Physics of the Earth and Planetary Interiors 361 (2025) 107320

Contents lists available at ScienceDirect

Physics of the Earth and Planetary Interiors

journal homepage: www.elsevier.com/locate/pepi

Radial structure of the Earth: (II) Model features and interpretations

Pritwiraj Moulik [a,*], Göran Ekström [b]

[a] Department of Geosciences, Princeton University, Princeton, NJ 08544, USA
[b] Lamont-Doherty Earth Observatory of Columbia University, Palisades, NY 10964, USA

ARTICLE INFO

Keywords:
Seismic velocities
Anisotropy
Attenuation
Density
Composition
Temperature

ABSTRACT

A new reference model is presented for the spherically-averaged profiles of elasticity, density and attenuation, which reflect the bulk composition, temperature profile and dominant processes of the Earth's heterogeneous interior. This study discusses the features of REM1D and geological interpretations while the underlying modeling concepts and reference datasets are described in a companion manuscript. All physical parameters in REM1D vary smoothly between the Mohorovičić and 410-km discontinuity, thereby excluding the 220-km discontinuity in earlier models. REM1D predicts arrival times of major body-wave phases in agreement (±0.8 s, normalized misfit $\psi_{pb} \leq 0.25$ s) with widely used but theoretically incomplete isotropic models optimized for earthquake location. Substantial radial anisotropy is present only in the shallowest mantle (~250 km) with peak values of shear-wave ($a_S = 3.90$ %, $\xi = 1.08$) and compressional-wave anisotropy ($a_P = 3.78$ %, $\phi = 0.93$) between ~125–150 km, consistent with textures that can form by the alignment of intrinsically anisotropic minerals in this deforming region. The upper mantle (24.4–410 km) is the most dissipative region with a finite bulk attenuation ($Q_\kappa \sim 386$) and strong shear attenuation ($Q_\mu \sim 60$–80) that peaks at a depth of ~150–175 km in the mechanically weak asthenosphere. An olivine-rich pyrolitic composition is broadly consistent with REM1D structure in the upper mantle and extended transition zone ($\lesssim 800$ km) with step changes across the 410-km and 650-km discontinuities. Features of the lower mantle can be reconciled with: (i) effects of thermally driven convection throughout the central lower mantle (771–2741 km) leading to an apparent subadiabaticity in the stratification parameter η_B, (ii) effects of spin transitions in iron-bearing minerals that manifest as distinct linear segments in modulus and Poisson's ratios (μ/κ, σ_P) on either side of a complex transition region (~1300–1700 km, 52–73 GPa), (iii) a thermal boundary layer with steeper superadiabatic gradients than near the surface, which ultimately exceed the critical gradients for both v_P and v_S (but not for density ρ) at a depth of 2741 km, and (iv) chemical stratification in the bottom ~500–750 km of the mantle that acts to suppress the thermal effects. Signatures of this thermo-chemical boundary layer are: (i) a gradual increase of density and steep positive gradients with depth ($d\rho/dz$) in the lower mantle, (ii) large values of the stratification parameter ($\eta_B > 1.03$) followed by an abrupt reduction to values below one near the core-mantle boundary (CMB), (iii) variations in bulk modulus with pressure $\kappa' = d\kappa/dp$ that are inconsistent with Equations of state (EoS) expectations of a uniform composition, (iv) very steep negative v_P and v_S gradients that form a low-velocity zone in the D″ region. The v_P and ρ variations in the outer core have steep gradients and the derivative properties are consistent with a neutrally stable region comprising a well-mixed iron alloy undergoing adiabatic compression ($\eta_B \simeq 1$, $N^2 \simeq 0$, negative κ'). REM1D is readily extendable due to its modular construction and represents the average physical properties, features essential for geological interpretations and the construction of a three-dimensional reference Earth model.

1. Introduction

Radial reference models describe Earth structure in terms of average elastic, anelastic and density variations, features indicative of the bulk composition and dominant processes within the Earth's interior. Classical one-dimensional (1D) models like the preliminary reference Earth model (PREM; Dziewoński and Anderson, 1981) serve as the critical baseline in a plethora of geophysical, geodetic, geochemical and

* Corresponding author.
E-mail addresses: moulik@caa.columbia.edu, moulik@princeton.edu (P. Moulik).

https://doi.org/10.1016/j.pepi.2025.107320
Received 4 March 2024; Received in revised form 2 December 2024; Accepted 1 February 2025
Available online 10 February 2025

petrological applications. Recent emphasis in global seismic imaging has been on quantifying the strength and extent of regional deviations away from the bulk Earth structure. Seismological heterogeneity affords constraints on intrinsic properties like temperature or composition and has implications for dynamic flow, rheology, grain size or crystal structure. Full heterogeneity in seismic properties can be imaged with three-dimensional (3D) tomographic models (e.g. Ritsema et al., 2011; Moulik and Ekström, 2014; French and Romanowicz, 2014; Bozdağ et al., 2016), which have reached a strong enough similarity to warrant the construction of a 3D reference Earth model (e.g. REM3D; Moulik et al., 2022). A key ingredient for REM3D construction is a new 1D reference model, which can represent the spherical average of Earth's heterogeneity and serve as an accurate baseline or starting model. Based on methodological advancements and expanded datasets, there is broad consensus on the need to update the preliminary information contained in PREM. Due to the recent focus on full 3D heterogeneity, it is often assumed that the ostensibly simpler average 1D structure is already known. However, several aspects of radial variations remain debated and geological interpretations motivate the construction of a new radial reference Earth model.

Bulk chemical composition of various principal regions in the Earth's interior informs our understanding of planetary-scale processes such as the accretion and evolution of the crust, mantle and core through differentiation and plate tectonics. Pyrolite is a candidate mineral assemblage dominated by olivine (~60 %) and orthopyroxene similar in composition to a fertile peridotite (Ringwood, 1966, 1975; Green and Ringwood, 1967; McDonough et al., 1995), which is used widely as the default mantle composition in dynamical simulations (e.g. Nakagawa and Tackley, 2005), rheological modeling (e.g. Hirth and Kohlstedt, 1996) and seismic interpretations (e.g. Weidner, 1985; Gaherty et al., 1999b; Matas et al., 2007). The pyrolitic model has been successful in explaining several observations in the shallowest mantle such as relationships between the chemistry of mid-ocean ridge basalts (MORB) upon partial melting, mantle temperature, ridge height and crustal thicknesses (e.g. Klein and Langmuir, 1987; McKenzie and Bickle, 1988; Workman and Hart, 2005). The different isotopic signatures of MORBs and ocean-island basalts (OIBs) provide compelling evidence for geochemically distinct yet accessible reservoirs in the deep mantle that may differ in bulk composition (e.g. Zindler and Hart, 1986; Kellogg et al., 1999; Hofmann, 2003). Revised estimates of average seismic properties are critical for calibrating the bulk composition in mineralogical models and dynamic simulations.

Radial variations in elastic properties and density with abrupt changes across seismically detected discontinuities provide important constraints on the current thermo-chemical state (e.g. Weidner and Wang, 2000; Faul and Jackson, 2005; Hirose et al., 2013) and dynamics of mass and heat transport in the Earth's deep interior (e.g. Christensen and Yuen, 1985; Jeanloz and Knittle, 1989; Tackley et al., 1993). A well-mixed, vigorously convecting domain with homogeneous composition undergoing self-compression along an arbitrary temperature adiabat may serve as a good starting approximation in large portions of the Earth's interior (e.g. Williamson and Adams, 1923; Jarvis and Mckenzie, 2006). Equations of state (EoS), which are used to calculate the elastic and thermodynamic properties of minerals at high pressure and temperature conditions (e.g. bulk modulus κ and its pressure derivative $\kappa' = d\kappa/dp$), are valid for an adiabatic region of uniform composition. EoS for various bulk compositions calibrated against radial reference models can be extrapolated to extreme conditions beyond that of the Earth's interior (e.g. $p \gg 364$ GPa), which are pertinent to the emerging studies of rocky and potentially habitable exoplanets called Super-Earths (e.g. Duffy et al., 2005; Seager, 2013; Boujibar et al., 2020; Kraus et al., 2022). Elastic and density structure from radial models such as PREM have been used with available EoS data to argue for a silicate mantle, an inner core composed of a crystalline phase of iron with some light elements, and a liquid outer core comprising additional lighter alloying elements (e.g. C, H, S, Si, or O; Birch, 1952, 1964; Jephcoat and Olson, 1987; Hirose et al., 2021).

However, the homogeneity assumption is violated when the chemical composition is variable while the adiabicity assumption is violated in regions internally heated by radioactive decay or when thermal boundary layers form to facilitate secular cooling (e.g. Jeanloz and Morris, 1987; Parmentier et al., 1994; Bunge et al., 2001; Monnereau and Yuen, 2002). Inhomogeneity can even arise in regions with a purportedly fixed bulk chemical composition due to the phase transitions of constituent minerals. For example, both *ab initio* calculations and laboratory experiments detect a phase transition from $MgSiO_3$-perovskite (Pv) to post-perovskite (pPv) (e.g. Murakami et al., 2004; Oganov and Ono, 2004; Tsuchiya et al., 2004) and a transition in the electronic spin state of iron in bridgmanite [$(Mg,Fe)SiO_3$-perovskite] and ferropericlase [(Mg,Fe)O] under lower-mantle conditions (e.g. Badro et al., 2003; Tsuchiya et al., 2006; Wentzcovitch et al., 2010; Badro, 2014). Since the pressure of a phase transition generally depends on temperature via the Clausius–Clapeyron equation, average depth of a discontinuity in seismological studies anchors the adiabatic geotherm (e.g. Stixrude and Lithgow-Bertelloni, 2011). A thermal boundary layer with superadiabatic gradients needs to exist in the lowermost mantle to facilitate the transfer of heat from the core (e.g. Stacey and Loper, 1983; Lay et al., 2008; Frost et al., 2022). Regional or even global departures from a homogeneous pyrolitic composition and adiabatic gradients have been proposed in the mantle transition zone and the lower mantle (e.g. Jeanloz and Richter, 1979; Mattern et al., 2005; Cobden et al., 2009). Thermo-chemical heterogeneity has been detected in the lowermost mantle based on full spectrum tomography (FST; Moulik and Ekström, 2016), which can manifest as signatures of chemical stratification in radial models if the heterogeneity is strong and pervasive. Departures from a state of adiabaticity and homogeneity can be probed seismologically using absolute density and velocity variations (e.g. Karato and Karki, 2001), or diagnostics like κ' (Bullen, 1949; Stevenson, 1980), modulus ratio (i.e. μ/κ, where μ is the shear modulus; Falzone and Stacey, 1980; Burakovsky et al., 2004; Kennett, 2021), and the stratification parameter (η_B; Bullen, 1963). Any anomalous signatures can afford insights into temperature gradients, heat flux, thermal history, phase or spin transitions, pervasive anisotropy, thermal boundary layers, chemical stratification and compositional heterogeneity.

Properties of the mantle transition zone (410–650 km depth) are of particular geological interest since they are strongly sensitive to bulk composition and influence the flow of material between the upper and lower mantle. While some body-wave studies have reported the continuity of slabs down to the lowermost mantle suggestive of whole-mantle convection (e.g. Grand et al., 1997; van der Hilst et al., 1997), recent studies have shown an accumulation of subducted material in the transition zone and horizontal flattening of the slabs using body waves (Fukao and Obayashi, 2013) and the full spectrum of seismological observations (~1–3200 s; Moulik and Ekström, 2014). Abrupt step changes in physical properties across the transition zone have been attributed to the phase transition of olivine [$(Mg,Fe)_2SiO_4$], the primary component of pyrolite, to its high-pressure polymorphs wadsleyite (410 km, $\alpha \rightarrow \beta$) and ringwoodite (550 km, $\beta \rightarrow \gamma$), followed by the dissociation (650 km, $\gamma \rightarrow$ pv + pc) of ringwoodite into bridgmanite and ferropericlase (e.g. Ringwood, 1975; Liu, 1979; Jackson, 1983). Based on discrepancies between seismological models and mineralogical predictions of pyrolite in the transition zone, other compositional models such as piclogite enriched in eclogitic components ($<$ 40 % olivine) have been invoked (e.g. Bass and Anderson, 1984). Most geodynamic models favor a phase transition in a homogeneous mantle at the depth of ~650 km while some geochemical studies favor a chemical discontinuity (e.g. Hofmann, 1997). For a pyrolitic composition, discrepancies between mineralogical and seismological estimates may not be large for the 650-km discontinuity (Yu et al., 2008; Wentzcovitch et al., 2010). Thermo-chemical interpretations in this region will benefit from new seismological estimates of absolute physical properties including the step changes across discontinuities.

Seismological studies differ in the treatment of intrinsic attenuation, or the lack thereof, during the construction of radial reference models. A few studies account for the effects of physical dispersion on body-wave arrival times without solving explicitly for the radial variations in intrinsic attenuation (e.g. Kennett et al., 1995; Kustowski et al., 2008). These approximations are often needed to reduce complexity of the inverse problem given the greater uncertainty in measurements of attenuation than of wave speeds (Dahlen, 1982). However, it is clear that the elastic and anelastic responses in the solid Earth manifest jointly through attenuation and dispersion of seismic waves and are best treated jointly in inversions (e.g. Randall, 1976; Liu et al., 1976; Hart et al., 1977; Dahlen and Tromp, 1998; Moulik and Ekström, 2025). Furthermore, joint analyses of elastic parameters and attenuation inform interpretations on intrinsic variables such as temperature T, pressure p, grain size d, chemical composition C, melt fraction and crystal structure (e.g. Faul and Jackson, 2005; McCarthy et al., 2011; Priestley and McKenzie, 2013; Olugboji et al., 2013; Abers et al., 2014) and their dynamic evolution (e.g. Tackley, 2012; Dannberg et al., 2017). PREM was the first radial model to constrain the elastic and anelastic structure simultaneously. Elastic properties from PREM are often assumed *a priori* while constructing models of seismic attenuation (e.g. Widmer et al., 1991; Durek and Ekström, 1996). Even though physical dispersion intricately links the elastic and attenuation properties, most studies since PREM have modeled them in isolation, leading to biased estimates of structure (Moulik and Ekström, 2025).

The mechanism of attenuation in seismic waves is attributed largely to shear friction $\left(\propto Q_\mu^{-1}\right)$ rather than to bulk dissipation ($\propto Q_\kappa^{-1}$) in the Earth (Heinz et al., 1982). Ratio of bulk to shear dissipation ($R_q = Q_\kappa^{-1}/Q_\mu^{-1} = Q_\mu/Q_\kappa$) is diagnostic of various solid-state mechanisms and the presence of fluids or partial melt (e.g. Anderson, 1980; Budiansky et al., 1983). Several generations of models agree broadly on features like a highly attenuating (low Q_μ) asthenosphere although details such as the location of peak attenuation remain debated (e.g Anderson and Hart, 1978; Sailor and Dziewonski, 1978; Dziewoński and Anderson, 1981; Widmer et al., 1991; Selby and Woodhouse, 2002). Although low values of shear attenuation in the transition zone could be indicative of water enrichment (e.g. ~0.1 wt%, Karato, 2011), most global studies report an increase in Q_μ from the upper mantle to the transition zone (e.g. Widmer et al., 1991; Durek and Ekström, 1996). While a finite bulk dissipation is needed to fit the observed decay of radial normal modes, strength and location of this feature is debated with estimates ranging from asthenosphere to the inner core (Dziewoński and Anderson, 1981; Durek and Ekström, 1995). Normal-mode studies report either a constant Q_μ in the lower mantle (Dziewoński and Anderson, 1981) or a slight decrease with depth (e.g. Widmer et al., 1991). A few studies of body-wave (e.g. ScS-S) spectra have reported an increase in Q_μ in the lowermost 1000 km of the mantle (e.g. Lawrence and Wysession, 2006; Durand et al., 2013). These apparent discrepancies between normal-mode and body-wave studies are sometimes used to invoke a frequency dependence ($Q^{-1}(f) \propto f^{-\alpha_Q}$) of attenuation (e.g. Hwang and Ritsema, 2011), which is typically observed in mineral assemblages under experimental conditions (e.g. α_Q = 0.2–0.4; Jackson and Faul, 2010) and is attributed to the mechanism of diffusionally accommodated grain boundary sliding (e.g. Raj, 1975). Joint modeling of elastic and anelastic structure can help identify the dominant dissipation mechanisms that are active in various regions at seismic frequencies (~0.3 mHz – 1 Hz).

Accurate estimates of average radial anisotropy in the mantle are critical for geological interpretations. To first order, anisotropy in the uppermost mantle could be caused by flow alignment of olivine, the major component of pyrolite, under dislocation creep (e.g. Nicolas and Christensen, 1987). Convection in the upper mantle can therefore be constrained with seismology by modeling the textures formed by lattice-preferred orientation (LPO) of these intrinsically anisotropic grains (e.g. Mainprice, 2007). This mechanism is likely to be most active in material undergoing shear strain, such as from the relative motion between lithospheric plates and the underlying mantle in oceanic basins (e.g. Montagner, 1998). Since LPO-style textures are formed by the dominance of dislocation rather than diffusion creep, amplitudes of seismic anisotropy also help constrain mantle rheology through flow laws (e.g. Karato, 1992; Karato, 1998; Gaherty and Jordan, 1995). In contrast to flow-based anisotropy arising from the strain fields of recent mantle convection (10 to 100 Ma timescale), anisotropy can also be frozen due to past strain fields and tectonic episodes (100 Ma to 1 Ga timescale). Layers and cracks with different isotropic velocities or aligned pockets of melt can cause the shape-preferred-orientation (SPO) style of anisotropy, which is possible in the crust and mantle lithosphere of localized regions (e.g. Schlue and Knopoff, 1976; Holtzman et al., 2003; Kawakatsu et al., 2009). Radial anisotropy can therefore aid global interpretations of composition, rheology, tectonic history, and deviatoric stresses or strain fields in geodynamic modeling.

Seismological models are yet to reach a consensus on the distribution and strength of average anisotropy in the Earth. Shear-wave anisotropy in PREM is strongest at the Mohorovičić discontinuity (hereafter Moho) with ~5 % $v_{SH} > v_{SV}$ and decreases monotonically to zero at the 220-km discontinuity. Bulk anisotropy in the mantle lithosphere (24.4–80 km) is strongly discrepant across various studies with values ranging from almost zero in STW105 (Kustowski et al., 2008) to 3–4.5 % in PREM. Some regional studies of oceanic basins argue for a weakly anisotropic lithosphere underlain by a highly anisotropic asthenosphere (e.g Maggi et al., 2006; Beghein et al., 2014) while local studies have reported strong anisotropy in the mantle lithosphere (e.g. Lin et al., 2016). Recent tomographic studies have reported strong radial anisotropy in the oceanic upper mantle although the strength of anisotropy peaks at asthenospheric depths (~120–150 km) instead of at the Moho in PREM (e.g. Kustowski et al., 2008; Moulik and Ekström, 2014; French and Romanowicz, 2014; Chang et al., 2015). In deeper regions, there is no agreement on pervasive anisotropy although some studies have proposed shear-wave anisotropy ($v_{SV} > v_{SH}$) between 300 and 400 km (Montagner and Anderson, 1989b; Montagner and Kennett, 1996) and compressional-wave anisotropy ($v_{PV} > v_{PH}$) in the inner core (Lythgoe and Deuss, 2015). The disagreement between models in the transition zone is not only on the amplitude but also on the sign of shear-wave anisotropy. Montagner and Kennett (1996) reported $v_{SH} > v_{SV}$ in the transition zone with body-wave and normal-mode data while other studies have reported either $v_{SV} > v_{SH}$ (e.g. Visser et al., 2008) or negligible anisotropy (e.g. Beghein et al., 2006). A few three-dimensional studies have also reported a pervasive feature with $v_{SH} > v_{SV}$ in the lowermost mantle (e.g. Montagner and Kennett, 1996; Panning and Romanowicz, 2004). The strength and extent of radial anisotropy remains debated since it is a subtle signal that needs to be constrained using multiple datasets to avoid inter-parameter tradeoffs (e.g. Moulik and Ekström, 2014), while accounting for the non-linear effects of the crust on wave propagation (Moulik and Ekström, 2025).

Our approach on geological interpretations is predicated on the detection of structural features that improve the fits to reference datasets and are not dictated by prior information. While we utilize petrological and mineral physical constraints in our starting model, parameterization and regularization, all physical parameters are allowed to evolve in our iterative inversions based on data fits (Moulik and Ekström, 2025). Other studies often prescribe an EoS formulation, bulk chemical composition, kinetics of phase transformations or scaling relationships between physical parameters (e.g. Cammarano et al., 2005; Khan et al., 2008; Durand et al., 2012; Afonso et al., 2013; Irving et al., 2018). Alternatively, Moulik and Ekström (2025) demonstrated that adjusting the polynomial parameterization and regularization of solely seismological properties is sufficient to match expectations from mineral physics (e.g. on κ' and η_B) without deteriorating the fits to reference datasets. No interpretative assumptions on the EoS formulation (e.g. Birch, 1947; Vinet et al., 1987; Stacey, 1995) or estimates of molar mass,

Table 1
Principal regions in the Earth. The reference model REM1D is expressed as a linear combination of various basis functions: 7 evenly-spaced cubic B-splines (s_1-s_7), polynomial terms (x^2, x^3, x^4), and values at the top (**t**) and bottom (**b**) of a region. The splines are numbered from the bottom to the top of the upper mantle. Expressions for all basis functions (B_t,B_b,$B_{x^{2-4}}$,$B_{s_{1-7}}$) are provided in Appendix A of Paper I in terms of the normalized radius (i.e. $r = 1$ at $R = 6371$ km). When a physical parameter is uniform throughout a region, the value is specified (e.g. v_S=0 in the outer core) in lieu of an expression in terms of basis functions (e.g. v_S=**0b** + 0 **t**). REM1D is isotropic (v_P=v_{PH}=v_{PV}, v_S=v_{SH}=v_{SV}, η=1, cf. eq. 6) everywhere except the upper mantle. A value of $Q_\kappa = 88{,}888$ in our calculations represents ∞ within numerical precision. Values in the upper crust are extended to the surface and ocean is removed when calculating body-wave travel times (e.g. Figs. 8 and 9). The elastic parameters listed below are valid at a reference period of 1 s; values at other periods can be calculated using eq. 8 (e.g. Fig. 11). Supplementary Table S7 lists the physical properties evaluated from the coefficients below in 750 concentric layers/shells inside the Earth.

Region Abbreviation	Depth (km)	Radius (km)	Density (g cm^{-3})	v_P (km s^{-1})	v_S (km s^{-1})	$1/Q_\mu$	$1/Q_\kappa$	η
inner core [ICO]	5156–6371	0–1215	13.09162 **b**	11.24981 **b**	3.65706 **b**	1/89.54	1/88888	1
			12.76742 **t**	11.01525 **t**	3.49062 **t**			
			−8.95642 x^2	−6.44945 x^2	−4.57628 x^2			
			0.22073 x^3					
outer core [OCO]	2891–5156	1215–3480	12.16715 **b**	10.35230 **b**	0	0	1/88888	1
			9.89574 **t**	8.02182 **t**				
			−10.16263 x^2	−2.25876 x^2				
			7.20974 x^3	−8.21972 x^3				
			−9.14712 x^4					
D″ [DPP]	2741–2891	3480–3630	5.58518 **b**	13.63723 **b**	7.18664 **b**	1/348.83	1/28596	1
			5.50958 **t**	13.66946 **t**	7.25359 **t**			
			5.15747 x^2	6.85977 x^2	8.95909 x^2			
			−2.90209 x^3	−4.10097 x^3	−5.35213 x^3			
central lower mantle [CLM]	771 2741	3630–5600	5.50958 **b**	13.66946 **b**	7.25359 **b**	1/348.83	1/28596	1
			4.42566 **t**	11.07017 **t**	6.21181 **t**			
			5.15747 x^2	50.54766 x^2	35.88441 x^2			
			−2.90209 x^3	−26.03250 x^3	−18.11583 x^3			
upper lower mantle [ULM]	650–771	5600–5721	4.42566 **b**	11.07017 **b**	6.21181 **b**	1/348.83	1/28596	1
			4.27497 **t**	10.64552 **t**	5.93161 **t**			
			−0.94075 x^2	−15.46104 x^2	−9.43004 x^2			
			0.38599 x^3	5.73330 x^3	3.53809 x^3			
transition zone [TZO]	410–650	5721–5961	4.05516 **b**	10.38457 **b**	5.57002 **b**	5.18498e-3	1/28596	1
			3.73420 **t**	9.15227 **t**	4.97081 **t**			
				v_{PH} (km s^{-1})	v_{PV} (km s^{-1})	v_{SH} (km s^{-1})	v_{SV} (km s^{-1})	
upper mantle [UUM]	24.4–410	5961–6346.6	3.55535 **b**	8.92938 **b**	8.92938 **b**	4.80443 **b**	4.80443 **b**	5.18498e-3 **b**	1/385.62	1 **b**
			3.29724 **t**	8.10557 **t**	7.83981 **t**	4.57103 **t**	4.52545 **t**	4.62083e-3 **t**		0.92243 **t**
			0.00786 $\mathbf{s}_1$	−0.00626 $\mathbf{s}_1$	0.02814 $\mathbf{s}_1$	−0.02314 $\mathbf{s}_1$	−0.01690 $\mathbf{s}_1$	0.12036e-3 $\mathbf{s}_1$		0.00984 $\mathbf{s}_1$
			0.01053 $\mathbf{s}_2$	−0.03253 $\mathbf{s}_2$	0.02907 $\mathbf{s}_2$	−0.05317 $\mathbf{s}_2$	−0.04367 $\mathbf{s}_2$	1.14282e-3 $\mathbf{s}_2$		0.01905 $\mathbf{s}_2$
			0.01364 $\mathbf{s}_3$	−0.10341 $\mathbf{s}_3$	0.00703 $\mathbf{s}_3$	−0.09579 $\mathbf{s}_3$	−0.07383 $\mathbf{s}_3$	2.15677e-3 $\mathbf{s}_3$		0.01664 $\mathbf{s}_3$
			0.00270 $\mathbf{s}_4$	−0.18940 $\mathbf{s}_4$	−0.11050 $\mathbf{s}_4$	−0.13637 $\mathbf{s}_4$	−0.13321 $\mathbf{s}_4$	7.04272e-3 $\mathbf{s}_4$		0.01043 $\mathbf{s}_4$
			−0.00708 $\mathbf{s}_5$	−0.16800 $\mathbf{s}_5$	−0.31084 $\mathbf{s}_5$	−0.07560 $\mathbf{s}_5$	−0.24256 $\mathbf{s}_5$	13.54302e-3 $\mathbf{s}_5$		−0.02032 $\mathbf{s}_5$
			−0.00658 $\mathbf{s}_6$	−0.21327 $\mathbf{s}_6$	−0.32739 $\mathbf{s}_6$	−0.06196 $\mathbf{s}_6$	−0.19270 $\mathbf{s}_6$	9.58492e-3 $\mathbf{s}_6$		−0.02262 $\mathbf{s}_6$

(*continued on next page*)

Table 1 (*continued*)

Region Abbreviation	Depth (km)	Radius (km)	Density (g cm^{-3})	v_P (km s^{-1})		v_S (km s^{-1})		$1/Q_\mu$	$1/Q_\kappa$	η
			$-0.00254\ \mathbf{s}_7$	-0.10599 $\mathbf{s}_7$	-0.13233 $\mathbf{s}_7$	-0.02083 $\mathbf{s}_7$	-0.06047 $\mathbf{s}_7$	0.92144e-3 $\mathbf{s}_7$		-0.01125 $\mathbf{s}_7$
lower crust [LCR]	15–24.4	6346.6–6356	2.900	6.800		3.900		1/300	1/88888	1
upper crust [UCR]	3–15	6356–6368	2.600	5.800		3.200		1/300	1/88888	1
ocean [OCE]	0–3	6368–6371	1.020	1.450		0		0	1/88888	1

pressure and gravity in the outer core (e.g. Irving et al., 2018) need to be invoked for this purpose. Modeling in terms of seismological properties (e.g. v_S, Q_μ) is theoretically well established, invokes fewer approximations, and often affords better data fits with fewer independent parameters than directly modeling the underlying thermodynamical state (e.g. T, p, d, C). While characterizing relationships between the two sets of properties is a frontier area of research, mixing them during the construction of seismological models can lead to biased and circular interpretations. Outstanding questions on core inhomogeneity or departures from mantle pyrolitic composition can be robustly evaluated only when these complexities are permitted by the modeling scheme but are nevertheless disfavored by observations.

Here, we identify robust structural features and discuss interpretations while constructing a new radial reference Earth model REM1D. Previous seismological studies have restricted modeling to isotropic velocities (e.g. AK135 and AK135F; Kennett et al., 1995; Montagner and Kennett, 1996), employed only body-wave travel times (e.g. SP6; Morelli and Dziewonski, 1993), and ignored the effects of lateral heterogeneity. While there is no prescribed way to construct a radial reference Earth model, we build upon recent improvements in our understanding of 3D crustal structure (e.g. Bassin et al., 2000; Laske et al., 2013) and new methods that utilize diverse seismological observations using full spectrum tomography (FST; Moulik and Ekström, 2014, 2016). In a related study (Moulik and Ekström, 2025, hereafter referred to as Paper I), the FST technique for constructing 3D Earth models was extended to radial (1D) structure. We introduced concepts that account for geographic bias in observations, theoretical complexities (e.g. anisotropy and attenuation), and non-linear crustal effects. Paper I also discussed the new reference bulk Earth dataset comprising astronomic-geodetic constants, normal-mode observations, body-wave constraints and surface-wave dispersion curves, which were either poorly constrained or unavailable during the construction of PREM. Modeling concepts and data fits are summarized in Section 2 while structural complexities are evaluated in Section 3. We conclude, in

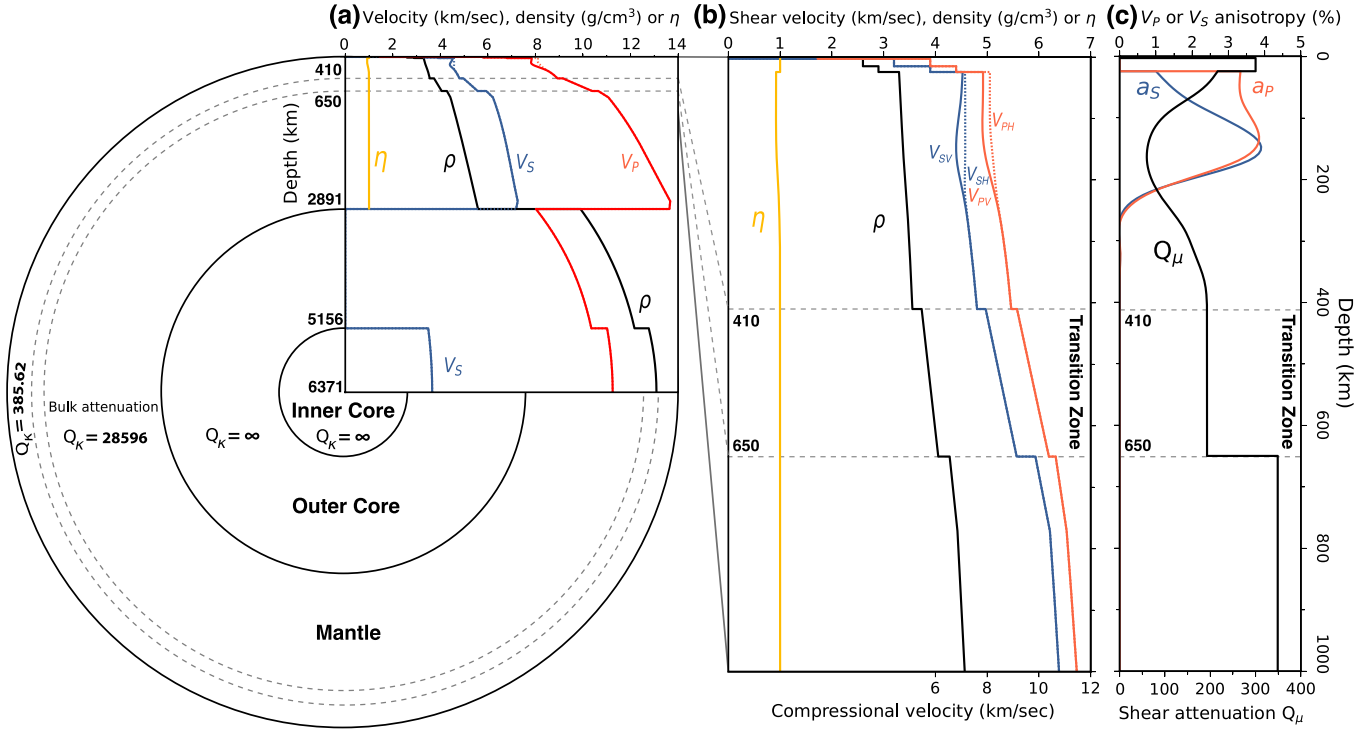

Fig. 1. The new radial reference Earth Model REM1D. Values of elastic parameters and density are provided for (a) the whole Earth and (b) the top 1000 km of the crust and mantle. (c) Shear attenuation (Q_μ) and anisotropy (i.e. a_S, a_P from eq. 3) in the shallowest regions. Dotted curves in (a–b) are the horizontal components of velocity (v_{SH}, v_{PH}) while solid curves are the vertical, or radial, components of velocity (v_{SV}, v_{PV}). REM1D is radially anisotropic in the upper mantle with η less than 1 and anisotropy (a_S and a_P) in the range of 1–4 %. Finite bulk attenuation is found in the mantle with two parameters above ($Q_\kappa = 385.62$) and below the 410-km discontinuity ($Q_\kappa = 28{,}596$). Shear attenuation peaks at a depth of ~150–175 km ($Q_\mu = 60$–80) but is also found in the lower mantle (650–2891 km, $Q_\mu = 348.83$) and the inner core ($Q_\mu = 89.54$). Peak anisotropy (a_S and a_P) is found 17 ± 5 km shallower in depth than the mechanically weak (low v_S and Q_μ) asthenosphere. REM1D describes bulk Earth structure in terms of a discrete set of basis functions (Table 1); this modular construction makes it readily extendable to various geochemical, petrological and seismological applications.

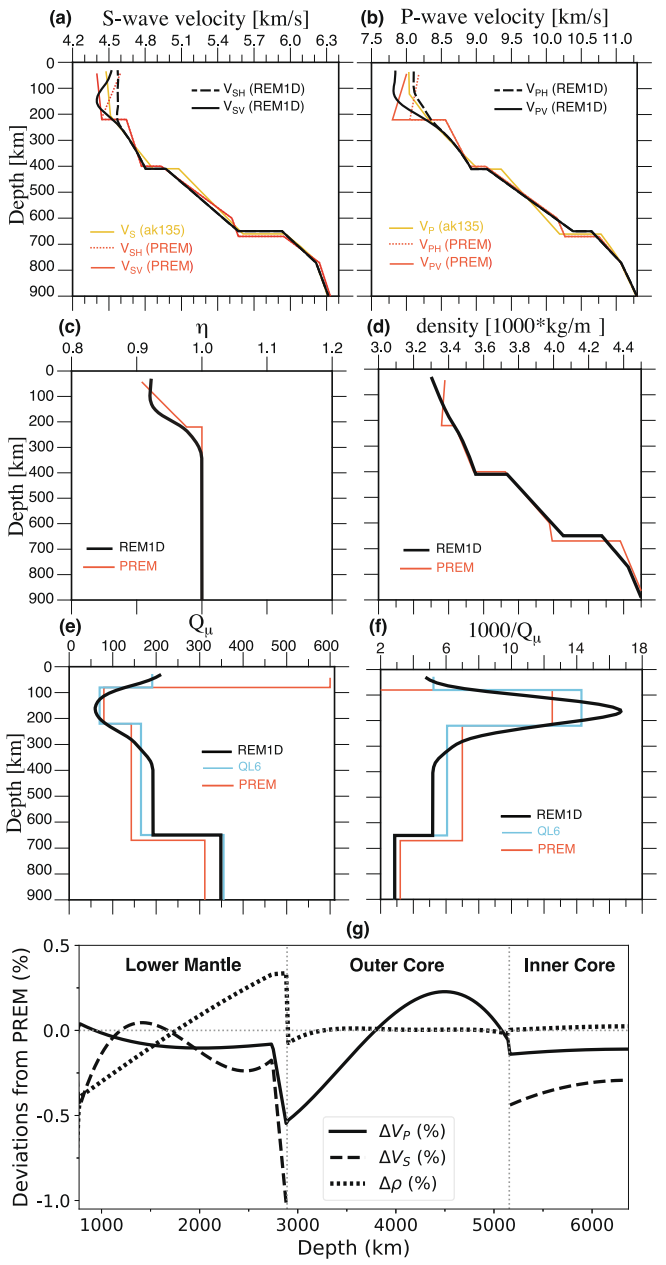

Fig. 2. Comparisons between REM1D and earlier models for (a–f) the upper mantle and transition zone, and (g) underlying regions. Elastic parameters and density from the anisotropic 1-D reference model PREM (Dziewoński and Anderson, 1981) and isotropic velocity model AK135 (Kennett et al., 1995) are plotted for comparison. Also shown are the variations in shear attenuation (Q_μ) from the radial model QL6 (Durek and Ekström, 1996). Percent deviations from PREM are plotted for the lower mantle and core, regions where absolute differences are relatively small in magnitude. More detailed comparisons between published models on variations in the outer core are provided in Fig. 7.

Sections 4 and 5, with geological interpretations and an overall outlook on radial structure.

2. Concept of the model

The construction of a new radial reference Earth model (REM1D) involves several modeling choices that dictate its parametric complexity (Table 1, Figs. 1 and 2). Outstanding questions persist regarding the choice of physical parameters that can be constrained using current datasets and relatedly, their geometric parameterization with depth. In the sections below, we justify our choices based on various considerations.

2.1. Physical parameterization

Physical parameters that describe the Earth's interior are chosen based on several theoretical and observational considerations. A radial reference model can be expressed as the spherically symmetric, non-rotating model

$$\oplus = \left(v_{PH}, v_{PV}, v_{SH}, v_{SV}, \eta, \rho, Q_\mu^{-1}, Q_\kappa^{-1}\right), \tag{1}$$

where the 8 physical parameters (m_k) include the 5 properties v_{PH}, v_{PV}, v_{SH}, v_{SV}, and η that define a transversely isotropic medium (e.g. Dziewoński and Anderson, 1981; Takeuchi and Saito, 1972; Dahlen and Tromp, 1998); ρ is density while Q_μ^{-1} and Q_κ^{-1} are attenuation parameters in shear and compression (or bulk), respectively. Here, we deal with the spherical equivalent of transverse isotropy where the symmetry axis is vertical (radial) for every parcel of material inside the solid Earth; this is also known as 'radial anisotropy' or 'polarization anisotropy' in the literature. The discrepancy in propagation velocities of Love and Rayleigh waves suggests that the upper mantle is anisotropic. This discrepancy is most prominent for waves that traverse the oceanic basins, which cover a majority of the Earth's surface. In contrast to classical studies, we invoke both radial anisotropy and the non-linear effects of crustal structure to explain the Love-Rayleigh wave discrepancy (Paper I). The influence of crustal heterogeneity on the average anisotropic structure is discussed further in Section 3.3.

For a radially anisotropic medium, wave propagation is determined by the 5 elastic parameters **A**, **C**, **L**, **N** and **F** (Love, 1927) that are related to parameters in eq. 1 following

$$v_{PH} = \sqrt{\mathbf{A}/\rho} \qquad v_{SH} = \sqrt{\mathbf{N}/\rho}$$
$$v_{PV} = \sqrt{\mathbf{C}/\rho} \qquad v_{SV} = \sqrt{\mathbf{L}/\rho}$$
$$\eta = \mathbf{F}\Big/(\mathbf{A} - 2\mathbf{L}) \tag{2}$$

The constant **N** (or v_{SH}) dictates the propagation of fundamental mode Love waves while all five constants, especially **L** (or v_{SV}), are important for Rayleigh waves (e.g. Takeuchi and Saito, 1972). The first two terms dictate the velocity of compressional (P) waves propagating perpendicular (i.e. horizontal, v_{PH}) and parallel (i.e. vertical, v_{PV}) to our axis of symmetry (vertical or radial). In contrast, shear-wave velocity depends both on polarization and direction of propagation. The terms **N** and **L** describe the velocity of horizontally (v_{SH}) and vertically polarized shear waves (v_{SV}), respectively, while propagating in the horizontal direction perpendicular to our axis of symmetry (vertical or radial). SH waves (e.g. S or ScS) recorded on the transverse component can propagate sub-horizontally for a substantial portion of the ray path near the bottoming depth; in the presence of mantle anisotropy (typically $v_{SH} > v_{SV}$), this leads to slightly faster arrivals (< 2 s) than the related SV waves recorded on the radial component. In the radial propagation direction that is parallel to our symmetry axis, there is no splitting in arrival time as both polarizations of shear waves are controlled by the same elastic constant **L** (or v_{SV}). Therefore, both horizontally and vertically propagating (reflected or converted) SV waves (i.e. SKS, SKKS, ScP, SP and SKIKP) recorded on the radial component travel with the same velocity. The fifth non-dimensional parameter η dictates the velocities at intermediate incident angles, and strongly influences fundamental mode Rayleigh wave dispersion (e.g. Dziewoński and Anderson, 1981). An alternative fifth non-dimensional parameter $\eta_\kappa = (\mathbf{F} + \mathbf{L})/\sqrt{(\mathbf{A} - \mathbf{L})(\mathbf{C} - \mathbf{L})}$ has recently been proposed to characterize incident angle dependence of body waves (Kawakatsu, 2016). Deviations of η_κ from one represent departures from the elliptic condition that would require phase velocity surfaces of body waves to be either circular (SV) or elliptic (P and SH; Thomsen, 1986). The magnitude of radial anisotropy is often quantified in the geosciences using four terms

$$a_S = \frac{2\cdot(v_{SH} - v_{SV})}{v_{SH} + v_{SV}}$$
$$a_P = \frac{2\cdot(v_{PH} - v_{PV})}{v_{PH} + v_{PV}} \quad (3)$$
$$\xi = \left[\frac{v_{SH}}{v_{SV}}\right]^2 \qquad \phi = \left[\frac{v_{PV}}{v_{PH}}\right]^2,$$

where a_S and ξ represent shear-wave anisotropy while a_P and ϕ represent compressional-wave anisotropy.

In order to derive 'equivalent' isotropic properties in the radially anisotropic parts of the mantle, we perform Voigt averaging following

$$v_P = \sqrt{(\lambda + 2\mu)/\rho} = \sqrt{(\kappa + 4/3\mu)/\rho}$$
$$v_S = \sqrt{\mu/\rho} \quad (4)$$
$$v_\Phi = \sqrt{\kappa/\rho},$$

where v_P, v_S and v_Φ are the isotropic compressional-wave, shear-wave and bulk-sound velocity, respectively. The Lamé parameters (λ and shear modulus μ) and bulk modulus represent the upper bounds of the effective moduli and are related to the anisotropic parameters as

$$\kappa = \frac{1}{9}[4\mathbf{A} + \mathbf{C} + 4\mathbf{F} - 4\mathbf{N}]$$
$$\mu = \frac{1}{15}[\mathbf{A} + \mathbf{C} - 2\mathbf{F} + 5\mathbf{N} + 6\mathbf{L}] \quad (5)$$
$$\lambda = \kappa - \frac{2}{3}\mu.$$

Note that a purely isotropic reference model described by the following conditions

$$\mathbf{A} = \mathbf{C} = \kappa + \frac{4}{3}\mu \qquad \mathbf{N} = \mathbf{L} = \mu \qquad \mathbf{F} = \lambda = \kappa - \frac{2}{3}\mu \qquad \eta = 1$$
$$v_P = v_{PH} = v_{PV} \qquad v_S = v_{SH} = v_{SV} \qquad a_P = a_S = 0 \qquad \xi = \phi = 1 \quad (6)$$

does not satisfactorily fit our reference surface-wave datasets from Paper 1; as such, the derived 'equivalent' isotropic parameters in the upper mantle are valid only for certain non-seismological applications where anisotropy may be ignored e.g. calibration of the average properties in a dynamic simulation (e.g. Dannberg et al., 2017).

In the general case of a weakly anisotropic medium, wave speeds are controlled by eight other linear functions of elasticity tensor components: the six 2ζ terms G_c, G_s, B_c, B_s, H_c and H_s, and the two 4ζ terms E_c and E_s, where ζ denotes the local wave ray azimuth with respect to the local meridian (Montagner and Nataf, 1986). There is some observational evidence of two-fold (2ζ) or four-fold (4ζ) azimuthal variations in surface-wave phase velocities (Forsyth, 1975), which can contribute substantially to the propagation phase and vary in pattern and strength across regional (e.g. Montagner and Jobert, 1988; Nishimura and Forsyth, 1989; Maggi et al., 2006; Marone and Romanowicz, 2007) and global scales (e.g. Montagner, 2002; Ekström, 2011; Ma et al., 2014; Schaeffer et al., 2016). Two-fold (2ζ) azimuthal anisotropy for surface waves means that the full, azimuthally varying phase velocity $c^\star(\zeta)$ can be expressed as

$$c^\star(\zeta) = c_0(\zeta)[1 + A_0 + A_2\,cos2\zeta + B_2\,sin2\zeta + A_4\,cos4\zeta + B_4\,sin4\zeta], \quad (7)$$

where $A_0 = \delta c/c_0$ denotes a static azimuthally averaged perturbations to the reference isotropic propagation velocity c^0 derived from the radial reference model. The terms A_2, B_2, A_4 and B_4 are coefficients describing azimuthal variations in phase velocity and are depth integrals involving the radial eigenfunctions of the reference model (Smith and Dahlen, 1973). Expressions for a medium with azimuthal anisotropy can also be derived for body wave phases with an additional dependence on the local angle of incidence (e.g. Backus, 1965; Jech and Pšenčík, 1989; Farra, 2005; Chen and Tromp, 2007), and for splitting of normal modes accounting for the resonance (or coupling) between standing vibrations at discrete frequencies (e.g. Woodhouse, 1980; Mochizuki, 1986). Since lateral variations in the two-fold (2ζ) anisotropy of Rayleigh waves are geographically consistent across measurement techniques and afford statistically significant improvements in data fits (Moulik et al., 2022), we use a reference dataset of fundamental-mode Rayleigh waves that is already corrected for azimuthal variations (Paper I).

The elastic and anelastic responses are two intricately linked aspects of Earth's rheology. Anelasticity influences the propagation velocities of seismic waves through dispersion and is a major reason for attenuation of amplitudes following the excitation by an earthquake. We adopt the intrinsic quality factor (i.e. $Q(f)$ at frequency f) as a measure of the volumetric rate of energy dissipation that appears as heat due to anelasticity (e.g. O'Connell and Budiansky, 1978). A single mechanism of energy dissipation can be denoted with a characteristic relaxation function of a standard linear solid that describes the response (i.e. departure from elasticity) of the solid at various frequencies (e.g. Zener, 1948; Nowick and Berry, 1972). Recently, forced oscillation tests have investigated anelasticity as a function of timescale, temperature T, pressure p, grain size d, melt fraction, and chemical composition C (e.g. Gribb and Cooper, 1998; Jackson et al., 2002; McCarthy et al., 2011; Faul and Jackson, 2015). A consistent feature of the experiments on melt-free (and mostly dry) polycrystalline aggregates is an absorption band (high-temperature background) with a mild frequency dependence ($\alpha_Q = 0.2$–0.4), which may be consistent with the mechanism of diffusionally accommodated grain boundary sliding (e.g. Raj, 1975). Since experiments are conducted at lower p-T-d conditions than in the real Earth, extrapolating properties of the absorption band at seismic frequencies is an outstanding problem in the geosciences.

From a seismological standpoint, waves at longer periods generally probe deeper regions of the Earth and it is therefore difficult to disentangle the effect of frequency dependence of attenuation (α_Q) from those stemming from its depth variation. We prescribe that quality factors are frequency independent ($\alpha_Q = 0$) for both shear friction ($Q_\mu(f) \approx Q_\mu$) and bulk dissipation ($Q_\kappa(f) \approx Q_\kappa$) within the seismic band of interest (~1–3200 s) and discuss implications later in this study (Section 4.2). Some energy dissipation mechanisms can cause anisotropy of attenuation at exploration scales (~0.1–10 km), such as due to fluid flow through the porous rock matrix or the interbedding of thin and variable attenuative layers (e.g. Mukerji and Mavko, 1994; Carcione, 2000; Chapman, 2003). We ignore this complexity since there is no clear evidence that such mechanisms are pervasive or operate over wavelengths that may be detected by long-period waves (> 20 s) and manifest as global features. In a medium with radial anisotropy in elastic properties and isotropy in anelastic properties, physical dispersion causes a traveling wave (or a corresponding normal mode) to 'see' the elastic parameters at the dominant period T (or eigenfrequency $\omega = 2\pi/T = 2\pi f$) of vibration $m_k(T)$ following

$$\frac{m_k(T)}{m_k(1)} = \begin{cases} 1 - \dfrac{2lnT}{\pi}\left[\dfrac{(1-E)}{Q_\kappa} + \dfrac{E}{Q_\mu}\right], & \text{for } m_k \in [\mathbf{A}, \mathbf{C}] \\ 1 - \dfrac{2lnT}{\pi Q_\mu}, & \text{for } m_k \in [\mathbf{N}, \mathbf{L}] \\ 1 - \dfrac{2lnT}{\pi}\left[\dfrac{\dfrac{(1-E)}{Q_\kappa} - \dfrac{E}{2Q_\mu}}{1 - \dfrac{3}{2}E}\right], & \text{for } m_k \in [\boldsymbol{F}] \\ 1 - \dfrac{lnT}{\pi}\left[\dfrac{(1-E)}{Q_\kappa} + \dfrac{E}{Q_\mu}\right], & \text{for } m_k \in [v_P] \\ 1 - \dfrac{lnT}{\pi Q_\mu}, & \text{for } m_k \in [v_S] \end{cases} \quad (8)$$

and

$$E = \frac{4}{3}\left[\frac{v_S}{v_P}\right]^2 = \frac{4}{3}\left[\frac{\mathbf{A}+\mathbf{C}-2\mathbf{F}+5\mathbf{N}+6\mathbf{L}}{8\mathbf{A}+3\mathbf{C}+4\mathbf{F}+8\mathbf{L}}\right], \tag{9}$$

derived by applying the chain rule to the 'equivalent' isotropic expressions in eq. 6 (e.g. $dln\mathbf{N} = dln\mathbf{L} = dln\mu = -\frac{2lnT}{\pi Q_\mu}$ and $dln\mathbf{F} = \left[d\kappa - \frac{2}{3}\cdot d\mu\right] / \left[\kappa - \frac{2}{3}\mu\right] = [(1-E)\cdot dln\kappa - E/2\cdot dln\mu\,] / \left[1 - \frac{3}{2}E\right]$). Here, we employ the approximation that logarithmic dispersion of the elastic moduli ($m_k \in [\mu, \kappa, \mathbf{A}, \mathbf{C}, \mathbf{N}, \mathbf{L}, \mathbf{F}]$) can be expressed in terms of the corresponding frequency-independent quality factors Q_k following $\frac{dlnm_k(\omega)}{dln\omega} \approx \frac{2}{\pi Q_k}$ (e.g. O'Connell and Budiansky, 1978; Dahlen and Tromp, 1998). Note that while simplified expressions are provided above for the dispersed velocities in isotropic regions (i.e. following $dln\mathbf{N} = dln\mathbf{L} = 2\cdot dlnv_S$ and $dln\mathbf{A} = dln\mathbf{C} = 2\cdot dlnv_P$), anisotropic velocities in the upper mantle should be calculated explicitly from the dispersed elastic parameters following eq. 2. The physical properties represented by our radial reference Earth model (i.e. $\oplus$, REM1D, Table 1, Fig. 1) are valid at the reference period of 1 s, denoted by $m_k(1)$, and are used to obtain E above.

Other parameters useful for geological interpretations such as pressure (p), gravity (g), Brunt-Väisälä frequency (N^2), Poisson's ratio (σ_P) and the Bullen's stratification parameter (η_B) can be derived from our radial reference model (e.g. Bullen, 1963; Dahlen and Tromp, 1998). The gradient of bulk modulus with pressure ($\kappa' = d\kappa/dp$) and its curvature ($\kappa'' = d^2\kappa/dp^2$) are important EoS parameters for relating pressure, temperature and density of material in thermal equilibrium. In a well-mixed isochemical region, the derivative EoS parameter κ'' should remain negative over an entire pressure range, decreasing in magnitude to zero at high pressures ($p \to \infty$; e.g. Stevenson, 1980; Stacey, 1995). An EoS formulation to characterize physical properties within a principal region is valid unless the assumptions of homogeneity and adiabaticity are violated (Sections 4.6 and 4.9). Bullen's η_B parameter measures deviations from a standard adiabatic and homogeneous region that is in hydrostatic equilibrium following the Adams-Williamson equation for density gradients ($d\rho/dr = -\rho^2 g/\kappa$). In terms of the pressure derivative of bulk modulus $d\kappa/dp \equiv (d\kappa/dr)/(dp/dr)$ in the radial reference model,

$$\eta_B = \frac{d\kappa}{dp} + \frac{1}{g}\frac{d}{dr}\left(\frac{\kappa}{\rho}\right). \tag{10}$$

In order to interpret the physical significance of the η_B values, it is useful to consider separate contributions of departures from adiabaticity and large-scale homogeneity following

$$\eta_B = 1 - \frac{\alpha\kappa\tau}{\rho g} - \frac{\kappa}{\rho^2 g}\sum_{i=1}^{n}\frac{\partial\rho}{\partial C_i}\frac{dC_i}{dr}, \tag{11}$$

where $\alpha = 1/V(\partial V/\partial T)_p$ is coefficient of thermal expansion for a volume V at pressure p, τ (in K/m) is deviation from the adiabatic temperature gradient in a chemical mixture of n components and C_i is a measure of the amount of each component (e.g. Birch, 1952; Bullen, 1967; Masters, 1979). Based on these considerations, it is clear why we refer to η_B as the stratification parameter since it is a measure of how much a region is either thermally or chemically stratified.

Bullen's stratification parameter can be used to detect regions with subadiabatic ($\tau < 0$) temperature gradients ($\eta_B > 1$) or regions containing thermal boundary layers with superadiabatic ($\tau > 0$) temperature gradients ($\eta_B < 1$). Note that chemical inhomogeneity ($n > 1$ in eq. 11) can theoretically act to either amplify or suppress the contribution from temperature gradients depending on the physical properties and ratios of the individual components. Irrespective of their origin (e.g. polymorphism, primordial material, core interaction, tectonic deposition), most high-density components in the Earth tend to either thermodynamically equilibrate or gravitationally stabilize at greater depths (or lesser radii i.e. $dC_i/dr < 0$). Therefore, inhomogeneity due to phase transitions or chemically distinct components will tend to manifest as η_B values substantially greater than one in regions where these processes are pervasive. The parameter Brunt-Väisälä frequency N^2 is of interest in the fluid regions and is defined as

$$N^2 = -\frac{g}{\rho}\frac{d\rho}{dr} - \frac{\rho g^2}{\kappa}. \tag{12}$$

For the Earth, this parameter is most relevant for the outer core, where positive values ($N^2 > 0$) imply that a small parcel of fluid oscillates about its initial position with angular frequency N in a gravitationally stable manner that facilitates density stratification. A neutrally stable outer core is characterized by the equivalent conditions N^2=0 and η_B=1 since N^2=$\rho g^2(\eta_B - 1)/\kappa$.

2.2. Geometric parameterization

The geometric parameterization of a radial reference model with depth strongly influences its structural complexity, flexibility for statistical tests and the rate of convergence towards an optimal solution. A modular description of radial models in terms of discrete principal regions is favorable due to its parametric simplicity and the ease of perturbing a particular feature independently of other parameters in the inversion (Table 1). The 10 principal regions in REM1D occupy discrete ranges of depths - ocean (OCE, 0–3 km), upper crust (UCR, 3–15 km), lower crust (LCR, 15–24.4 km), upper mantle (UUM, 24.4–410 km), transition zone (TZO, 410–650 km), central lower mantle (CLM, 771–2741 km), D″ region (DPP, 2741–2891 km), outer core (OCO, 2891–5156 km), and inner core (ICO, 5156–6371 km). Radii of internal discontinuities between the principal regions and the mean Earth radius (R = 6371 km) are fixed throughout this paper. Within each region, different sets of analytical basis functions are used to geometrically parameterize the variations at depth. Basis functions adopted in this study include (i) polynomial terms up to order 4 and (ii) 7 evenly-spaced cubic B-splines restricted to the upper mantle. Linear combinations of analytical functions vary between physical parameters (eq. 1) due to historical reasons, prior expectations from mineral physics and based on the sensitivity afforded by the reference bulk Earth datasets (Paper I). For example, η_B artifacts that imply strong inhomogeneity and non-adiabaticity are avoided in potentially well-mixed regions like the outer core by adopting a higher order polynomial for density than the elastic structure (cf. Section 4.1.4 in Paper I). Flexibility in parametrization allows us to isolate the influence of specific features and determine the level of structural complexity justified by available datasets. Both absolute values of physical parameters and important derivative properties (e.g. η_B, κ') can be evaluated in high precision without the need for numerical interpolation.

Radial inversions can solve either for absolute ($\oplus^{abs}$) or relative ($\oplus^{rel}$) perturbations to values in the starting reference model ($\oplus_0$). The first approach allows a simpler expression for an updated radial model $\oplus^{1D}$ as

$$\oplus^{1D}(r) = \oplus_0(r) + \oplus^{abs}(r). \tag{13}$$

Such expressions for absolute perturbations have been used in the construction of classical radial models like PREM and the attenuation model QL6 (Durek and Ekström, 1996). We express both the starting model $\oplus_0$ and absolute perturbations $\oplus^{abs}$ in terms of the same set of analytical basis functions. When expressed using a set of piecewise continuous functions along Earth's radius (B_h, Table 1), the starting radial reference model can be written as

$$\oplus_0(r) = \sum_h c_h^{m_k} B_h(r), \tag{14}$$

where $c_h^{m_k}$ corresponds to the coefficient for the h-th function from the basis set and the k-th parameter m_k out of the 8 physical parameters in eq. 1. An alternative to analytical functions and a less modular approach is to express the variations as a sequence of linear gradients or values at

discrete depths (e.g. AK135; Kennett et al., 1995). Another approach for constructing radial models uses relative ($\oplus^{\mathrm{rel}}$) perturbations defined as

$$\oplus^{\mathrm{1D}}_{\mathrm{avg}}(r) = \int_{\Omega} \oplus^{\mathrm{3D}}(r,\theta,\phi)\, d\Omega, \tag{15}$$

where $d\Omega$ is the differential surface area on the unit sphere at the latitude θ, longitude ϕ, and radius of interest r. Here, the heterogeneity field for each physical parameter is defined as

$$\oplus^{\mathrm{3D}}(r,\theta,\phi) = \oplus_0(r)\left[1 + \oplus^{\mathrm{rel}}(r,\theta,\phi)\right], \tag{16}$$

where $\oplus^{\mathrm{rel}}$ denotes the perturbation relative to the radial reference model $\oplus_0$. An example of a radial model constructed using this approach is STW105, which was derived as the spherical average of a 3D tomographic model (Kustowski et al., 2008).

2.3. Regularization and inversion

We solve for the absolute perturbations $\oplus^{\mathrm{abs}}$ to a starting reference Earth model $\oplus_0$ since it preserves the modular construction of the starting model. Our procedure involves inversion for absolute perturbations to a starting reference model

$$\oplus^{\mathrm{abs}} = \delta m_k(r) = \sum_h \delta c_h^{m_k} B_h(r) Y_{00}, \tag{17}$$

where $\delta c_h^{m_k}$ is perturbation to the coefficient $c_h^{m_k}$ corresponding to the k-th parameter m_k and h-th basis function B_h while Y_{00} denotes value of the degree-0 spherical harmonic ($1/\sqrt{4\pi}$ in our normalization). The use of polynomials and cubic B-splines in this study permit a radial regionalization with abrupt internal discontinuities. Paper I describes the basis functions and the *a priori* constraints from recent studies that are incorporated in the starting model ($\oplus_0$) in more detail. The model vector in our inverse problem ($\mathbf{m}$) therefore comprises the perturbations needed to the basis coefficients ($\delta c_h^{m_k}$) to fit bulk reference datasets. We express our model vector in terms of isotropic (e.g. $\delta v_S = (\delta v_{SH} + \delta v_{SV})/2$) and anisotropic variations (e.g. $\delta a_S = \delta v_{SH} - \delta v_{SV}$) for both compressional- and shear-wave velocities. This choice allows us to modulate independently the complexity of variations in isotropic velocity and radial anisotropy.

The total data misfit (χ^2) is calculated for all reference bulk Earth datasets (Section 2.4). We relate the data vector $\mathbf{d}$ to the model vector $\mathbf{m}$ using linearized sensitivity kernels (e.g. Supplementary Fig. S1) following $\mathbf{Gm} = \mathbf{d}$ based on the formulations in Paper I. The inversion is stabilized with prior information from regularization schemes, which can be expressed as a general matrix formulation $\mathbf{D}\left(\mathbf{m} + \delta^{abs}\mathbf{m}_0\right) = c$. Here, $\mathbf{m}_0$ is the starting model, c is a constant, and δ^{abs} dictates whether absolute properties (i.e. $\mathbf{m}_0 + \mathbf{m}$, δ^{abs}=1) rather than perturbations (i.e. $\mathbf{m}$, δ^{abs}=0) are regularized. Following discrete inverse theory (e.g. Menke, 1989), solution to the regularized inverse problem is

$$\mathbf{m}_{\mathrm{LS}} = \left[\sum_i w_i\left(\mathbf{G}^T\mathbf{G}\right)_i + \sum_j \gamma_j\left(\mathbf{D}^T\mathbf{D}\right)_j\right]^{-1}\left[\sum_i w_i\left(\mathbf{G}^T\mathbf{d}\right)_i - \sum_j \gamma_j\left(\delta^{abs}.\mathbf{D}^T\mathbf{D}\mathbf{m}_0 - \mathbf{D}^T c\right)_j\right], \tag{18}$$

where $\mathbf{m}_{\mathrm{LS}}$ is a matrix containing the best-fitting model while w_i and γ_j are the weights given to various types of data and damping, respectively. Also, j corresponds to different regularization choices in our models and $\left(\mathbf{D}^T\mathbf{D}\right)_j$ are the respective damping matrices derived numerically (cf. Appendix A in Paper I). We calculate the weighted least-squares solution to eq. 18 using a standard Cholesky factorization for positive-definite matrices (e.g. Trefethen and Bau, 1997). We perform standard damped least-squares inversions and select an appropriate amount of damping for every principal region in the Earth. The optimal damping scheme is adjusted separately for different physical parameters after successive trials and evaluations of our results.

We adopt a computationally intensive procedure that calculates *a posteriori* fits to a suite of radial models obtained using various amounts and types of regularization schemes. Our cascading scheme involves three sets of inversions with increasing parametric complexity - (i) mantle shear attenuation (Q_μ), (ii) mantle Q_μ and elastic variations, (iii) mantle η and ρ including all parameters in the previous set, and finally (iv) all mantle and core parameters. The strongest sensitivity of the reference datasets are to the shear-velocity and shear-attenuation structure in the mantle (e.g. Supplementary Fig. S1); we solve these parameters initially to obtain faster convergence in data fits. The second set of inversions is done jointly for several iterations and accounts for the effects of attenuation on mode eigenfrequencies due to physical dispersion (cf. eq. 16 in Paper I). From the third step onwards, astronomic-geodetic and body-wave measurements are included. Each step in our inversion procedure comprises up to five iterations of calculating sensitivity kernels accounting for crustal structure in case of surface waves and the corresponding normal modes (cf. eq. 13 and 14 in Paper I), followed by accumulation of data sensitivities from different datasets and joint inversions for radial structure (eq. 18). The incremental approach of adding structural complexity and reference datasets in our inversions allows us to trace and control the contributions from different subsets of data.

2.4. Fits to bulk earth datasets

Our preferred radial reference Earth model (REM1D) is constructed from a rigorous evaluation of structural complexities based on optimal fits to bulk Earth datasets (Table 1, Fig. 1). In Paper I, we derived reference datasets comprising normal-mode eigenfrequencies and quality factors, surface-wave dispersion curves, impedance constraints and arrival-time curves from body waves, and Earth's mass and moment of inertia. A crucial goal of a new reference Earth model is to afford more accurate predictions of all data types compared to earlier radial models. Other models considered here were constructed either with older reference datasets (e.g. PREM, AK135F) or a subset of data types such as normal modes (EPOC) and body waves (SP6, AK135, CCREM, KHOMC, EK137). EPOC (Irving et al., 2018) and KHOMC (Kaneshima and Helffrich, 2013) report changes in properties of the outer core and retain values from PREM in other regions. EPOC prescribes an isentropic EoS formulation (Vinet et al., 1987) to fit a small dataset of normal-mode eigenfrequencies with associated estimates of molar mass, pressure and gravity in the outer core; such a parameterization assumes a well-mixed, adiabatic region *a priori* in the inversion. EK137 (Kennett, 2020) aims to fit arrival times of body wave phases by updating a combination of the AK135 mantle and EPOC core. KHOMC (Kaneshima and Helffrich, 2013) reports changes to v_P variations in the PREM outer core based on differential times between the SmKS phases (i.e. m = 2 for SKKS) with different numbers of underside reflections (m-1) at the core–mantle boundary. CCREM (Ma and Tkalčić, 2021) is optimized to fit the correlation features that exist in global correlograms due to the similarity of body waves reverberating through the Earth's interior. STW105 (Kustowski et al., 2008) is an elastic model that was derived as the spherical average of a 3D tomographic model using older datasets

Table 2
Comparison of fits to the normal-mode datasets. The χ^2/N misfits to the reference dataset of eigenfrequencies (ω) and quality factors (Q) are provided separately for radial modes, spheroidal and toroidal fundamental modes, or their overtone branches. Average dispersion curves of surface waves are converted to mode eigenfrequencies in these calculations. In the case of REM1D, non-linear crustal contributions are included in the predictions for eigenfrequencies of fundamental modes (Paper I). Subsets of spheroidal overtones are sensitive to v_P or core structure. Studies that do not solve for attenuation profiles are denoted by a "†"; shear and bulk attenuation parameters from either QL6 (in case of STW105) or PREM (in case of others) are used to account for physical dispersion in these models. Models that did not employ normal modes and surface waves in their construction are denoted by "∧" and "§", respectively. EPOC (v_P, ρ) and KHOMC (v_P) are outer-core models that prescribe PREM structure in other regions and for the remaining physical properties (Section 2.4). Data fits comparable to PREM afforded by these two studies are therefore a natural outcome of this modeling limitation. Fits afforded by REM1D to individual normal modes are listed in Supplementary Tables S2–S6. Some of the values below are noted in the legends of Figs. 3 and 4.

χ^2/N	Radial	Spher. Fund.	Tor. Fund.	Spher. Over.	Tor. Over.	Subsets of Spheroidal Overtones			All Modes
	Q | ω	Q | ω	Q | ω	Q | ω	Q | ω	v_P sens.	Core	Other	Q | ω
REM1D	15 | 377	2 | 8	2 | 2	19 | 44	2 | 3	25 | 49	13 | 141	19 | 31	11 | 32
PREM	41 | 215	1 | 110	8 | 131	28 | 165	21 | 3	26 | 196	18 | 286	36 | 146	18 | 120
AK135F	1087 | 23,493	2 | 675	3 | 2312	96 | 2142	7 | 42	192 | 5202	63 | 7742	45 | 1020	85 | 1946
STW105†^	43 | 112	1 | 70	2 | 479	24 | 231	2 | 29	30 | 526	22 | 474	22 | 161	14 | 194
EPOC†§	40 | 3240	1 | 93	8 | 131	28 | 103	21 | 3	28 | 78	18 | 368	35 | 72	18 | 142
AK135†§^	85 | 1521	52 | 2798	99 | 20,422	125 | 878	75 | 103	187 | 3371	30 | 2613	144 | 304	100 | 3057
CCREM†§^	90 | 1418	76 | 4527	101 | 27,011	125 | 415	80 | 30	185 | 817	30 | 772	146 | 313	106 | 3692
KHOMC†§^	41 | 1135	1 | 326	8 | 2843	28 | 117	21 | 11	27 | 216	18 | 313	35 | 77	18 | 432
EK137†§^	85 | 1052	52 | 2056	99 | 28,885	2356 | 1162	75 | 12	1251 | 1602	2497 | 2918	3071 | 874	1244 | 4026

and excluding the constraints from normal modes. All radial models except PREM and AK135F report elastic properties and density with no independent descriptions of anelastic structure (Q_μ, Q_κ). All earlier models ignore the effects of azimuthal anisotropy during model construction while only PREM, AK135F and STW105 account for radial anisotropy. Overall, REM1D provides revised estimates of all physical properties (Fig. 1, Table 1) and affords better fits to the new reference datasets than all classical and widely used radial models that are available from the literature. While improvements with REM1D is not altogether surprising, a simple fitting exercise based on classical approaches was found inadequate so new concepts for jointly modeling the diverse datasets had to be developed for this outcome (Paper I).

Table 2 demonstrates the improvement in χ^2/N misfits for various subsets of normal modes. In order to aid comparisons, average dispersion curves of surface waves are converted to eigenfrequencies of fundamental modes following Paper I. REM1D fits fundamental (spheroidal and toroidal) modes and v_P-sensitive overtones up to 65 times better than PREM. Since the reference datasets span the full spectrum of seismological observations (~1–3200 s), attenuation profiles (Q_μ, Q_κ) from PREM are adopted to account for physical dispersion in the predictions from body-wave models that do not report these parameters (AK135, CCREM, KHOMC, EK137). All body-wave models report up to two orders of magnitude worse χ^2/N misfits to normal-mode and surface-wave datasets compared to REM1D. Figs. 3 and 4 demonstrate the capability of REM1D to reproduce the trends in eigenfrequency and quality-factor data along various overtone branches indicative of the improved constraints on shallow Earth structure. REM1D is the only model that fits all astronomic-geodetic data to within their 1-σ bounds ($|\chi| \leq 1$) of uncertainty (Fig. 5, Supplementary Table S1). Improvements in fits to normal-mode, astronomic-geodetic and surface-wave data are obtained in conjunction with robust fits to the body-waves arrival times (Table 3) and contrasts across internal discontinuities (Table 4, Section 3.2). Normalized misfits to body-wave arrivals from REM1D are very low ($\psi_{pb} \leq 0.25$ s) across a range of phases and distances (Table 3), which is comparable in magnitude to the misfits from body-wave models (e.g. AK135, CCOMC, KHOMC). While predictions from SP6 are used for calculating these misfits (Paper I), discrepancies with other arrival times (e.g. Kennett et al., 1995; Kennett, 2020) are uniformly low ($\ll 0.5$ s) except for a few phases where the geographic bias to structure in the shallowest mantle and D″ region (e.g. S, P, ScS and SKKS; Supplementary Fig. S2) is accounted for in this work.

Fig. 6 demonstrates the excellent fits to average surface-wave dispersion curves that could be achieved only after performing iterative inversions that account for non-linear crustal contributions. The influence of heterogeneity from the crustal model CRUST2.0 (Bassin et al., 2000) is substantial (> 50 %) for phase velocities of both Love and Rayleigh waves. At least three iterations are needed before inversions of elastic structure converge in their fits to surface wave dispersion. Since local phase velocities are calculated for CRUST2.0 at every iteration (Paper I), fitting the dispersion curves is a computationally intensive and strongly non-linear procedure. REM1D predicts average dispersion to within the 1-σ uncertainty bounds across the entire range of surface-wave periods considered in this study (25–250 s). PREM predicts substantially slower phase velocities (by up to ~1.2 %) for the short-period (< 50 s) Love waves and all Rayleigh waves. Since we account for physical dispersion while fitting mode eigenfrequencies (cf. eq. 16 in Paper I), the attenuation parameters also influence the retrieved elastic structure. Robustness of the REM1D shear and bulk attenuation model (Section 3.1) is evident based on (up to 10 times) lower χ^2/N misfits than PREM to the quality factor observations of normal modes (Table 2, Figs. 3 and 4).

Revisions in density structure are needed to reconcile two major subsets of the reference dataset. First, REM1D satisfies the astronomic-geodetic constraints (Fig. 5, Supplementary Table S1) with positive density gradients ($d\rho/dz$) throughout the upper mantle and slight reductions in density within the outermost outer core (Fig. 2d,g). In contrast, PREM systematically over predicts the new and more precise estimates of Earth's total mass and inertia coefficient ($\chi^2/N = 21$). Second, eigenfrequencies of long-period spheroidal modes require steeper gradients of density in the lower mantle with 0.2–0.3 % denser material than PREM at the bottom ~500 km of the mantle (Fig. 2g). Several long-period normal modes (e.g. ${}_0S_{2-5}$) that afford comparable sensitivity to elastic parameters and density in the mantle (e.g. Dahlen and Tromp, 1998, cf. Supplementary Fig. S1 in Paper I) require this feature of geological significance (Sections 4.5 and 4.6). Density excess in the outer core reported by EPOC relative to PREM (> 1 %, Fig. 7c,d) is highly inconsistent with astronomic-geodetic observations ($|\chi| = 13–79$, Supplementary Table S1).

Fig. 8 summarizes fits to the arrival times of a few mantle and core phases that were used in the construction of REM1D. PREM predicts faster arrivals (>1 s) of the diffracted phases P_{diff} and S_{diff} than the radial model SP6 due to the geographic bias towards the faster lower-mantle

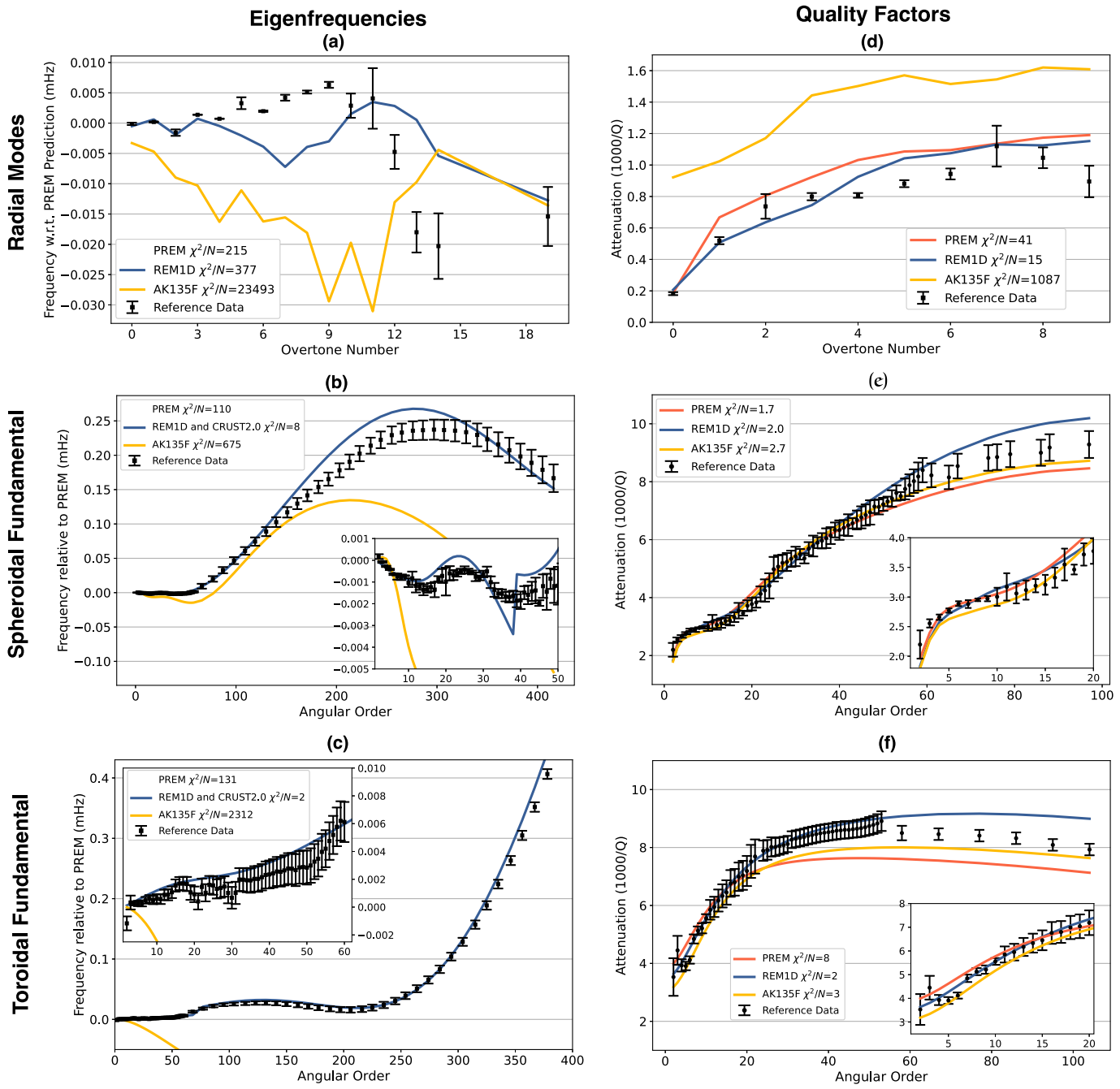

Fig. 3. Fits to eigenfrequencies (a–c) and quality factors (d–f) of radial and fundamental normal modes. Predictions from REM1D (blue) include the non-linear contribution from the crust following eqs. 13 and 14 in Paper I. The χ^2/N misfit values are provided in the legend for the models REM1D, AK135F and PREM. For clarity, eigenfrequencies (a–c) are plotted relative to the values predicted by PREM. Average dispersion curves of surface waves are converted to mode eigenfrequencies in these calculations following Paper I. Fits afforded by REM1D to individual normal modes are listed in Supplementary Tables S2–S4.

anomalies in the northern hemisphere (e.g. Paper I; Morelli and Dziewonski, 1993). According to ray theory, arrival times of these teleseismic body waves have a peak sensitivity at the turning point of the ray in the bottom 200–300 km of the mantle (Fig. 9). We start with a low-velocity zone in the D″ region (Paper I) and the negative gradients in both v_P and v_S structure persist even with the inclusion of normal mode eigenfrequencies and after performing several iterations of joint inversions. Compared to PREM, REM1D is up to 0.5 % slower in v_P and up to 1 % slower in v_S in the D″ region primarily due to the arrival times of diffracted waves (Fig. 2g). Normal-mode overtones that afford additional sensitivity to the lower mantle (Supplementary Fig. S1) are fit significantly better by REM1D with up to 4 times lower χ^2/N misfits compared to PREM (Fig. 4a-f). Core structure is constrained using long-period ($\geq$ 50 s) normal-mode measurements and arrival times of core-traversing phases (e.g. PKIKP, SKS) recorded at shorter periods (~1–50 s). Arrival-time predictions of all core phases (i.e. PKIKP, PKKP, PKP, SKKS, SKS, SKIKP and P′P′) are consistent ($\pm$ 0.8 s, $\psi_{pb} \leq$ 0.25 s) with the reference dataset of SP6 values (Fig. 9a, Table 3). In contrast, PREM predicts faster arrivals (up to 6 s) than REM1D for the core phases SKS and SKKS (Fig. 9c,d), which is inconsistent with arrival time curves of both AK135 and SP6. Differential times between the SmKS phases (m = 2–5; e.g. SKKKS-SKKS) provide sensitivity to the outermost ~800 km of the core. Although excluded from our inversions, discrepancies in differential SmKS times (m = 1–5) predicted by REM1D and KHOMC (<

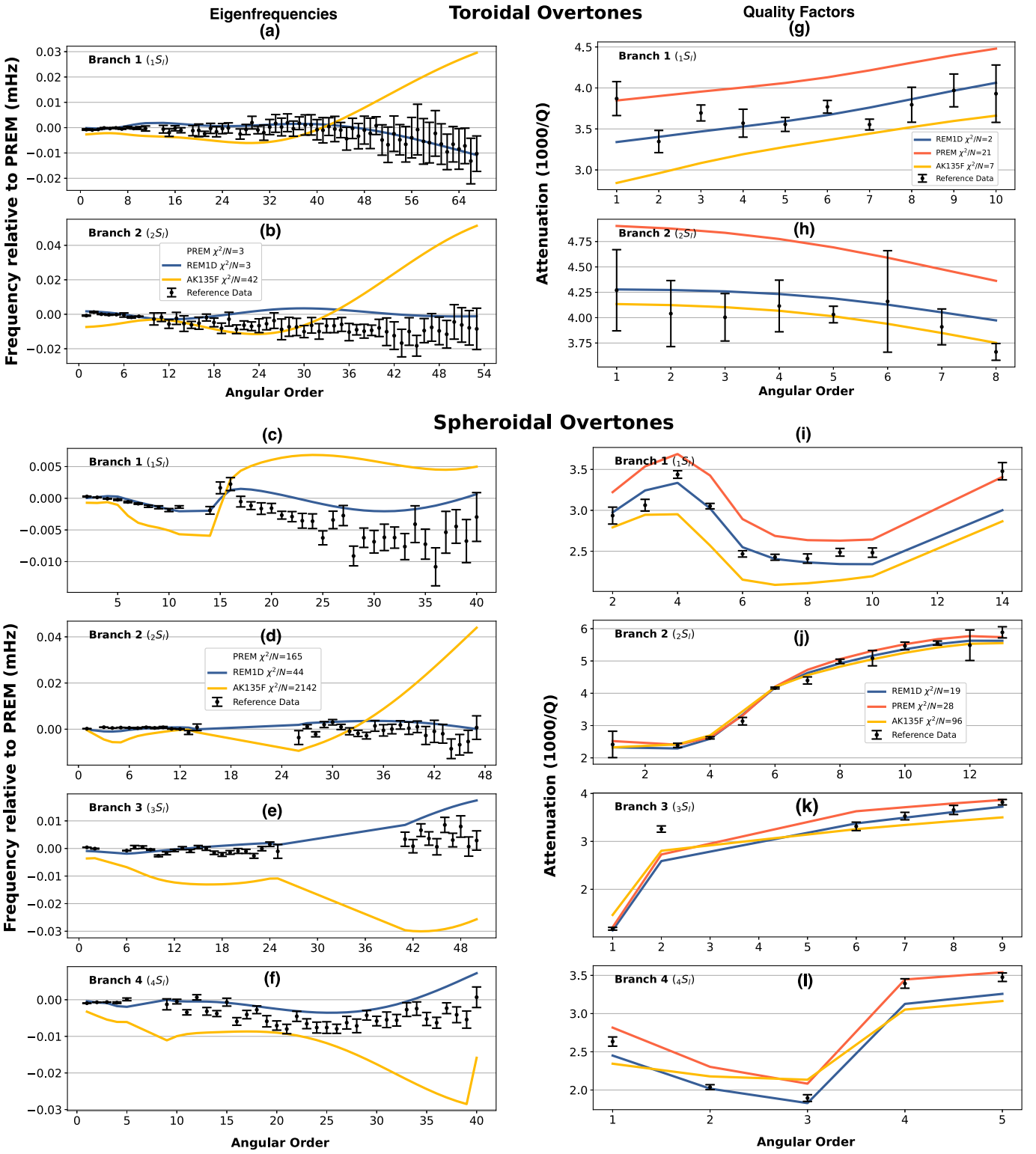

Fig. 4. Fits to eigenfrequencies (a–f) and quality factors (g–l) of toroidal and spheroidal overtones. Note the full description in Fig. 3. All overtone branches are not plotted here for clarity but discussed in the text. Fits afforded by REM1D to individual normal modes are listed in Supplementary Tables S5 and S6.

0.4 s) at distances between 125°–165° from a deep-focus earthquake (500 km hypocenter depth) do not exceed the reported uncertainty and scatter in array studies (e.g. Alexandrakis and Eaton, 2010; Kaneshima and Helffrich, 2013; Kaneshima, 2018). While a model like KHOMC can be optimized to fit differential SmKS times, it is overall too fast in the shallow outer core (down to ~4000 km depth; Fig. 7b) to fit arrival times of PKP phases that are incorporated in REM1D (Table 3).

While REM1D affords better overall fits to reference datasets than PREM, some outliers persist due to, (i) unrealistic uncertainty bounds for the reported measurements, (ii) tradeoffs between different types of reference datasets, and (iii) theoretical limitations such as ignoring the effects of radial anisotropy on observations. Of particular note are the high-overtone radial modes ($_{3-9}S_0$), which are equivalent to radially propagating PKIKP waves and are sensitive to v_P variations in the whole

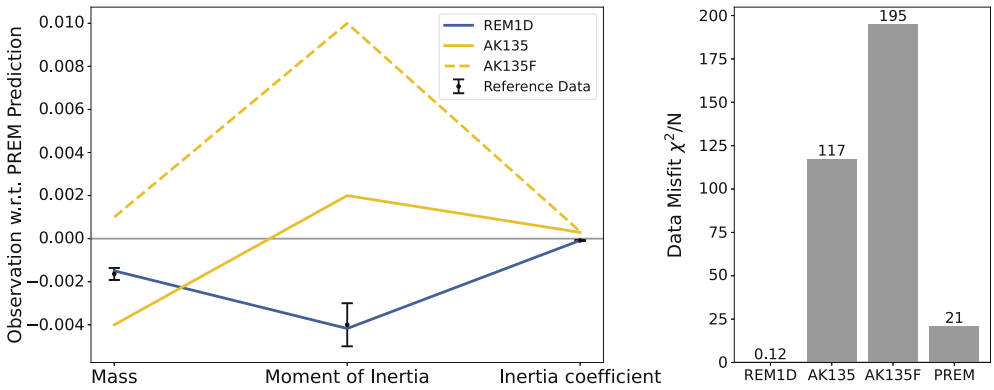

Fig. 5. Fits to the reference astronomic-geodetic data. For clarity, all observations from Paper I and model predictions are plotted relative to the value predicted by PREM. The cumulative χ^2/N misfits are provided for various radial models - PREM, AK135, AK135F and REM1D - demonstrating the significant misfit reduction with this study. Predictions from other radial models and detailed measures of data fit are provided in Supplementary Table S1.

Table 3

Comparison of fits to arrival times of body-wave phases. Normalized misfit is defined as $\psi_{pb} = \frac{1}{1+\Delta_2-\Delta_1}\left[\chi^2_{pb}\right]^{1/2}$ where χ^2 fits for each phase (p) and branch (b) are calculated using eq. 19 in Paper I. Body-wave travel times are obtained at the corresponding components and range of great-circle distances $\Delta = [\Delta_1,\Delta_2]$ sampled at 1° intervals. The arrivals of S, SS and ScS are associated with the transverse (T) component while other phases are associated with the vertical (V) component. Radial models that did not employ body waves in their construction are denoted by a "†". Values in the upper crust are extended to the surface and ocean is removed when a global ocean layer is reported in models denoted by a "*". Rays are calculated through all profiles at the reference period of 1 s without corrections for physical dispersion while using an anisotropic tracer modified from Woodhouse (1981). The source is a surface-focus earthquake located at the equator (0°, 0°) and no ellipticity correction is applied. Large normalized misfits ($\psi_{pb} > 0.25$ s) are underlined for clarity.

Phase	Great-circle Distance Δ	Normalized Misfit (ψ_{pb}) of Radial Models								
		REM1D*	PREM*	AK135	AK135F	EK137	CCREM	KHOMC	EPOC*†	STW105*
P	27°–125°	0.05	0.15	0.06	0.10	0.04	0.04	0.15	0.15	0.12
S	27°–125°	0.06	0.23	0.25	0.24	0.20	0.23	0.23	0.23	0.22
PP	53°–180°	0.03	0.12	0.02	0.21	0.02	0.06	0.12	0.12	0.07
SS	56°–150°	0.14	0.11	0.07	0.54	0.09	0.14	0.11	0.11	0.06
PcP	26°–70°	0.03	0.14	0.04	0.17	0.02	0.05	0.14	0.14	0.08
ScS	19°–65°	0.07	0.09	0.14	0.32	0.10	0.12	0.09	0.09	0.08
ScP	18°–62°	0.04	0.10	0.08	0.25	0.06	0.07	0.10	0.10	0.06
SP	95°–128°	0.13	0.19	0.08	0.54	0.04	0.18	0.19	0.19	0.23
PKIKP	118°–180°	0.04	0.19	0.02	0.17	0.04	0.06	0.16	0.10	0.13
PKP_{ab}	156°–178°	0.06	0.44	0.06	0.24	0.03	0.05	0.39	0.15	0.35
PKP_{bc}	151°–153°	0.25	0.79	0.11	1.07	0.04	0.05	0.65	0.34	0.48
$PKKP_{ab}$	111°–122°	0.03	0.67	0.04	0.42	0.06	0.01	0.53	0.12	0.55
$PKKP_{bc}$	83°–122°	0.10	0.22	0.04	0.25	0.01	0.03	0.16	0.05	0.16
SKS	91°–123°	0.14	0.15	0.08	0.47	0.08	0.08	0.12	0.11	0.13
SKKS	65°–178°	0.09	0.32	0.08	0.26	0.16	0.13	0.24	0.13	0.30
SKIKP	113°–160°	0.01	0.19	0.07	0.27	0.08	0.09	0.16	0.08	0.14
SKP_{bc}	141°–148°	0.02	0.31	0.07	0.78	0.10	0.09	0.23	0.08	0.19
P′P′	56°–70°	0.10	0.47	0.02	0.50	0.02	0.08	0.39	0.13	0.30

Earth (cf. Supplementary Fig. S1 in Paper I). These modes are fit poorly by both REM1D and PREM with χ^2/N misfits to eigenfrequencies exceeding 300 even though the remaining radial modes are fit at least 10 times better with REM1D. While eigenfrequencies of radial modes are measured with high precision due to their large quality factors (Fig. 3d) and the related slow decay in amplitudes, it is not clear whether uncertainties lower by 2 orders of magnitude are justified for a subset of these modes (Supplementary Table S2). Tradeoffs between body-wave and normal-mode datasets are present while fitting the shear velocities in the mantle. A radial model constructed with normal modes in isolation prefers v_S variations that are up to 15 m/s slower than REM1D down to a depth of ~800 km. This leads to a slightly more pronounced low-v_S zone in the shallowest mantle (80–250 km) and slower velocities in the uppermost lower mantle (650–771 km), regions that strongly influence the propagation of S and SS phases. By optimizing the v_S structure in joint inversions, REM1D is able to fit arrivals of major body-wave phases without substantially deteriorating the fits (< 1.5 times) to eigenfrequencies afforded by the mode-only inversions (Table 5). Only the SS phase persists as an outlier (> 0.8 s) in data fits between SP6 and REM1D, especially at epicentral distances shorter than 90° (Fig. 9). Discrepancies of a similar magnitude can be caused by the effects of radial anisotropy and the biased sampling of continental regions that is

Table 4
Model estimates of contrasts in elastic parameters and density across internal discontinuities. We define the contrast as $\%\Delta x = 100 \times \Delta x/x_{avg}$, where $\Delta x = |x_+ - x_-|$ is the magnitude of difference between parameters at the top (subscript '+') and bottom (subscript '–') of the discontinuity and $x_{avg} = [x_+ + x_-]/2$ is the average. Parameter x can be density ρ, shear modulus μ, Lamé parameter λ, shear-wave velocity (v_S) and impedance (Z_S), compressional-wave velocity (v_P) and impedance (Z_P), and bulk-sound velocity (v_Φ). Reference dataset with uncertainties are discussed in Paper I. Estimates from REM1D and other classical radial models are provided for comparison. Discrepant predictions that fall outside bounds of the uniform distribution or the 95 % confidence interval (2-σ) of the normal distribution are underlined. At the 650-km discontinuity, PREM overestimates the impedance contrasts while REM1D detects negligible changes in both v_Φ and λ. ICB represents the inner-core boundary that is fixed at a radius of 1215 km in REM1D.

Discontinuity	Parameter[§]	Reference	Model Estimates			
		Data	REM1D	PREM	AK135	SP6
410 km $\alpha\rightarrow\beta$	$\%\Delta v_P$	2.5–4.8	2.5	2.5	3.6	3.7
	$\%\Delta v_S$	3.4–5.4	3.4	3.4	4.2	4.5
	$\%\Delta\rho$	3.9–5.0	4.9	5.0	3.3	5.3
	$\%\Delta Z_P$	7.5 ± 2.2	7.4	7.5	6.9	9.1
	$\%\Delta Z_S$	8.3 ± 1.6	8.3	8.3	7.6	9.8
	$\%\Delta\lambda$	–	7.2	7.8	8.7	10.6
	$\%\Delta v_\phi$	–	1.9	2.0	3.2	3.2
650 km $\gamma \rightarrow$ pv + pc	$\%\Delta v_P$	0.7–2.5	2.5	4.6	5.6	5.3
	$\%\Delta v_S$	4.8–8.5	6.3	6.5	6.1	6.2
	$\%\Delta\rho$	5.2–6.2	5.3	9.3	5.3	7.9
	$\%\Delta Z_P$	7.2 ± 2.1	7.8	13.9	10.9	13.2
	$\%\Delta Z_S$	10.0 ± 1.4	11.6	15.8	11.3	14.2
	$\%\Delta\lambda$	–	1.1	12.8	15.2	15.5
	$\%\Delta v_\phi$	–	0.0	3.4	5.3	4.6
ICB	Δv_S (km s^{-1})	2.5–3.5	3.5	3.5	3.5	3.5
	$\Delta\rho$ (g/cm^3)	0.5–0.9	0.6	0.6	0.6	0.6

[§] For small contrasts in properties, $\%\Delta Z_S = \%\Delta v_S + \%\Delta\rho$ and $\%\Delta Z_P = \%\Delta v_P + \%\Delta\rho$.

ignored in most body-wave models (Paper I).

A way to improve constraints on the lowermost mantle and the D″ region (Section 4.6) is by including expanded datasets of diffracted body waves (P_{diff}, S_{diff}) and the so-called Stoneley modes trapped at the core-mantle boundary (e.g. Ritsema et al., 2011; Koelemeijer et al., 2013). While we have included average travel times of diffracted phases that account for the uneven geographic coverage (Paper I), newer observations afforded by array deployments of broadband seismometers (e.g. USArray) will likely yield insights on lateral variations. Our experiments with the mode eigenfrequencies of CMB-Stoneley modes reported by a single study (Koelemeijer et al., 2013) reveal that these data are fit substantially better with REM1D (χ^2/N ∼ 343) than PREM (χ^2/N ∼ 657). While the misfits are still quite large, they stem from outstanding discrepancies in only three modes ($_1S_{16}$, $_2S_{25}$ and $_3S_{26}$). The CMB-Stoneley modes are difficult to measure due to the limited

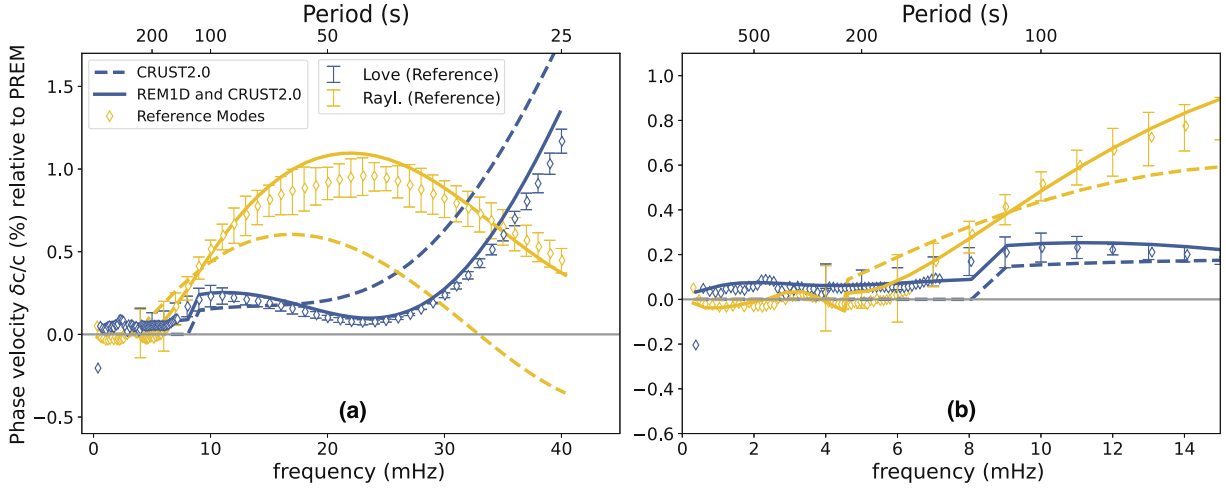

Fig. 6. Fits to the reference surface-wave dispersion dataset. (a) Predictions of average phase-velocity perturbations (dc/c) for Love (in blue) and Rayleigh (in yellow) waves between 25 and 250 s. (b) Zoomed in values at the longest periods of vibration (60–3200 s). Reference data of eigenfrequencies from Fig. 3b,c are converted to phase velocity perturbations to aid comparisons following eq. 12 in Paper I. Predictions from CRUST2.0 alone (dashed) and when combined with our preferred model REM1D (solid) are calculated following eq. 14 and 17 in Paper I. All values are plotted relative to the phase velocities predicted by PREM.

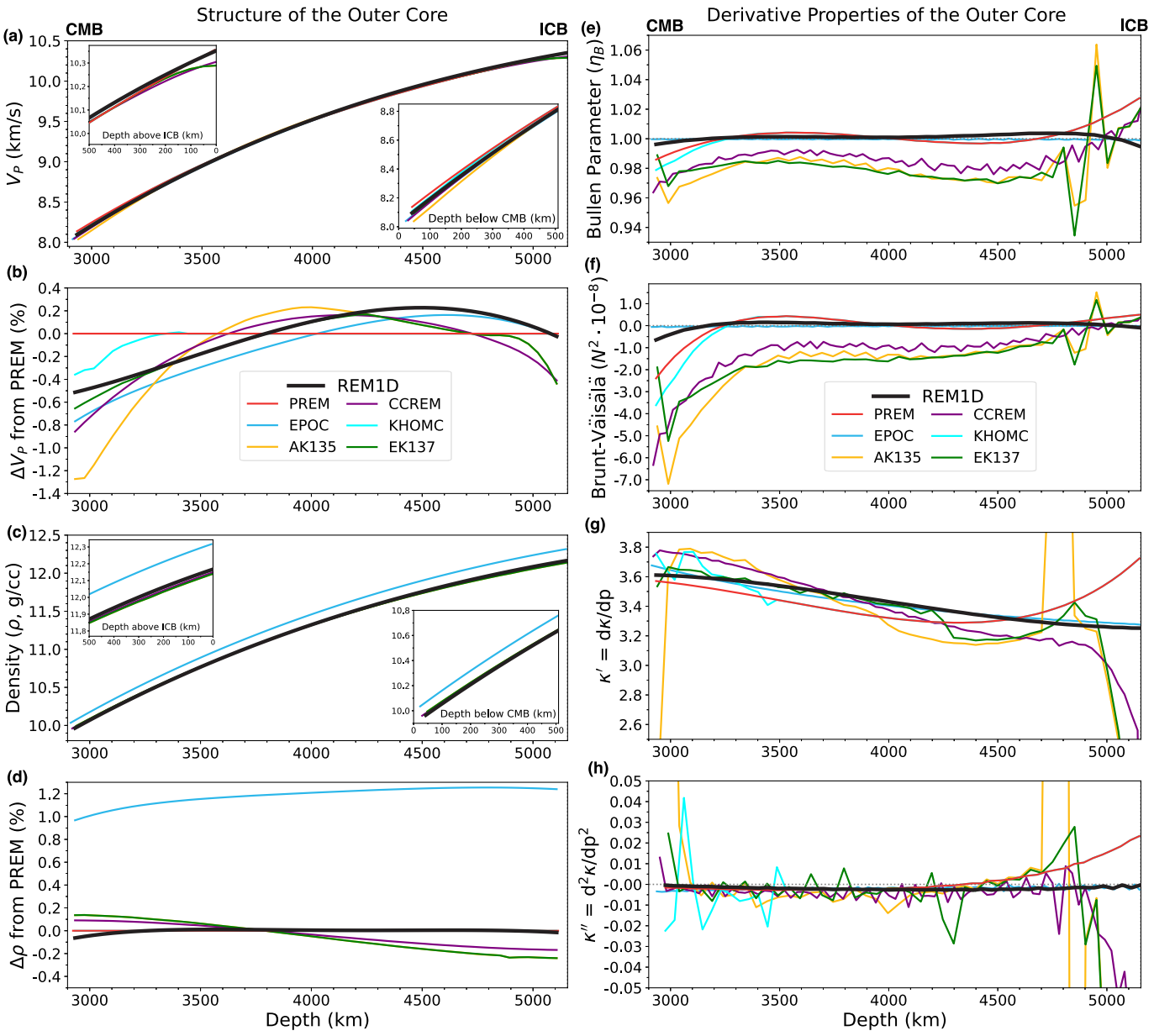

Fig. 7. Comparison of radial models in the outer core. (a,c) Absolute variations in v_P and ρ along with (b,d) deviations from PREM values are provided. Derivative properties include (e) Bullen's stratification parameter η_B, (f) Brunt-Väisälä frequency N^2, (g) gradient in bulk modulus with pressure $\kappa' = d\kappa/dp$ and (h) its curvature κ''. Inset figures (a,c) zoom in to the boundary regions of the outer core with a thickness of 500 km next to the CMB and ICB. REM1D reports steeper velocity and density gradients than PREM and up to 0.5 % lower velocities (v_P) in the outermost outer core. Density excess in the outer core reported by EPOC relative to PREM (> 1 %) is highly inconsistent with astronomic-geodetic observations ($|\chi| = 13$–79, Supplementary Table S1). REM1D detects η_B values close to one throughout the outer core with a smoothly decreasing κ' (i.e. negative κ''). REM1D can fit all reference datasets without the abrupt changes in v_P gradients at the base of the outer core reported by most body-wave models, which is related to the anomalous deviations in κ' and η_B with positive values of κ''. Our results are consistent with a neutrally stable outer core comprising a well-mixed iron alloy undergoing adiabatic compression (Section 4.9). Values of the physical properties from REM1D are listed in Supplementary Table S7.

displacements of their eigenfunctions on the Earth's surface and their strong resonance with other modes nearby in frequency. They also have limited sensitivity to density in the lowermost mantle and our inversions with a variety of density variations give comparable fits to the reported data. These measurements were obtained using a technique that iteratively fits a set of observed normal-mode spectra (ISF; e.g. Giardini et al., 1987, 1988; Li et al., 1991; Resovsky and Ritzwoller, 1998; Deuss et al., 2013), which is strongly non-linear and requires accurate descriptions of the earthquake source and radial structure. Alternative techniques are being formulated that may overcome such limitations (e.g. Masters et al., 2000b); REM1D fits current estimates better than PREM even though these data were not part of the reference dataset (Paper I) and are not employed during model construction.

3. Estimation of physical properties

In this section, we discuss the various structural complexities that were evaluated during the construction of REM1D (Table 1, Fig. 1). For brevity, we focus on a small subset of modeling scenarios that are most pertinent to the geological interpretations discussed later in the paper (Section 4). Key questions are regarding the major modifications needed to the classical radial reference models like PREM (Fig. 2).

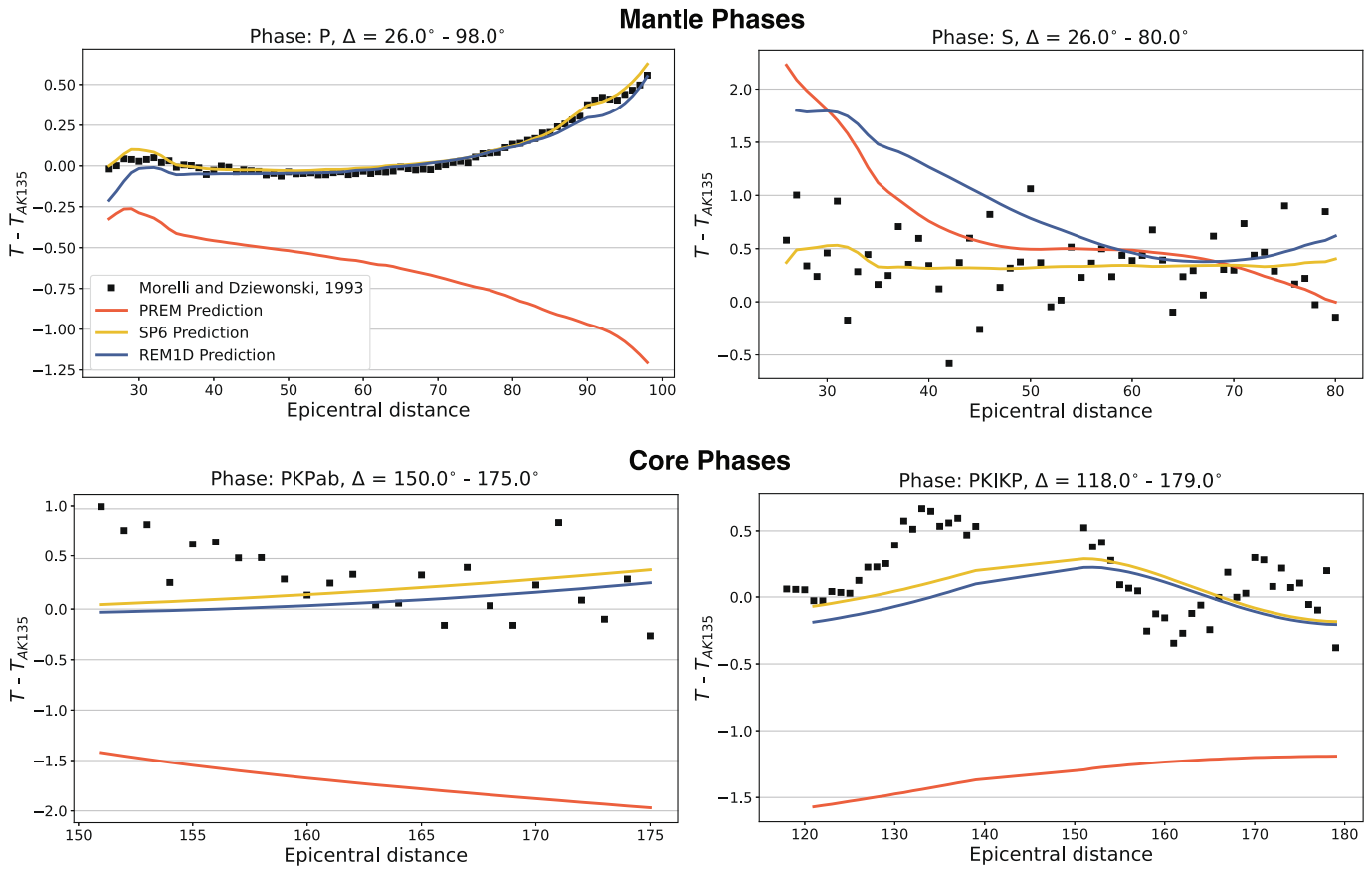

Fig. 8. Fits to summary arrival-time curves of body waves. Reference observations from Morelli and Dziewonski (1993) are provided in black. The source is a surface-focus earthquake located at the equator (0°, 0°) and no ellipticity correction is applied. All arrival times are plotted relative to predictions from the isotropic model AK135 to aid comparisons. REM1D removes the geographic bias towards faster v_P structure in the northern hemisphere present in PREM.

3.1. Shear and bulk attenuation

Fig. 10 summarizes trial inversions that evaluate shear attenuation structure in three isolated regions of the Earth's mantle: (i) upper mantle, (ii) lower mantle, and (iii) the D″ region. A suite of shear-attenuation (Q_μ) models is inverted using a regularization scheme that modulates the complexity of structure. We apply different levels of smoothness (γ_g) in the upper or lower mantle while another damping term (γ_d) modulates the step change in shear attenuation across the D″ discontinuity (Fig. 10a,b). We show results from the first iteration of an iterative scheme (Section 2.3), which eventually converges towards our preferred model of shear attenuation in the mantle (Fig. 1c, Table 1). Corresponding fits to the full compilation of quality-factor observations and the various subsets of normal modes are also reported (Fig. 10c–h). Shear attenuation in the upper mantle is constrained well by the large set of quality factor observations in our reference dataset (Paper I). In the vast majority of our models, the minimum in Q_μ corresponds to a strongly attenuating asthenosphere at a depth of ~150–175 km. This feature is favored by a majority of quality-factor observations, especially the fundamental (Rayleigh-wave equivalent) spheroidal and (Love-wave equivalent) toroidal modes. When strong attenuation (low Q_μ) in the uppermost mantle is suppressed with strong gradient damping, χ^2/N misfits to spheroidal modes deteriorate by as much as 30 (Fig. 10c). Substantial reductions in fits ($\Delta\chi^2$/N ~ 10) are also observed for the toroidal fundamental modes when low attenuation is imposed in the asthenosphere; in contrast, toroidal overtones and radial modes are less sensitive to details in the uppermost mantle (Fig. 10f). Overall, there is a clear need for enhanced shear dissipation in the uppermost mantle compared to PREM.

Several features of shear attenuation in the deep mantle are also evaluated in these experiments. REM1D exhibits constant shear attenuation in the lower mantle (Fig. 2e,f), with values closer to the attenuation model QL6 (Durek and Ekström, 1996) than PREM. When we allow more structural complexity in the lower mantle by reducing the weights for gradient damping, a gradual increase in shear attenuation (ΔQ_μ = 10–50) is observed between 650 and 2891 km depth (Fig. 10b). This increase in shear attenuation from the mid mantle is roughly in agreement with a previous normal-mode study (e.g. Widmer et al., 1991). When additional complexity is allowed by reducing the weights that modulate the step change at the D″ discontinuity, a low Q_μ of ~180–200 is recovered. A moderately high shear attenuation in the D″ region could be due to its role as a thermal or chemical boundary layer, and is broadly consistent with some body-wave analyses (Doornbos, 1974). However, analysis of data fits show no clear requirement for both of these complexities in the lower mantle in order to fit any subset of normal modes; χ^2/N misfits to the spheroidal modes do not improve substantially ($\Delta\chi^2$/N < 2–3) when gradient damping is relaxed in the lower mantle (Fig. 10d). Fits to toroidal overtones, which are sensitive to this region, deteriorate slightly ($|\Delta\chi^2/\mathrm{N}| \sim 1$) when the gradient damping is relaxed (Fig. 10g). Similar results are found for Q_μ in the D″ region; χ^2/N misfits do not improve substantially ($\Delta\chi^2$/N < 2) in models that permit strong attenuation ($Q_\mu \sim 170$) isolated at the base of the mantle (Fig. 10e,h). Overall, these experiments suggest that the reference datasets of quality factors are adequately fit by a constant and uniform Q_μ throughout the lower mantle.

Observed decay of radial normal modes requires a finite bulk dissipation ($Q_\kappa \ll \infty$) somewhere in the Earth but its radial variation has been a subject of debate. Table 5 lists the retrieved models of bulk attenuation

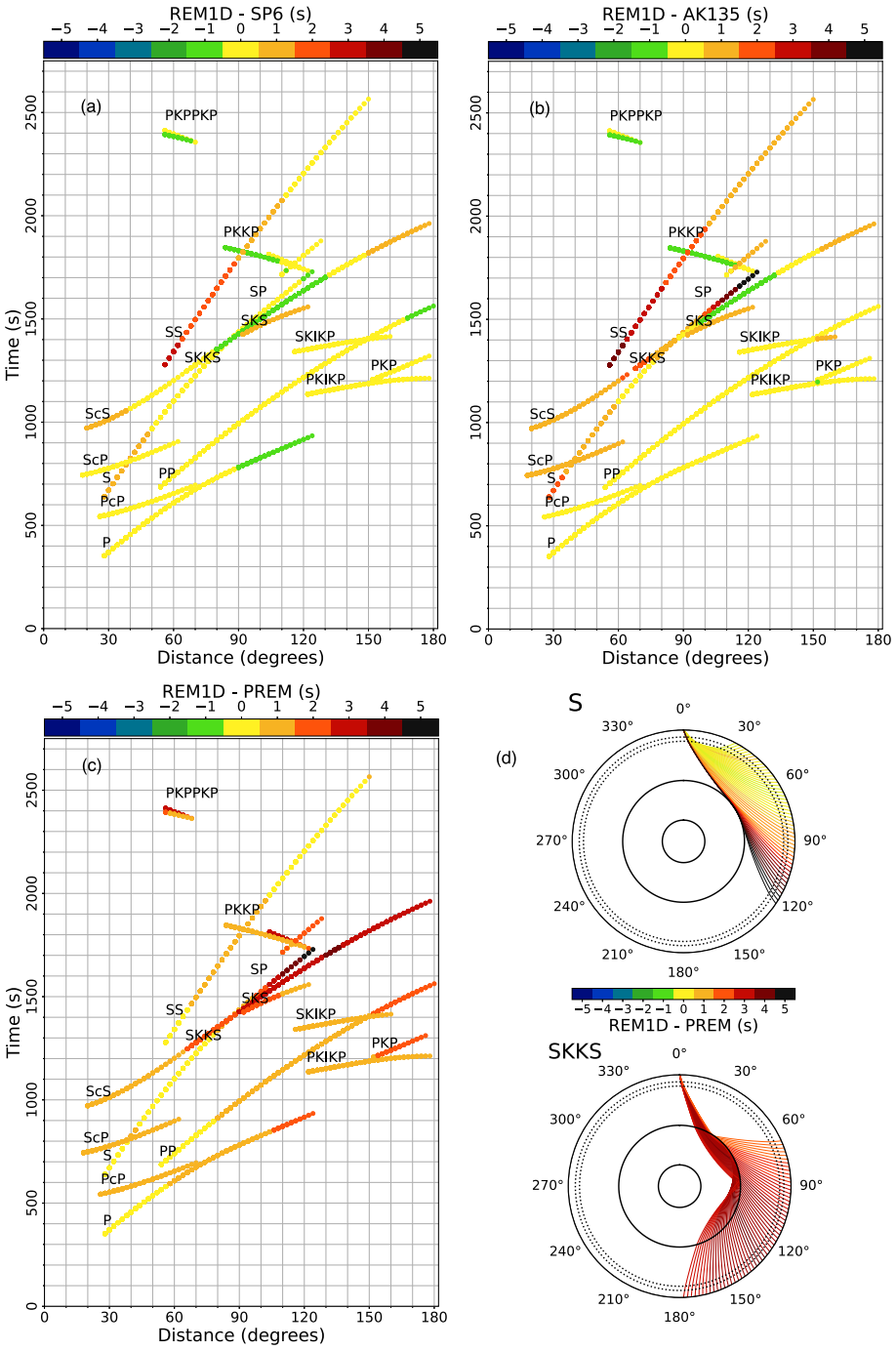

Fig. 9. Record sections containing arrival-time comparison curves between pairs of models. Arrival times of various body-wave phases are calculated at every 2° distance for anisotropic (i.e. REM1D, PREM) and isotropic models (i.e. SP6, AK135). Red colors denote slower velocities (greater arrival times) and blue colors denote faster velocities (smaller arrival times) in the first model compared to the second model in each colorbar. Source is a surface-focus earthquake located at the equator (0°, 0°) and no ellipticity correction is applied. Ray tracing is done in an anisotropic medium (Woodhouse, 1981), assuming that the phases S, SS and ScS are recorded on transverse and others are on the vertical component (cf. Table 2 in Paper I). Note that the major discrepancies (> 1 s) between REM1D and body-wave models (SP6, AK135) are only for phases (S, SS, ScS, SKKS) with sensitivity to the uppermost mantle where there is substantial radial anisotropy and the D″ region where a low-velocity zone is needed to account for the geographic bias in arrival times. Comparisons with other body-wave models are provided as Supplementary Figs. S3–S5.

for different radial parameterizations, where bulk attenuation (Q_κ) is allowed to vary in various combinations of principal regions. The χ^2/N misfits change by ~2–22 times across model scenarios with the addition of one or two extra parameters of bulk attenuation, which is significant above the 99 % level. For any region except the inner core, the inclusion of a single value of Q_κ leads to significant improvements in fits to the reference dataset. Our preferred scenario (REM1D) places finite bulk attenuation in the mantle with two parameters above ($Q_\kappa = 385.62$) and below the 410-km discontinuity ($Q_\kappa = 28{,}596$). REM1D fits quality factors of radial and other modes comparably to the model QL6 (Durek and Ekström, 1996), while affording substantially (6–100 times) better fits to mode eigenfrequencies. All inversions start with no bulk attenuation ($q_\kappa = 0$, $Q_\kappa = \infty$) and utilize only normal mode measurements in this experiment. Due to physical dispersion, both mode eigenfrequencies

Table 5
Retrieved radial models of bulk attenuation Q_κ. The five sets of inversions start with no bulk attenuation (q_κ=0, Q_κ=∞), utilize only normal mode measurements, and adopt a fixed elastic and shear attenuation structure from the preferred model REM1D. Only bulk attenuation parameters are allowed to vary and up to five iterations are performed while damping the norm of perturbations and the step changes between some regions (e.g. transition zone and lower mantle). The χ^2/N misfits to the reference dataset of eigenfrequencies (ω) and quality factors (Q) are provided separately for radial, spheroidal fundamental, v_P-sensitive and all normal modes. Non-linear crustal contributions are included in the predictions for the fundamental modes (Paper I). All depth ranges for the principal regions are provided in km, and a value of Q_κ = 88,888 in our calculations represents ∞ within numerical precision. Note that the substantial changes in fits to eigenfrequencies ω in the first five scenarios are purely due to the physical dispersion caused by bulk dissipation. Last row contains the values from our preferred joint radial reference model REM1D (*in italics*); reduced ω fits compared to the preceding normal-mode only scenarios are due to tradeoffs with body-wave datasets (Section 2.4).

Upper mantle	Transition zone	Lower mantle	Outer core	Inner core	# of Q_κ	χ^2/N Radial	χ^2/N Spher. Fund.	χ^2/N v_P sens.	χ^2/N Core	χ^2/N All
24.4–410	410–650	650–2891	2891–5156	5156–6371	variables	Q | ω	Q | ω	Q | ω	Q | ω	Q | ω
∞	∞	∞	∞	890	1	18 | 142	7 | 88	148 | 81	36 | 102	40 | 34
∞	∞	∞	4017	∞	1	15 | 157	7 | 88	134 | 72	22 | 105	34 | 33
∞	∞	22,533	∞	∞	1	9 | 250	6 | 88	137 | 74	42 | 123	38 | 37
29,360	29,360	∞	∞	∞	1	18 | 256	6 | 87	146 | 79	43 | 126	41 | 38
385	25,893	25,893	∞	∞	2	10 | 143	1 | 5	25 | 24	17 | 109	12 | 20
385.62	*28,596*	*28,596*	∞	∞	*2*	*15 | 377*	*2 | 8*	*25 | 49*	*13 | 141*	*11 | 32*

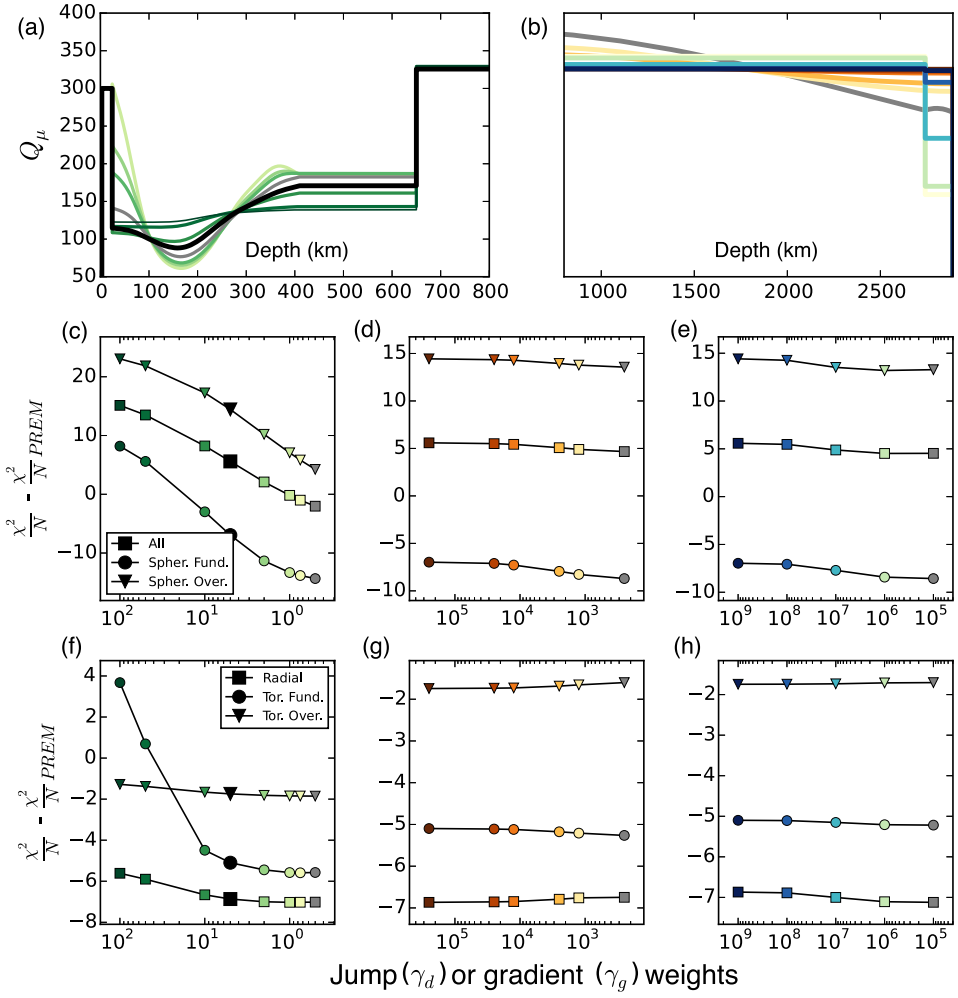

Fig. 10. Tests for resolution of shear attenuation (Q_μ) in different regions of the mantle. Three columns represent sets of inversions that vary the gradients in the upper mantle, gradients in the lower mantle, and the step change at the D″ discontinuity. Radial variations are modulated by applying various amounts of smoothness weights γ_g and discontinuity weights γ_d (Section 2.3). Models inverted in the first set of inversions are plotted in (a) while the other two sets are plotted in (b). The χ^2/N misfits to all quality factor data and its various subsets are plotted separately for the three experiments (c–e). Darker colors correspond to stronger damping i.e. higher weights γ_g and γ_d. Black curves and misfit values are for the preferred damping parameters used in the first iteration of our inversion scheme. Note the reversed order of damping values (x-axes) employed in the misfit plots (c–h) to make the curves correspond roughly to an L-curve analysis for optimal damping parameters (e.g. Marquardt, 1963; Menke, 1989).

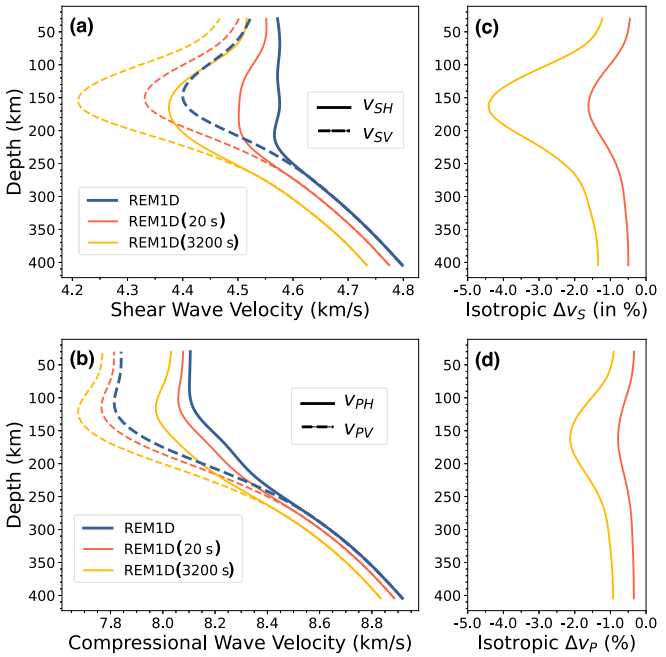

Fig. 11. Effects of physical dispersion on elastic properties 'seen' by various periods of vibration. (a-b) Dispersed elastic parameters of the radially anisotropic medium are calculated using eq. 8 at the dominant periods (T) of 20 s and 3200 s, which correspond roughly to a typical traveling (body and surface) wave and the longest-period spheroidal fundamental mode ($_0S_2$), respectively. (c-d) Reduction in the 'equivalent' isotropic velocities (eq. 4) is the most dramatic (~4.5 % v_S, ~2 % v_P) at a depth of ~150–175 km where there is a peak of shear attenuation (Q_μ = 60–80) in REM1D (Figs. 1 and 14b). Note that the low-velocity zone corresponding to the weak asthenosphere becomes progressively more prominent at longer periods and the effect of physical dispersion is stronger for shear than compressional waves (eq. 8). The elastic parameters of REM1D (i.e. blue curves in a-b) are reported at the reference period of 1 s (Table 1, Supplementary Table S7).

and quality factors are sensitive to bulk dissipation and are used jointly to constrain Q_κ (cf. eq. 16 and Section 4.4 in Paper I) leading to better overall data fits. Inclusion of eigenfrequencies accounting for physical dispersion also reveals a clearer preference for a finite bulk attenuation restricted to the mantle. Radial and core-sensitive (PKIKP-equivalent) normal modes (Supplementary Fig. S1), which afford constraints on bulk attenuation, are fit significantly better by REM1D with two Q_κ parameters in the mantle. While PKIKP-equivalent modes afford strong compressional energy densities in the core, they also have comparable or even higher (~0.8–2 times) shear- and compressional-energy densities in the mantle (e.g. Dahlen and Tromp, 1998). Placing finite Q_κ in the mantle not only leads to 1.2–2.5 times lower χ^2/N misfits for core-sensitive modes but also affords up to 6 times lower misfits for modes primarily sensitive to v_P structure in the mantle (e.g. Deuss et al., 2013). Examination of each subset of data in Table 5 verifies that the details of bulk dissipation in REM1D are not dictated by a single type but are rather consistent with the entire reference dataset.

Shear attenuation in the mantle lithosphere (24.4–80 km) and the transition zone (410–650 km) are not as well constrained as at the depths corresponding to the asthenosphere (80–250 km). Although not shown here, a few of our model scenarios exhibit slightly higher shear attenuation (lower Q_μ) in the transition zone compared to the bottom of upper mantle (ΔQ_μ = 10–50), in broad agreement with an undamped inversion performed by an earlier study (cf. Fig. 6 in Durek and Ekström, 1996). However, details of this complexity depend strongly on our choices of regularization in the upper mantle, especially between the depths of ~250–410 km. In order to fit the strong attenuation (low Q_μ) at asthenospheric depths favored by most of the normal modes, cubic splines and the polynomial terms in the upper mantle tend to overshoot the values of Q_μ in the transition zone, resulting in a discontinuity at 410 km depth. Since we do not obtain substantial improvements in data fits with such complexities ($\Delta\chi^2$/N < 10 %), we suppress the step change in Q_μ variations between the upper mantle and the transition zone across the 410-km discontinuity (γ_d). In contrast, very strong damping (γ_d) is needed to eliminate the step change in shear attenuation at the 650-km discontinuity (ΔQ_μ = 156) and this feature is therefore retained. Our results are in agreement with Durek and Ekström (1996), who did not favor low attenuation in the transition zone based on fits to an earlier compilation of quality factor observations. Similar experiments with shear attenuation in the mantle lithosphere show minor improvements in fits when strong gradients are permitted in this region; we adjust the gradient damping $\left(\gamma_g\right)$ for a smooth transition to a crustal Q_μ of 300 (Durek and Ekström, 1996).

3.2. Mantle velocities and density

Joint inversions of surface-wave, normal-mode and body-wave datasets allow us to constrain the isotropic v_P and v_S variations throughout the Earth's mantle. New reference datasets of Love- and Rayleigh-wave dispersion (Paper I), in particular, provide some of the best constraints on shear-wave velocities in the uppermost mantle. We obtain similar variations (deviation < 1 %) of isotropic v_S at 80–410 km depth using a variety of smoothness and norm regularization schemes. Structure in the shallowest mantle cannot be accurately modeled using the body-wave phases in isolation (e.g. AK135, EK137). While inversions using arrival-time curves favor an overall reduction of shear velocities in the upper mantle from faster starting models (Paper I), it is the average phase velocities (or corresponding eigenfrequencies) of fundamental-mode surface waves that require a low-velocity zone in the upper mantle (~150–175 km). Joint modeling of different data types is even more important for constraining structure in the deeper regions of the mantle. While some sensitivity to v_S variations in the transition zone is afforded by the teleseismic S and SS phases, strong norm damping is required to stabilize our inversions when the normal mode eigenfrequencies are excluded.

Our estimates of isotropic velocities in the mantle show substantial deviations from PREM (Fig. 2). We find clear signatures of two low-velocity zones in the upper and lower boundary layers of the mantle based on multiple datasets. This feature can be easily identified based on the depth gradients of density and isotropic velocities (i.e. $\dot{v}_S = dv_S/dz$, $\dot{\rho} = d\rho/dz$), which should be positive in an adiabatic, homogeneous mantle undergoing hydrostatic compression. In the uppermost mantle, REM1D has 4 times stronger negative v_S gradients ($\dot{v}_S = -0.0015/s$) than PREM between Moho and 150 km depth but the v_P gradient is negligible ($\left|\dot{v}_P\right| \ll \left|\dot{v}_S\right|$). The upper mantle is therefore characterized by a pronounced low-v_S zone and a weaker low-v_P zone. In contrast, PREM reported 2 times stronger v_P gradients than v_S gradients in the upper mantle, a discrepancy that is likely caused by the past limitations in short-period measurements (Paper I). The low-velocity zone in both v_P and v_S structure becomes more prominent at progressively longer periods of vibration (e.g. 20 and 3200 s) due to the effects of physical dispersion in REM1D (Fig. 11). In the D″ region, negative gradients are noted for both v_P and v_S variations ($\dot{v}_S = 2{\cdot}\dot{v}_P = -0.0004/s$), but their magnitudes are smaller than in the upper mantle boundary layer. In contrast, PREM contains a weak negative $\dot{v}_S$ with a positive $\dot{v}_P$ and $\dot{\rho}$ in the D″ region. REM1D prefers low-velocity zones and lower values of v_P and v_S in this region in order to fit arrival-time curves of diffracted P_{diff} and S_{diff} waves ($\Delta > 90°$). After accounting for the preferential sampling of the faster heterogeneity in the northern hemisphere, steep negative velocity gradients are required in the lowermost mantle by body waves that bottom near the CMB (e.g. Morelli and Dziewonski, 1993). Interpretations of these low-velocity zones are discussed further in Section

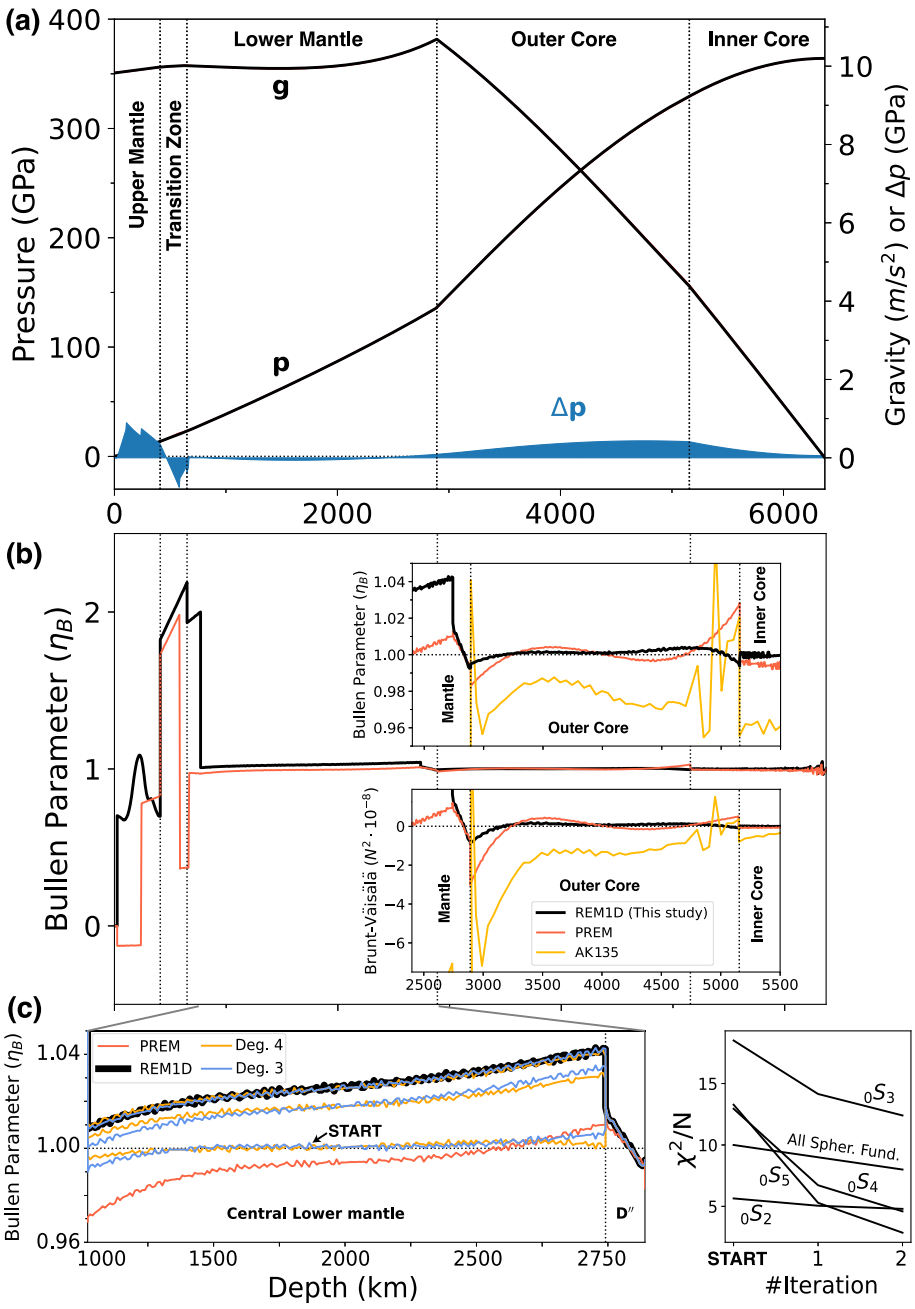

Fig. 12. Relevant physical properties of various radial models. (a) Pressure and gravity are functions of density, while (b) Bullen's stratification parameter (η_B) and squared Brunt-Väisälä frequency (N^2, inset) are functions of both radial gradients and structure. The blue filled curves in (a) report the deviations in pressure between REM1D and PREM, $\Delta p = p$ - p_{PREM}. More detailed comparisons between published models on variations in the outer core are provided in Fig. 7. (c) Robustness of η_B variations in the central lower mantle. Similar values are obtained after 2 iterations (blue or yellow curves) from starting models that satisfy the Adams-Williamson equation ($\eta_B = 1$), irrespective of the polynomial order used for density (3 or 4). Preferred η_B values from REM1D afford improved (up to 4.6 times lower) χ^2/N misfits to the longest-period spheroidal fundamental modes ($_0S_{2-5}$), which are sensitive to density structure in the lower mantle. Note that the η_B values in the central lower mantle exceed 1.03 below a depth of ~2100 km. A well-mixed homogeneous material corresponds to Bullen's parameter $\eta_B \sim 1$ and Brunt-Väisälä frequency $N^2 \sim 0$. Values of the physical properties from REM1D are listed in Supplementary Table S7.

4.5.

Substantial revisions to density variations in PREM are required throughout the mantle. In the shallowest 200 km, it has been suggested that discrepancies between observations of Earth's flattening and hydrostatic predictions can be attributed to the anomalous and gravitationally unstable low-density zone in the PREM upper mantle (Nakiboglu, 1982). In REM1D, density gradients in both upper and lower mantle boundary layers are positive ($\dot{\rho} > 0$) and no subset of data requires a dramatic reduction of density in both regions. An increase in density (up to 0.3 %) relative to PREM with steeper gradients ($\dot{\rho}$) is found in the REM1D lower mantle. Pressure distribution obtained from REM1D is consistent with PREM to within ~1 GPa in all principal regions; minor deviations are observed in the uppermost mantle and the transition zone with the peak value ($\Delta p = p$ - p_{PREM} = 0.89 GPa) at 108 km depth (Fig. 12a). While the pressure scale is important for calibrating EoS parameters and inferring bulk chemical composition in a self-consistent manner (e.g. Stixrude and Lithgow-Bertelloni, 2011), choice of the radial reference model will contribute significantly lower

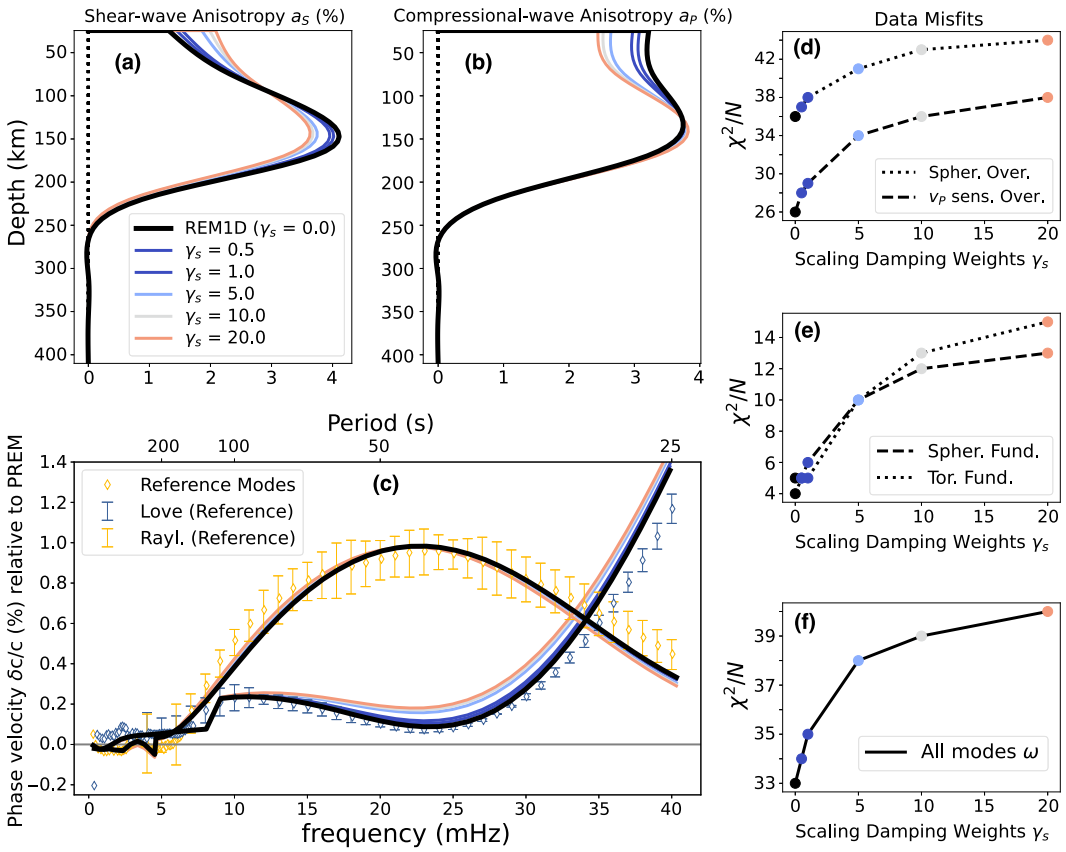

Fig. 13. Tests for the magnitude of radial anisotropy in the shallowest mantle. (a,b) Variation of anisotropy for different scenarios of damping that impose scaling and correlation between v_P and v_S anisotropy ($a_S = 0.55 \cdot a_P$) in the mantle lithosphere (24.4–80 km). (c) Predicted dispersion curves from the inverted scenarios accounting for the non-linear contributions from CRUST2.0 compared with the bulk reference dataset from Paper 1. (d–f) Fits to various subsets of mode eigenfrequencies (i.e. spheroidal, toroidal fundamental modes and overtones) as a function of the amount of scaling damping. Black curves and misfit values correspond to the preferred set of damping parameters ($\gamma_s = 0$) used in REM1D inversions. Note the strong sensitivity (cf. Supplementary Fig. S2 in Paper I) of fundamental-mode surface wave dispersion to slight changes in anisotropy in the uppermost mantle (c,e). Moderate anisotropy in the mantle lithosphere and peak anisotropy at ~125–150 km depth is detected irrespective of the damping choices.

uncertainties ($\Delta p < 0.15$ %) to the analysis below the transition zone ($p > 25$ GPa) than uncertainties stemming from mineral physics (e.g. $\Delta p = 15$ % at 330 GPa based on EoS for platinum; Stacey and Davis, 2004).

Table 4 reports the step changes in elastic parameters and density across major internal discontinuities. REM1D estimates fall inside the 95 % confidence interval (2-σ) of the normal distributions and are within the bounds of uniform distributions in the reference dataset. Classical radial models (e.g. SP6, AK135, PREM) fit the new dataset of contrasts in physical properties comparably well at the 410-km discontinuity. However, REM1D reports up to 2 times weaker contrasts in velocity and impedance (Z_P, Z_S) than PREM across the 650-km discontinuity. Our estimates of Z_P and Z_S across this discontinuity are consistent with AK135, which is used in a few body-wave studies due to its ability to fit amplitudes of the SS phase that is a function of impedances. However, the v_S contrast that underlies the Z_S impedance is substantially lower in REM1D for both discontinuities in the transition zone; there is even a tendency for this step change to reduce further (i.e. with lower γ_d) albeit with insignificant improvements to the χ^2/N misfits. Our v_P contrast of 2.5 % across the 650-km discontinuity agrees with the values obtained from the analysis of SS- and PP-precursors (Shearer and Flanagan, 1999; Estabrook and Kind, 1996), receiver functions (Lawrence and Shearer, 2006) and ScS reverberations (e.g. Revenaugh and Jordan, 1991, cf. Table 3 in Paper I) at the 95 % confidence interval. Topography of the transition-zone discontinuities may be expected due to lateral variations in temperature and composition, which would reduce the apparent contrast if pervasive in lateral extent. However, strong large-scale variations (exceeding ±5 km) are found only in geographically localized regions such as subduction zones while large swaths of the mantle retain the discontinuity close to 410 and 650 kms (S362ANI+M; Moulik and Ekström, 2014). After accounting for the tradeoffs between velocity and the topography of internal discontinuities using full-spectrum tomography, the spherically-averaged depths of both discontinuities do not deviate by more than 0.17 km in S362ANI+M. Contrasts in the bulk structure of REM1D are therefore unlikely to be influenced by the large-scale topography of internal discontinuities. Implications of these contrasts for bulk composition of the mantle are discussed in Section 4.7.

3.3. *Extent of radial anisotropy*

Strong radial anisotropy with fast horizontally polarized shear-wave velocities ($v_{SH} > v_{SV}$, $\xi > 1$) is required in the upper mantle (24.4–410 km) to fit surface-wave dispersion curves and eigenfrequencies of short-period normal modes. REM1D exhibits the maximum shear-wave anisotropy at ~125–150 km depth ($a_S = 3.90$ %, $\xi = 1.08$) with smoothly decreasing values at shallower and deeper parts of the uppermost mantle. These features are in contrast to PREM, which reported a monotonically decreasing a_S anisotropy with depth in the upper 220 km of the mantle. We suppress radial anisotropy below 250 km with norm damping since such variations fail to significantly improve the fits to any subset of reference datasets above the 95 % confidence level. Our anisotropic variations are comparable in magnitude but differ in pattern when compared to the radial model STW105 that was optimized to fit surface-wave dispersion. Peak shear-wave anisotropy in REM1D is somewhat deeper than in STW105 and anisotropy in the mantle

lithosphere (24.4–80 km) does not diminish to zero close to the Moho. We correct the Rayleigh wave dispersion data for azimuthal anisotropy and account for non-linear effects of the crust on wave propagation (Paper I), modeling choices that improve the constraints on radial anisotropy in the shallowest regions of the Earth.

Non-linear contributions from the strong crustal variations (Paper I) strongly influence both shear- and compressional-wave anisotropy (a_S, a_P) in the mantle lithosphere. After accounting for this effect, mode eigenfrequencies (and corresponding surface-wave dispersion) require higher v_{SV} and lower v_{SH} velocities than PREM in the shallowest mantle. REM1D therefore exhibits a more prominent peak in a_S anisotropy and a more distinct low-velocity zone than earlier radial models. In our preferred inversions, both a_S and a_P anisotropy are allowed to vary independently with no correlation or scaling with each other. REM1D contains roughly 3 times stronger compressional-wave anisotropy (a_P = 3.31–3.39 %, ϕ = 0.93–0.94) than shear-wave anisotropy (a_S = 1.09–2.00 %, ξ = 1.02–1.04) in the mantle lithosphere. In order to evaluate the robustness of this feature, we experimented with amounts of damping (γ_s) that impose scaling and correlation ($a_S = 0.55 \cdot a_P$) in the mantle lithosphere as expected from petrological constraints (e.g. Montagner and Anderson, 1989a). Fig. 13 contains the model scenarios and their predictions to dispersion curves and other normal-mode reference datasets. Imposing constant a_P-a_S scaling in the mantle lithosphere leads to deterioration in fits to all subsets of the reference dataset, particularly to the dispersion of fundamental-mode surface waves. The χ^2/N misfits to these dispersion data reduce by a factor greater than 2 when strong damping is applied ($\gamma_s \geq 5$, Fig. 13c,e), which is significant at the 95 % confidence level. Placing strong emphasis on anisotropic scaling in the mantle lithosphere has the adverse effect of reducing the magnitude of peak a_S anisotropy (Fig. 13a). It is evident that reference datasets corrected for nonlinear crustal effects are sensitive to small changes in radial anisotropy, and that the peaks in both a_P and a_S anisotropy at ~125–150 km depth do not depend strongly on regularization choices.

The surface-wave dataset employed in this study provides the strongest sensitivity to shear-wave anisotropy in the upper mantle (cf. Supplementary Fig. S2 in Paper I). Resolution of the remaining anisotropic parameters - compressional-wave anisotropy and η - is slightly more limited based on the sensitivity afforded by currently available datasets. Nevertheless, modeling choices regarding these two parameters can influence the variations of shear-wave anisotropy in our inversions. For example, compressional-wave anisotropy (i.e. a_P, ϕ) trades off with density and shear-wave anisotropy (a_S) in the shallowest mantle (e.g. Beghein et al., 2006; Kustowski et al., 2008). We apply gradient and norm damping to obtain smooth variations in compressional-wave anisotropy ($a_P \leq 3.78$ %, ϕ = [0.93,1]) in the shallowest 250 km of the mantle (cf. Appendix A in Paper I). In case of the fifth anisotropic parameter η, we start with a constant isotropic value of 1 throughout the Earth and examine possible deviations in the upper mantle. We choose to suppress perturbations in η below 250 km using strong norm damping; relaxing this constraint does not appreciably improve the overall fits to the normal-mode eigenfrequencies. While the details of η variations depend on the smoothness applied in different depth regions, values below 1 are preferred by both spheroidal mode eigenfrequencies and Rayleigh-wave dispersion. Several iterations are required before the models converge towards the η variations in our preferred model (Figs. 1b and 2c), which contains a smooth change from 1 at a depth of ~300 km to 0.92 at the Moho. The magnitude of compressional-wave anisotropy is similar to earlier models (e.g. PREM, STW105) and is largely independent of the η structure in the shallowest 200 km of the mantle.

Although not shown here, we have performed experiments that modulate the anisotropic features of other principal regions using various regularization schemes. When additional anisotropic parameters in the deep mantle are included as free parameters in our inversions, mild anisotropy ($a_S < 1$ %, $v_{SH} > v_{SV}$, $\xi > 1$) is observed in the transition zone. When we solve for radial anisotropy throughout the lower mantle, the D″ region exhibits a slightly reduced anisotropy ($v_{SV} > v_{SH}$, $\xi < 1$) largely due to tradeoffs with anisotropic variations in the mid mantle. Reference eigenfrequencies of core-sensitive modes are adequately fit without requiring the presence of shear- or compressional-wave anisotropy (a_S, a_P) in the inner core. In contrast to some studies (e.g. Montagner and Anderson, 1989b; Beghein et al., 2006; Panning and Romanowicz, 2004; Visser et al., 2008), we do not obtain substantial improvements in misfits ($\Delta\chi^2$/N < 5%) to any subset of normal modes by allowing pervasive anisotropic features below a depth of 250 km. Other studies have reported a strong tradeoff between isotropic and radially anisotropic variations in the lowermost mantle (e.g. Kustowski et al., 2008). Additional constraints from normal modes help alleviate some of the tradeoffs in structure, as was demonstrated in case of lateral variations in the lowermost mantle (Moulik and Ekström, 2014). Even with our methodological improvements (Paper I), current reference datasets require neither predominant horizontal flow in the lowermost mantle (Panning and Romanowicz, 2004) nor anisotropy arising from texturing or solidification of the inner core (Lythgoe and Deuss, 2015).

3.4. Core structure

Elastic and density structure of the Earth's core does not deviate substantially from the starting model that followed the Adams-Williamson equation (e.g. $\eta_B = 1$) and expectations of derivative properties (e.g. κ') from mineral physics (Paper I). REM1D can fit reference datasets without the very steep gradients of v_P and v_S in the outer and inner core reported by SP6, which lead to anomalously large κ' values with positive curvatures (κ''). Such features may not be expected in an iron-rich crystalline inner core or a well-mixed outer core with uniform phase and composition (e.g. Stacey, 2005) so need to be invoked only when other options have been exhausted. While some body-wave studies report a dramatic change of velocity gradients in the lowermost outer core atop the inner-core boundary (e.g. Kennett et al., 1995; Song and Helmberger, 1995), we demonstrate that a radial model can be constructed without the need for this feature (Fig. 7) while affording similar fits to body-wave arrival times (Table 3) and significantly better fits to normal-mode measurements (Table 2). This is possible due to the limited sensitivity of the SKS, SKKS and PKP_{ab} phases to this region since their turning depths for the available range of epicentral distances (cf. Table 2 in Paper I) are shallower than the bottom 500 km of the outer core (Supplementary Figs. S3–S5). Other core phases like PKIKP and P′P′ do not isolate sensitivity to this region while the few PKP_{bc} arrivals that turn at these depths are fit very well ($\psi_{pb} = 0.25$ s, Table 3) by REM1D. Improvements in fits to the core phases also require REM1D to have steeper v_P gradients than PREM with up to 0.5 % lower velocities in the outermost outer core (Fig. 2g). Steeper v_P gradients in the outermost 90–450 km of the core are consistent with array studies of SmKS body wave phases (Section 2.4), which are highly sensitive to this region (e.g. Tanaka, 2007; Helffrich and Kaneshima, 2010; Kaneshima, 2018). Eigenfrequencies of spheroidal overtones sensitive to the core and v_P structure are also fit significantly better by REM1D with χ^2/N misfits that are reduced 2–4 times compared to PREM (Table 2).

Although inner core is a principal region that occupies less than 1 % of the Earth by volume, a few precise seismic observations are available to probe its structural properties. Due to the spread in structural sensitivity (Supplementary Fig. S1), core-sensitive normal modes may find it difficult to discriminate a higher $\Delta\rho$ localized at the inner-core boundary (ICB) from the integrated effects of a density gradient above the ICB followed by a smaller $\Delta\rho$ (e.g. Gubbins et al., 2008). We utilize normal-mode and body-wave datasets that constrain both absolute properties and their gradients on either side of the ICB. Density contrast ($\Delta\rho$) at the ICB is 0.6 g/cm^3, which is broadly consistent ($\pm 2\sigma$) with recent normal-mode (e.g. Masters and Gubbins, 2003) and body-wave studies (e.g.

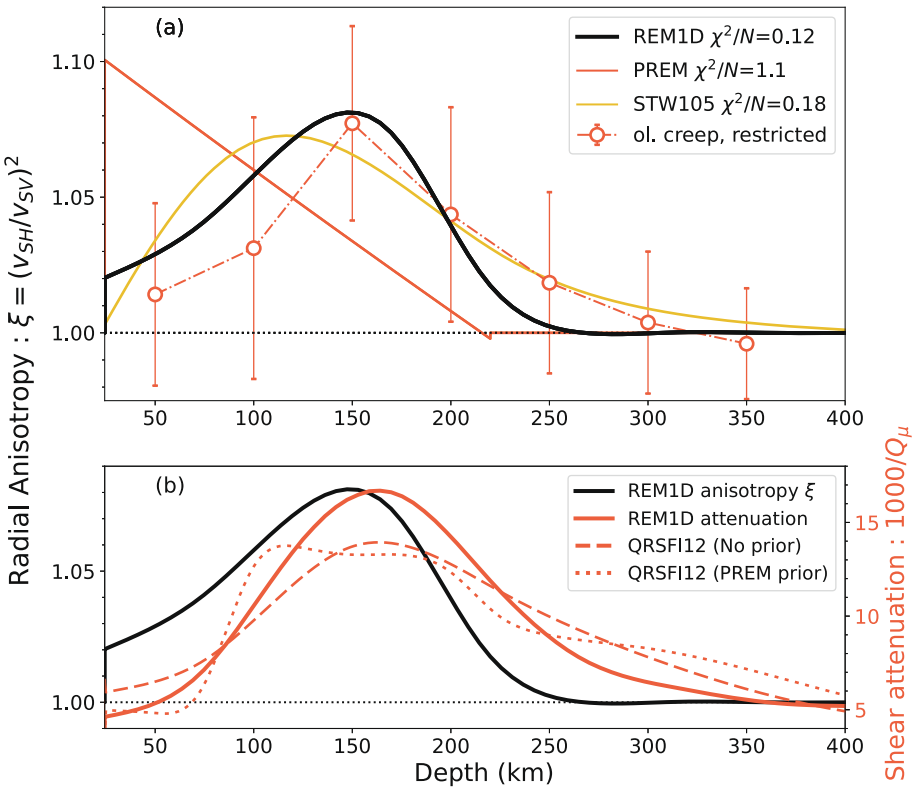

Fig. 14. Comparisons of REM1D with geodynamic flow and 3D attenuation models. (a) Depth variation of shear-wave anisotropy (ξ, eq. 3) in REM1D is compared with the values from PREM and STW105. Predictions of ξ from a dynamic flow study where texture formation is restricted to regions where olivine is in dislocation creep are provided as red circles (Becker et al., 2008). The χ^2/N misfits between seismological radial models and geodynamic predictions are provided in the legend. (b) Shear attenuation, in terms of $1000/Q_\mu$, is plotted with a twin axis and red curves. Values from REM1D are compared against the average attenuation of the 3D shear attenuation model QRSFI12 (Dalton et al., 2008), derived using a smooth PREM as the starting model or otherwise. When no prior information is imposed, both REM1D and QRSFI12 agree that the peak attenuation (Q_μ = 60–80) is present at a depth of ~150–175 km. Peak anisotropy is found 17 ± 5 km shallower in depth than the mechanically weak (low v_S and Q_μ) asthenosphere.

Koper and Dombrovskaya, 2005). Early seismological estimates of $\Delta\rho$ at the ICB derived from the amplitude ratios of PKiKP/PcP phases (Bolt and Qamar, 1970) were up to 2 times higher and had limited global coverage. Recent body-wave studies (cf. Table 3 in Paper I) have placed upper bounds of $\Delta\rho < 1$–1.2 g/cm^3 (Shearer and Masters, 1990; Tkalčić et al., 2009; Waszek and Deuss, 2015), which is consistent with our estimates. Major features of the inner core do not change substantially with the addition of a cubic polynomial for density that suppresses the η_B artifacts from parameterization (Section 2.2, Paper I). REM1D finds κ' values in the inner core that are marginally higher (2.35–2.36) than PREM (2.33–2.34), features related to the 0.1–0.5 % reduction in velocities (Figs. 2g and 16). Thermodynamical interpretations based on the revised core structure are discussed in Section 4.9.

4. Thermo-chemical and dynamical interpretations

REM1D represents revised estimates of average physical properties with important implications for the bulk thermo-chemical state and global dynamics of the Earth's deep interior. In the sections below, we discuss some outstanding geological questions where new information is gleaned by this study.

4.1. Origins of radial anisotropy

Boundary layers that contain intrinsically anisotropic minerals and undergo strong deformation are prime candidates for pervasive seismic detections of radial anisotropy that is LPO-style in origin. For example, the *a*-axis of dry olivine aligns parallel to flow direction, resulting in $v_{SH} > v_{SV}$ for regions with horizontal flow and $v_{SV} > v_{SH}$ for regions with vertical flow (e.g. Nicolas and Christensen, 1987; Mainprice et al., 2000). Shear-wave anisotropy in the shallowest mantle of REM1D ($v_{SH} > v_{SV}$, $a_S > 0$, $\xi > 1$) are likely LPO-style textures of intrinsically anisotropic grains arising from the horizontal flow in this ductile region under dislocation creep (e.g. Nicolas and Christensen, 1987; Montagner, 2002; Becker et al., 2008). REM1D also detects compressional-wave anisotropy ($v_{PH} > v_{PV}$, $a_P > 0$, $\phi < 1$) and η values in the range of 0.92–1 within this region (Section 3.3, Figs. 1 and 2). In contrast to earlier radial models like PREM, values of an alternative fifth elastic parameter η_κ in REM1D exceed one (1–1.01) throughout the mantle lithosphere and asthenosphere (Supplementary Fig. S6), a feature that cannot be attributed to a layering of homogeneous isotropic layers and requires intrinsic anisotropy as the dominant mechanism (Backus, 1962; Berryman, 1979). Our η_κ variations are found to be consistent with radial anisotropy in this region even though we neither parameterize in terms of η_κ nor damp its values towards one. A gradual increase of anisotropy with depth in the shallowest mantle is consistent with the effect of temperature on single-crystal estimates of anisotropy in upper mantle minerals such as olivine and enstatite (Mainprice, 2007). Peak shear-wave anisotropy ($a_S = 3.90$ %, $\xi = 1.08$) and compressional-wave anisotropy ($a_P = 3.78$ %, $\phi = 0.93$) both lie at a depth of ~125–150 km (Fig. 1c). REM1D estimates of peak anisotropy may indicate pervasive large-scale processes such as apparent plate motion or density-driven flow in the oceanic mantle (e.g. Conrad and Behn, 2010; Becker et al., 2014).

Calibration against bulk seismological properties can help glean information on first-order effects that are less sensitive to the starting conditions in geodynamic simulations. Fig. 14 provides comparison of our estimates of average radial anisotropy with those derived from a

geodynamic flow study that modeled shear deformation (Becker et al., 2008). A low viscosity asthenosphere underneath oceanic plates, which cover a majority of the Earth's solid surface, promotes efficient shear alignment of LPO and formation of radial anisotropy. REM1D recovers an abrupt dropoff in radial anisotropy below ~250 km, which is consistent with geodynamic simulations ($\chi^2/N = 0.18$) when a olivine creep law is used with LPO formation limited to regions dominated by dislocation creep (Fig. 14a). This mechanism may be favored compared to two alternatives investigated by Becker et al. (2008) - LPO formation due to recent asthenospheric flow from only radial viscosity variations ($\chi^2/N = 3.38$) or lateral viscosity variations with a joint dislocation and diffusion creep law for olivine ($\chi^2/N = 0.27$). Peak anisotropy in REM1D is slightly deeper (~125–150 km) than in STW105 that did not account for azimuthal anisotropy, and is more consistent with all geodynamic flow scenarios (Fig. 14a).

Seismological and geodynamic estimates of average anisotropy differ substantially within the mantle lithosphere (24.4–80 km). REM1D detects mild shear-wave anisotropy in this region ($a_S = 1.09$–2.00 %, $\xi = 1.02$–1.04), which is a robust feature based on our experiments (Section 3.3). This estimate is lower than PREM (3–5 %) and substantially higher than the negligible anisotropy in recent models like STW105 (Fig. 14a). Moreover, compressional-wave anisotropy is high ($a_P = 3.31$–3.39 %, $\phi = 0.93$–0.94) in the mantle lithosphere and does not scale uniformly with shear-wave anisotropy (Fig. 13). REM1D values are broadly consistent with path-average studies that report non-negligible amounts of shear-wave anisotropy ($a_S = 2$–6 %) in the mantle lithosphere across diverse tectonic settings (e.g. Nishimura and Forsyth, 1989; Gaherty et al., 1999a; Simons and van der Hilst, 2003; Gaherty, 2004). Geodynamic flow models consistently predict lower mean anisotropy in the mantle lithosphere than our estimates ($\xi = 1.02$–1.04, Fig. 14a). Due to the small strain rates in the mantle lithosphere and other modeling assumptions (e.g. LPO formation duration), simulations with the radial viscosity scenario are almost isotropic ($\xi \sim 1$) at depths shallower than ~125 km. The residual anisotropy in the mantle lithosphere may be attributed to frozen-in LPO in oceanic or continental lithosphere (e.g. Gaherty and Jordan, 1995; Simons and van der Hilst, 2003), or other mechanisms (e.g. melt alignment, shape-preferred orientation SPO) that are unaccounted for in most geodynamic simulations (e.g. Becker et al., 2008). Our results disfavor a preponderance of stronger anisotropy in the mantle lithosphere than the asthenosphere, a feature in some regional studies that attribute it to seafloor spreading (e.g. Debayle and Ricard, 2013; Lin et al., 2016).

Overall, REM1D improves estimates of average radial anisotropy (Figs. 1 and 2) in the upper mantle by accounting for the azimuthal dependence in surface-wave phase velocities and the non-linear effects of the crust on wave propagation (Paper I). Majority of the reference datasets, especially the phase velocities (or equivalent eigenfrequencies) of fundamental-mode surface waves, can be reconciled with the presence of radial anisotropy restricted to the uppermost ~250 km of the mantle (Section 3.3). Intrinsic anisotropy tends to reduce when certain minerals such as olivine undergo phase transformations in the transition zone (e.g. Mainprice, 2007). For example, ringwoodite is nearly isotropic with a cubic structure (Weidner et al., 1984; Kiefer et al., 1997; Sinogeikin et al., 2003), while majorite garnet and clinopyroxene either have too weak single-crystal anisotropy or lack in mineral fraction abundances (e.g. Sang and Bass, 2014; Pamato et al., 2016). The long-wavelength geoid tends to prefer an increase of viscosity in the lower mantle (e.g. Hager et al., 1985; Rudolph et al., 2020), which could be related to a suppressed vigor of deformation, reduction in grain size and a predominance of diffusion creep that would prevent the formation of LPO-style textures (e.g. Dannberg et al., 2017). REM1D represents the average structure and pervasive mechanisms, so localized features with limited strength and lateral contiguity need to be evaluated using full three-dimensional models. Additional factors that may be important at regional scales include activation of other slip systems in wet olivine under high-stress conditions (e.g. Jung and Karato, 2001; Karato et al., 2008; Ohuchi and Irifune, 2013), influence of melt distribution on olivine LPO (Holtzman et al., 2003; Holtzman and Kendall, 2010), or other potential mechanisms (e.g. Greve and Savage, 2009; Faccenda et al., 2008).

4.2. Mechanisms of attenuation

Our preferred model of bulk and shear attenuation is constructed while accounting for the effects of physical dispersion on seismic observations (Section 3.1). REM1D provides better fits than PREM to the new reference dataset of quality factor observations using a shear attenuation (Q_μ) model that is smooth across the 220-km discontinuity, further validating the exclusion of this discontinuity for all physical parameters. Peak shear attenuation with $Q_\mu \sim 60$–80 is detected at a depth of ~150–175 km corresponding to a mechanically weak asthenosphere. Strong shear attenuation in the upper mantle with a peak at ~160–175 km is also seen in three-dimensional studies of oceanic regions (e.g. Selby and Woodhouse, 2002; Dalton et al., 2008). Previous radial models that did not employ a detailed and smooth Q_μ parameterization in the upper mantle nevertheless report similarly low values ($Q_\mu \sim 80$) at these depths (e.g Durek and Ekström, 1996; Widmer et al., 1991). A strongly attenuating low-velocity zone with a deeper region of higher velocities and reduced attenuation may be interpreted in terms of solid-state mechanisms that depend on variations in temperature and grain size without invoking the presence of partial melt or fluids (e.g. Faul and Jackson, 2005). Such an explanation would also imply that partial melt or fluids are likely localized in regions with very limited extent such as beneath the mid-ocean ridges, subduction zones or back-arc basins (Section 4.3).

We achieve good fits to quality factor observations and other reference datasets with a frequency-independent attenuation model suggesting a broad absorption band for Earth materials at seismic frequencies (Liu et al., 1976; Kanamori and Anderson, 1977). Since the reference period of REM1D elastic structure is 1 s, the dispersion correction is substantial for the long-period normal modes (eq. 8, Fig. 11). Any signal of frequency dependence could manifest as large residual variances of the long-period normal modes or as tradeoffs with short-period body waves. While minor tradeoffs that are natural for joint inversions are noted (Section 2.4), REM1D is able to reconcile all reference datasets without requiring any frequency dependence in shear dissipation ($\alpha_Q = 0$) for seismic waves between ~1–3200 s. Both the quality factors and eigenfrequencies of normal modes are fit significantly better than all radial models published to date (Table 2). Based on current datasets in this period band, there is no apparent need to invoke the frequency dependence of shear attenuation suggested by a few studies (e.g. Anderson and Given, 1982; Lekic et al., 2009). Improved estimates of these data and uncertainty bounds could be useful in disentangling the signal of α_Q from the depth dependence of shear attenuation that is recovered by REM1D. Our results on frequency independence ($\alpha_Q = 0$) suggest that there could be additional dissipation mechanisms active within our modeled period band (~1–3200 s) that act to suppress the mild frequency dependence ($\alpha_Q = 0.2$–0.4) in background dissipation from diffusionally accommodated grain boundary sliding (e.g. Raj, 1975). It is conceivable that only solid-state dissipation mechanisms with additional effects of impurities, larger grain sizes and near melting temperature are sufficient to explain both the depth variation and frequency independence of shear attenuation in the upper mantle (Jackson et al., 2002; Faul and Jackson, 2005; Takei et al., 2014). Although there could be a superposition of multiple absorption peaks with individual relaxation mechanisms at seismic frequencies, there needs to be at least one peak attenuation mechanism that dominates the relaxation spectrum and is substantially more dissipative than the monotonic high-temperature background.

Finite bulk attenuation ($Q_\kappa = 385.62$) in the upper mantle (24.4–410

km depth) provides an optimal fit to both quality factor and eigenfrequency measurements (Sections 3.1); ratio of bulk to shear attenuation in this region is higher ($R_q = Q_\mu/Q_\kappa = 17$–$60$ %) than in the lower mantle (~0.8 %). In contrast to the early studies of radial structure (e.g. Masters and Gilbert, 1983), current reference datasets can place finite bulk attenuation in the upper mantle without adopting strong *a priori* constraints on R_q (< 2 %) or prescribing no attenuation ($Q_\kappa = \infty$) in the outer core. Since the REM1D parameterization in the upper mantle comprises a boxcar for bulk attenuation and cubic B-splines for shear attenuation, detailed variation of these ratios should be interpreted with caution to avoid artifacts from parameterization. However, average ratio for the upper mantle ($R_q = 35$ %) is largely independent of the parameterization choices and data limitations; this estimate is also consistent with earlier studies that used boxcars for the parameterization of Q_κ (Durek and Ekström, 1995). While the mechanism of diffusionally accommodated grain boundary sliding may be sufficient to explain shear attenuation in the upper mantle (e.g. Raj, 1975; Faul and Jackson, 2015), this mechanism cannot be used to explain the finite bulk dissipation at these depths. Solid-state mechanisms could be adequate to explain the R_q ratios in the lower mantle (e.g. Budiansky et al., 1983). However, the increase in ratio within the upper mantle needs to be evaluated for other microscopic dissipation mechanisms and their dependence on the thermodynamical state (e.g. T, p, d, C, melt fraction). Based on the current literature, our estimates of bulk attenuation and R_q are not high enough to suggest the pervasive presence of partial melt and water in any principal region of the Earth.

4.3. Role of the mantle transition zone

Several features of REM1D suggest that the mantle transition zone (410–650 km) plays a unique role in mantle convection. While phase transformations in this region can occur smoothly over a finite range of depths and can depend strongly on bulk composition (e.g. Akaogi et al., 1989), we are unable to fit the new reference datasets without an abrupt step change at the discontinuities. Normal mode overtones and the SS phase are poorly fit if absolute velocity variations change by more than 0.2 % in order to create very steep gradients that would suppress the step changes. Moreover, a step change in shear attenuation across the 650-km discontinuity is required by the reference datasets (Section 3.1). Nature of this internal boundary is of great importance to geodynamics because it can break mantle convection into two layers. The extent to which phase transformations at both 410 and 650 km influence mantle dynamics scales with the phase buoyancy parameter

$$\Pi = \frac{\gamma \Delta\rho}{g\alpha\rho^2 h}, \tag{19}$$

where γ is the Clapeyron slope, g is the acceleration due to gravity, and h is height of the convecting mantle layer (e.g. Christensen and Yuen, 1985). Phase transformations with negative Clapeyron slopes (i.e. endothermic reactions), such as the bridgmanite forming reaction at 650 km, tend to impede radial mass transfer, while those with positive Clapeyron slopes (i.e. exothermic reactions), such as the olivine to wadsleyite transformation at 410 km, tend to encourage it.

The density contrast ($\Delta\rho/\rho$) across the 650-km discontinuity in REM1D is reduced to almost half the value in PREM ($\Delta\rho = 5.3$ %, Table 4). The upper lower mantle region (650–771 km depth) acts as an extended transition zone to accommodate yet another $\Delta\rho = 3.5$ % across a relatively thin region. Reduced and smooth density contrasts in REM1D supports the idea that the mantle transition zone impedes but does not completely prevent flow of mass and heat between the upper and lower mantle (e.g. Christensen and Yuen, 1985; Tackley et al., 1993). Such a 'leaky' transition zone can still impede whole-mantle convection and result in large root-mean-square (RMS) amplitudes of heterogeneity at these depths (e.g. Moulik and Ekström, 2014). Accumulation of seismically fast and presumably cold and heavy masses have been inferred in the transition zone beneath East Asia in both v_P (e.g. Fukao et al., 2001) and v_S tomography (e.g. Ritsema et al., 2011; Moulik and Ekström, 2014). Other subduction zones such as South America exhibit fast anomalies that are imaged down to ~1000 km demonstrating that some slabs are able to penetrate the 650-km discontinuity. For a critical value of Clapeyron slope (e.g. Christensen and Yuen, 1985), this plethora of subduction scenarios is bound to be facilitated by the reduced density contrast across the 650-km discontinuity in REM1D.

Absolute density variations informs our understanding of the role a principal region plays in global dynamics. The density gradient is very high in the transition zone and its properties are modeled using a continuous linear function in REM1D. This principal region is characterized by greater-than-adiabatic compression due to the phase transformations of olivine to its high-pressure polymorphs. The value of Bullen's stratification parameter (η_B) in the REM1D transition zone deviates substantially from one, consistent to first order with the expectations from mineral physics. However, it is unclear whether the series of expected phase transitions is sufficient to explain radial inhomogeneity in this region or whether radial gradients in bulk composition or changes to the temperature gradients may also be required. If anomalous sources of internal heating are absent, heat flux across the transition zone is unlikely to cause large subadiabatic temperature gradients needed to explain the large η_B values. A chemical layering and the related accumulation of cold, heavy masses can also contribute to strong subadiabatic density increases (e.g. Matyska and Yuen, 2002). If the limited ponding of subducted slabs in the transition zone is considered as representative of the 'leaky' mantle convection, it is unlikely that basalt enrichment or other chemical layering in this region will persist globally over geological timescales.

Step changes in shear attenuation across internal discontinuities can be used to infer the physical state of the mantle transition zone. Based on data-fit considerations, a 410-km discontinuity in Q_μ was excluded but a step change was permitted at the bottom of mantle transition zone (Section 3.1). These features are consistent with the mineralogical expectations regarding the dominant dissipation mechanisms in a mantle with pyrolitic composition. Large step changes of shear attenuation in the transition zone can be disfavored since the polymorphic phase transition from olivine to wadsleyite (~410 km) and ringwoodite (~550 km) involve coordination changes of atomic species but not a wholesale reordering of the unit cell structure. Moreover, experimentally determined grain-boundary diffusivities are similar for the olivine polymorphs in the transition zone (e.g. Dohmen and Milke, 2010). Since the experimentally derived models of velocity and attenuation are likely based on the underlying physical mechanism of grain boundary diffusion (e.g. Jackson et al., 2014; Faul and Jackson, 2005), this mechanism is unlikely to contribute to substantial Q_μ variations within the transition zone. The breakdown from ringwoodite to bridgmanite at a depth of 650 km involves unit-cell scale reordering with a reset of post-reaction grain sizes to approximately 1–20 μm (Solomatov and Reese, 2008). An abrupt change in shear attenuation can therefore be expected at a depth of 650 km, as is observed in REM1D ($\Delta Q_\mu = 156$). However, this step change leads to fast velocities and low shear dissipation in the lower mantle and is therefore of the opposite sign than expected due to the process of grain size reduction alone. Smaller grains tend to decrease seismic velocities and increase attenuation in a homogeneous region. In order to explain REM1D features, we therefore need to modify mineralogical parameters across the phase boundary that can dominate or nullify the effect of grain size reduction. Simple anelastic scaling relationships suggest three parameters in the lower mantle chiefly control Q_μ: grain growth rates (faster growth yields larger equilibrium grain sizes), anelastic activation volume (V^*) (controlling the pressure or depth dependence), and relaxation strength (Δ_B) for the magnitude of step change at 650 km. The grain growth parameters and Δ_B might trade off strongly, since both determine the prefactors to an Arrhenius-type Q_μ relationship that is characteristic of diffusion-based physics. Absent new

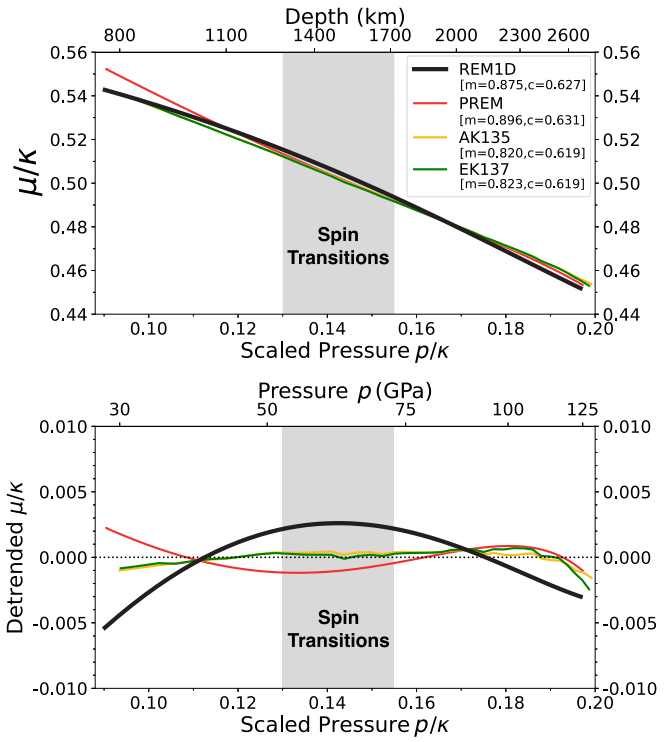

Fig. 15. Comparisons of scaled parameters sensitive to spin transitions in iron-bearing minerals. The shear modulus (μ) and pressure (p) are both scaled by the bulk modulus (κ) calculated using REM1D, PREM and the body-wave models AK135 and EK137. Trends between the two parameters are fitted with a polynomial of the form $\mu/\kappa = c$ - $m{\cdot}p/\kappa$; the polynomial terms for each radial model is provided in the legend. Between the scaled pressure range p/κ = 0.13–0.155 highlighted by a grey box, REM1D detects a change in the gradient of modulus ratio (μ/κ) in the central lower mantle. Similar changes are also observed in the REM1D profile of Poisson's ratio (σ_P) that is provided as Supplementary Fig. S7. The change in gradient occurs over a broad region in the depth range of ~1300–1700 km and at pressures between 52 and 73 GPa. This signature in REM1D is constrained using all reference datasets (Paper I) and is more prominent than in several models constructed with body waves in isolation (e.g. AK135, EK137). Values of the physical properties from REM1D are listed in Supplementary Table S7.

data on lower mantle grain growth rates, seismically-calibrated estimates of mineralogical parameters are unlikely to change substantially from those derived by Dannberg et al. (2017), since REM1D and the attenuation model QL6 have similar magnitudes and step changes of Q_μ in the transition zone and lower mantle.

Shear attenuation (Q_μ) in REM1D has implications for the presence of small quantities of water (~0.1 wt%) that are known to enhance anelastic effects in the mantle (e.g. Karato and Jung, 1998; Karato, 2011; Aizawa et al., 2008). Water in nominally anhydrous mantle minerals has been inferred at concentrations between 0.05 and 0.2 wt% in the upper mantle (Hirth and Kohlstedt, 1996; Hirschmann, 2006; Crowley et al., 2011) and up to ~1 wt% in transition-zone polymorphs (e.g. Pearson et al., 2014). While some seismological studies have reported low Q_μ in localized regions of the transition zone and interpreted the findings as an indication of water enrichment (e.g. Fuji et al., 2010; Zhu et al., 2013), our global inversions do not require an elevated shear attenuation at these depths. REM1D has a smooth decrease in shear attenuation from the upper mantle to the transition zone (Q_μ = 193); lower Q_μ values in the transition zone are strongly dependent on regularization and do not provide significant improvements in data fits (Section 3.1). Based on our estimates of shear attenuation that are constrained well by normal-mode overtones, the mantle transition zone is unlikely to be a uniformly hydrated layer (e.g. Karato, 2011), although water could be entrained locally where subducted slabs interact with this region. Even if the transition zone has an apparently high water solubility, actual water distribution is only indirectly controlled by this limit and can be uniformly low and quite homogeneous throughout the mantle due to the remixing of subducted water out of a 'leaky' transition zone (e.g. Richard et al., 2002).

4.4. Spin transitions in the lower mantle

A transition in the electronic spin state of iron in bridgmanite and ferropericlase is expected to occur in the central lower mantle (CLM) based on *ab initio* calculations and laboratory experiments. In ferropericlase, the spin transition associated with ferrous iron (Fe^{2+}) is expected to occur in the pressure range of $p \sim$ 50–90 GPa though the exact mineral physical estimates of its size and radial (or pressure) extent remain debated (e.g. Badro et al., 2003; Tsuchiya et al., 2006; Wentzcovitch et al., 2010; Badro, 2014). This spin transition is accompanied by softening (i.e. reduction) of the bulk modulus (κ) with negligible impacts on shear modulus (μ) and density (e.g. Wentzcovitch et al., 2009; Marquardt et al., 2018), which would manifest seismically as a more discernible change in the absolute values of v_P compared to other physical parameters (eq. 4). However, there are several reasons to expect that the seismological signatures of the spin transition may get suppressed in amplitude and broadened out in radial extent. First, the exact composition of the mineral assemblage (C) such as the amount of iron (e.g. Speziale et al., 2005; Fu et al., 2018) and aluminum (Shukla et al., 2016) is known to either shift the spin transition to higher pressures or suppress its effects. Due to the known abundance of bridgmanite in the lower mantle (~70–75 %) and its potential enrichment near the CMB (i.e. lower Mg/Si ratio; Section 4.7), the nature of spin transition in bridgmanite strongly influences observations. Presence of bridgmanite can suppress the seismological signatures since the net effect of the spin transition on its elastic properties may be small (Caracas et al., 2010) and depends strongly on the valence (ferrous/ferric) and position of iron in the silicate lattice structure (Badro, 2014). Second, spin transitions in both bridgmanite and ferropericlase are strongly temperature (T) dependent and tend to broaden with increasing temperature (e.g. Wentzcovitch et al., 2009). Third, preference of iron for the low-spin state is expected to produce changes in Fe—Mg partitioning between bridgmanite and ferropericlase (Irifune et al., 2010; Badro, 2014; Piet et al., 2016), which can modify the aggregate properties due to the dissimilar influence of iron content on the properties of these minerals. Overall, signatures of the spin transition may naturally be harder to discern from the absolute properties of radial models.

Prominent spin-transition signatures can emerge in derivative properties such as the Poisson's ratio σ_P (e.g. Fu et al., 2018) and the relative behavior of the elastic moduli (μ, κ) or the corresponding wave speeds (v_S,v_P). Based on EoS expectations, gradients of the modulus ratio (μ/κ) as a function of scaled pressure (p/κ) are expected to follow a linear relationship in regions with uniform phase and composition (e.g. Falzone and Stacey, 1980; Burakovsky et al., 2004; Kennett, 2021). The spin crossover in the lower mantle is expected to be a smooth (second-order) phase transition that modifies the pattern with distinct linear μ/κ and σ_P segments on either side of the transition region and a complex behavior within. Fig. 15 reports a dramatic change in the gradient of the modulus ratio between the scaled pressure range p/κ = 0.13–0.155 in the CLM region of REM1D. This signature consistent with spin transitions is observed over a broad region in the depth range of ~1300–1700 km and at pressures between 52 and 73 GPa. Our results favor pervasive iron spin transitions and the presence of ferropericlase in the CLM region whose unambiguous spin-transition signatures (μ/κ, σ_P) may be somewhat suppressed in the aggregate properties reported by REM1D due to different mechanisms (e.g. C, T, Fe partitioning). Moreover, lateral variations in temperature and composition (e.g. ferropericlase content) cannot be ruled out and calibrations are needed against 3D Earth models to characterize the signatures of spin transitions in various tectonic

regions.

The gradients of derivative properties are constrained by the joint sensitivity to elastic structure afforded by the new reference datasets and are not dictated by the polynomial parameterization in the lower mantle (Paper I). The v_P-sensitive spheroidal overtones require REM1D to have slightly lower v_P values (~0.1 %) than PREM throughout the CLM region (Fig. 2g). Spheroidal modes and toroidal overtones, in contrast, require substantially stronger reductions in v_S (~0.4 %) on either side of the spin-transition region. Normal modes are able to constrain both stratification (i.e. gradient) and magnitude of physical properties due to their oscillatory sensitivity kernels (Dahlen and Tromp, 1998); an increase in density, for example, can either have a positive or negative effect on eigenfrequencies depending on the depth of perturbation (Supplementary Fig. S1). The contrasts between v_P and v_S gradients along with the related changes in the modulus ratio (μ/κ, Fig. 15) and Poisson's ratio (σ_P, Supplementary Fig. S7) are more prominent in REM1D than past studies that employed body waves in isolation (e.g. AK135, EK137). Arrival times (t) of mantle waves (e.g. P, S) do not report a distinct change in their slope $dt/d\Delta$ at epicentral distances that correspond to bottoming depths in the spin transition region ($\Delta = 52°$–$68°$; Fig. 8). Since the mantle phases lack the discriminatory sensitivity to spin transitions, a wide variety of (σ_P and μ/κ) gradients in body-wave models can fit the arrival-time data equally well (Table 3) and the mild changes in AK135 gradients within the CLM region (Kennett, 2021) should be interpreted with caution. Overall, gradients of the elastic properties in REM1D afford prominent and broad signatures consistent with pervasive spin transitions that will motivate calibrations of temperature and composition in the lower mantle with the emerging mineralogical constraints.

4.5. Extent of adiabicity and large-scale homogeneity

Fig. 12 provides revised estimates of the Bullen's stratification parameter (η_B) from REM1D. Deviations in η_B values from one can be attributed to the presence of thermal boundary layers, radial anisotropy in the shallowest ~250 km of the mantle (Sections 3.3 and 4.1), and phase or spin transitions of the constituent minerals. REM1D removes the anomalous $\eta_B < 1$ values of PREM at the bottom of the transition zone (600–650 km) and reports larger values in the transition zone ($\eta_B \sim$ 2.2, 410–650 km) and the upper lower mantle ($\eta_B =$ 1.9–2, 650–771 km). The series of expected phase transitions in the constituent minerals of pyrolite may be sufficient to explain radial inhomogeneity in this extended transition zone although minor changes in bulk composition or entropy are possible as well (Sections 4.3 and 4.7).

Superadiabatic gradients can lead to the formation of low-velocity zones in both the top and bottom boundary layers of mantle convection. Near the surface, conductive heat losses lead to superadiabatic temperature gradients that dominate over any effects from changes in bulk composition, leading to low η_B (0.65–0.75) between the Moho and a depth of 150 km (eq. 11). Negative velocity gradient will appear whenever the thermal gradient exceeds a critical value such that the increase of velocity with compression is overcome by the decrease of velocity on heating (Anderson et al., 1968; Stixrude, 2007). The critical thermal gradient that must be exceeded for shear waves is

$$\beta_S = (\partial T/\partial p)_{v_S} = -\frac{(\partial v_S/\partial p)_T}{(\partial v_S/\partial T)_p}. \quad (20)$$

When temperature increases even more rapidly with increasing depth, thermal expansion counteracts and can even overcome the effect of pressure on the density, causing the density to decrease with increasing depth. The corresponding critical gradients for density is

$$\beta_\rho = (\partial T/\partial p)_\rho = \frac{1}{\alpha K_T} \quad (21)$$

where K_T is the isothermal bulk modulus employed in many EoS (e.g. Murnaghan, 1944; Birch, 1952) and derived from seismic properties (Grüneisen, 1912). Several mantle minerals follow the trend $\beta_S < \beta_P < \beta_\rho$ (e.g. Anderson et al., 1968; Stixrude, 2007), whereby a greater threshold of temperature gradients needs to be crossed for forming low-density than low-velocity zones.

REM1D detects the following low-velocity features with no corresponding reductions in density: (i) a low-v_S zone with a relatively weaker low-v_P zone in the upper mantle (Fig. 11), and (ii) a pronounced low-velocity (i.e. both v_P and v_S) zone in the D″ region (Fig. 1a). Based on a recent mineralogical compilation (Stixrude, 2007), for a mantle comprised purely of olivine, average geothermal gradients should be less than $\beta_\rho = 10$ K km^{-1} in order to avoid creating a pervasive low-density zone in the upper mantle. Absence of negative density gradients suggests that the boundary layers are gravitationally stable and not undergoing rapid overturning over geological timescales, except in regions of limited geographic extent where more dense material can overlie less dense material (e.g. mid-ocean ridges, back-arc basins). Temperature profiles will need to be calibrated based on the following features of REM1D: (i) revised average depths of the internal discontinuities (Table 1) to anchor the geotherm, (ii) thermodynamical properties for the possible bulk compositions of each principal region (Section 4.7), and relatedly (iii) temperature gradients in the boundary layers that exceed critical values to form the low-velocity zones. Based on a typical formulation of average temperature perturbations in a convecting mantle (Richter and McKenzie, 1981), REM1D structure implies that a much larger change in temperature is expected in the lowermost mantle than at the surface boundary. While the exact temperature contrast between the core and mantle remains poorly constrained, our inference on a steep temperature gradient is consistent with the large values ($\Delta T >$ 1300 K) reported by several studies (e.g. Knittle and Jeanloz, 1991; Nimmo et al., 2004).

Based on η_B values less than 1 in earlier radial models like PREM, superadiabaticity was suggested in the central lower mantle (771–2891 km depth, Fig. 12c). Past studies have reported that this principal region could accommodate around 200–300 K of excess temperatures linearly across this region on top of the adiabatic mantle geotherm (Brown and Shankland, 1981; Anderson, 1982). In contrast, the revised density structure and gradients in REM1D imply an apparent subadiabatic compression ($\eta_B \sim$ 1.01–1.04) over a broad range of pressures and temperature conditions. In order to reconcile these discrepancies, robustness of η_B variations in the central lower mantle was evaluated based on *a priori* assumptions and fits to data. This feature is recovered from a different starting model, which assumed that the central lower mantle follows the Adams-Williamson equation with a density at the CMB optimized to fit Earth's mass and moment of inertia. We tested both cubic and quartic polynomials for density inversions in order to evaluate any η_B artifacts arising from the parameterization that were evident for the core (Paper I). Similar η_B values are obtained in the central lower mantle after two iterations irrespective of the parameterization choices. An increase in η_B with depth affords improved (up to 4.6 times lower) χ^2/N misfits to the longest-period spheroidal fundamental modes ($_0S_{2-5}$), which are strongly sensitive to density variations in the lower mantle (cf. Supplementary Fig. S1 in Paper I).

The apparent subadiabaticity of the lower mantle is recovered even though we do not prescribe *a priori* constraints on the range of η_B based on mineral physical considerations. For example, even in homogeneous and adiabatic regions, an appreciable bulk attenuation can lead to a non-adiabatic contribution to the geotherm so an apparent subadiabaticity should anyway be a feature of the starting model (e.g. Heinz and Jeanloz, 1983). This bulk attenuation effect is due to the internal stresses generated from the local mismatch of the elastic moduli of neighboring grains in a given aggregate. REM1D contains finite bulk attenuation in the lower mantle ($Q_\kappa = 28{,}596$) with a small yet detectable ratio of bulk to shear dissipation ($R_q = Q_\mu/Q_\kappa = 0.8$ %) so this effect on η_B cannot be summarily ignored. In internally-heated and rapidly convecting

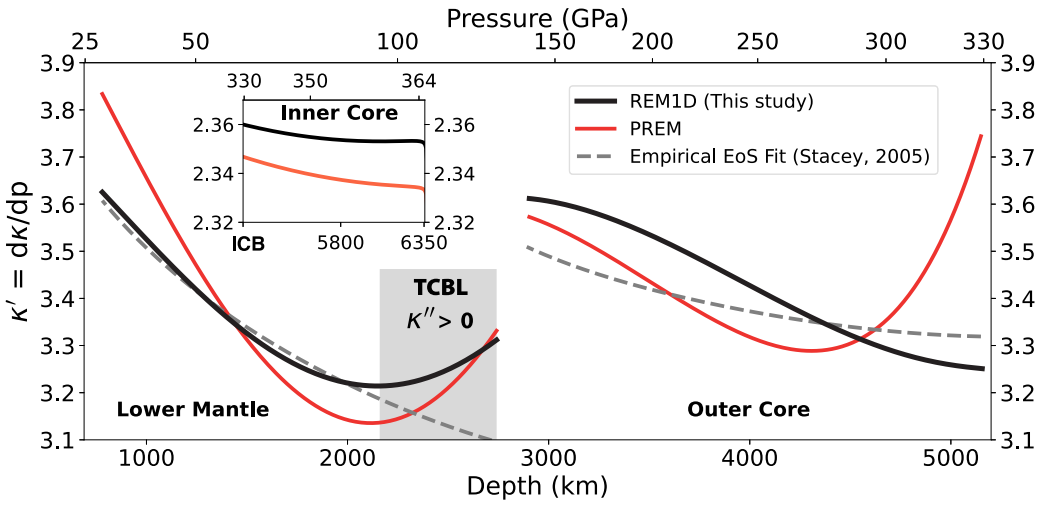

Fig. 16. Comparisons of EoS parameters in the lower mantle and outer core. Pressure derivative of bulk modulus ($\kappa' = d\kappa/dp$) is derived from the radial reference models REM1D and PREM. Based on EoS predictions for a well-mixed isochemical region, the curvature κ'' should remain negative over an entire pressure range, decreasing in magnitude to zero at high pressures ($p \to \infty$). REM1D is consistent with the expectations from mineral physics in both regions except in the bottom ~500–750 km of the mantle (Sections 4.6 and 4.9). REM1D removes the positive κ'' in the deepest ~1000 km of the outer core that is an anomalous feature of PREM and most body-wave studies (Section 3.4, Fig. 7). The curvature κ'' in REM1D becomes positive in the central lower mantle below 2135 km (p = 94–127 GPa, highlighted by a grey box), which is a signature of the thermo-chemical boundary layer (TCBL; Section 4.6). Stacey (2005) fitted a reciprocal relationship of predicting adiabatic κ parameters to PREM structure for the lower mantle and outer core; it is shown here for comparisons but does not imply a preference for this empirical EoS formulation. All κ' values on the y-axis are in the S.I. unit kg/(m·s^2·Pa), inner core is provided as an inset figure, and the D'' region ($\kappa' \sim 1.24$–1.28) is not shown. More detailed comparisons between published models on variations in the outer core are provided in Fig. 7. Values of κ' from REM1D are listed in Supplementary Table S7.

interiors of the lower mantle, a subadiabatic geotherm can be expected (Parmentier et al., 1994; Monnereau and Yuen, 2002), and geodynamic simulations suggest a value of $\eta_B \sim 1.01$ from this effect (Bunge et al., 2001; Matyska and Yuen, 2000). Spin crossovers in the iron-bearing ferropericlase (Section 4.4) can cause positive excursions of η_B to ~1.02 (Valencia-Cardona et al., 2017), albeit with a maximum near 1900 km depth rather than the 2741 km in REM1D. If the lowermost ~500–750 km of the mantle is enriched in silica (Section 4.7), the related reduction in ferropericlase content will suppress or even nullify the contribution of spin transitions to our η_B values. Subadiabatic gradients may also develop as convective flows are forced to turn from vertical to horizontal advection in the boundary layers (e.g. Mckenzie et al., 1974; Sinha and Butler, 2007). The resulting overshoot of η_B to subadiabatic values may be restricted to a narrow region atop the bottom thermal boundary layer in a vigorously convecting mantle but may also spread out over a broader region if internal heating is substantial (Sinha and Butler, 2007). Lower-mantle heat flow estimates are largely uncertain, though a substantial fraction could be from internal heating due to radiogenic heat production (Jaupart et al., 2007; Lay et al., 2008). Overall, bulk attenuation, spin transition, advection and internal heating cause relatively small η_B fluctuations (~0.01–0.02) in a purely thermal convection regime with uniform bulk composition. Our η_B values are relatively large (> 1.03) and have steep positive gradients towards the bottom of the CLM region.

Our estimates of the Bullen's stratification parameter can be reconciled with the presence of a pervasive thermo-chemical boundary layer in the lowermost mantle. Thermal contributions, like core heating, cause superadiabatic temperature gradients at the bottom of the mantle and thus the presence of a thermal boundary layer (Loper and Stacey, 1983), which manifests as a strong monotonic reduction of η_B in the D″ region. The lowermost ~500–750 km of the mantle is also a region where chemically distinct material is likely to gravitationally stabilize (Fig. 12c). This would lead to a chemical mixture of at least $n = 2$ components where C_1 represents a constant composition throughout the lower mantle (e.g. pyrolite) and C_2 is a chemically distinct component whose amount increases with depth (e.g. monotonic or parabolic function) reaching its maximum at the CMB. There is however a tradeoff between temperature and composition gradients when interpreting η_B values (eq. 11). Chemical stratification in this region can suppress the η_B signal of superadiabatic gradients in the bottom thermal boundary layer, explaining the substantially larger values in the D″ region ($\eta_B \sim$ 0.98–0.99) than is expected from purely thermal geodynamic simulations ($\eta_B \sim$ 0.8–0.9; e.g. Bunge et al., 2001; Matyska and Yuen, 2002). The detailed thermodynamical properties of this intriguing boundary layer are beyond the scope of this study as they would require joint calibrations of bulk composition (e.g. n and C_i) and thermal profiles (i.e mantle adiabat and the deviation τ) against the seismological features in REM1D.

4.6. *Lowermost mantle and the D″ region: A thermo-chemical boundary layer*

REM1D detects large deviations from PREM in the lowermost mantle and D″ region (Fig. 2g), which have important implications for the thermo-chemical state of this boundary layer. Based on summary arrival-time curves and normal-mode eigenfrequencies, REM1D exhibits uniformly slow shear- and compressional-wave velocities (up to ~1 % relative to PREM) in the lowermost mantle with negative gradients in the D″ region. Negative velocity gradients atop the CMB were suggested by some early seismological studies based on PcP/P amplitudes (e.g Buchbinder, 1968; Müller et al., 1977) and diffracted S_{diff} waves (e.g Cleary, 1969); scatter in the measurements, limited geographic coverage and inconsistency with travel time observations prevented a robust detection in earlier studies. The pervasive low-velocity zone in the D″ region can be reconciled with solely solid-state mechanisms and steep temperature gradients without requiring a partially molten basal layer (Section 4.5).

Chemical stratification in the lowermost ~500–750 km of the mantle can be favored based on the following features in REM1D: (i) relatively large η_B (> 1.03) with steep positive gradients till 2741-km depth followed by an abrupt reduction to values below one (0.98–0.99) near the CMB (Fig. 12c), (ii) very steep negative v_P and v_S gradients that form a

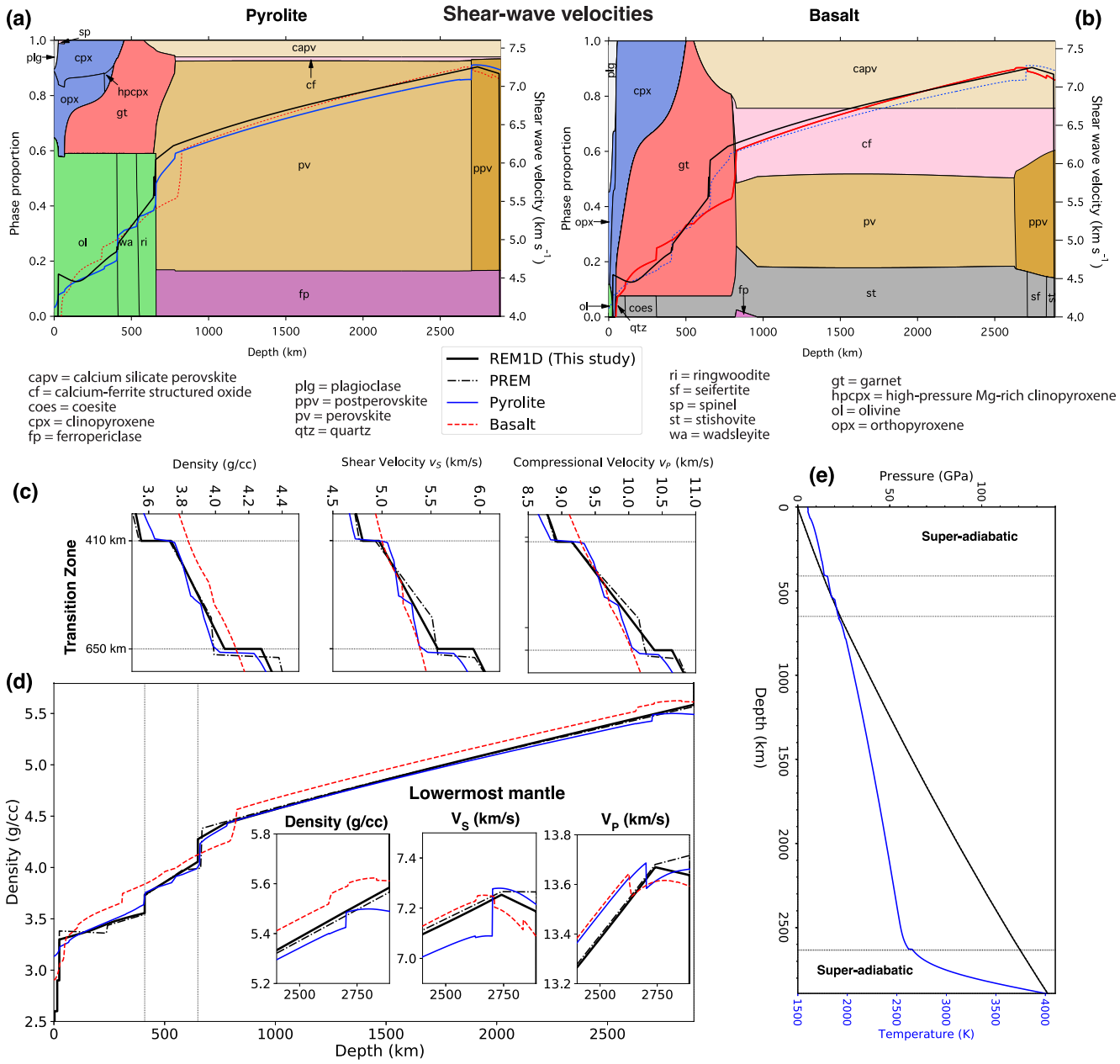

Fig. 17. Comparisons of REM1D with mineralogical predictions. Phase proportions (atomic fraction) of (a) pyrolite and (b) basalt as bulk composition of the entire mantle. Shear-wave velocities are superimposed from pyrolite (blue), basalt (dashed red) and the radial reference models REM1D and PREM. Curves are repeated in both panels to facilitate comparisons. Insets figures zoom into the (c) transition zone and (d) the lowermost mantle. Profiles of elastic parameters and density for the two bulk compositions were calculated along an adiabat with the potential temperature of 1600 K and a superadiabatic thermal boundary layer in the lowermost 300 km of the mantle (Stixrude and Lithgow-Bertelloni, 2011, 2012), as shown in (e) along with the corresponding pressures.

low-velocity zone in the D″ region with no corresponding reduction in density, (iii) up to 0.5 % increase in density relative to PREM and steeper positive gradients $d\rho/dz$ (Fig. 2g), and (iv) variations in κ' that are inconsistent with the expectations for EoS of a uniform composition (Fig. 16). While a thermal boundary layer with superadiabatic gradients may partly explain the first two features (Section 4.5), satisfying all four requires a thermo-chemical boundary layer in the bottom ~500–750 km of the mantle.

We focus our attention in this section to the κ' variations in the lowermost mantle since the other features have already been discussed (Section 4.5). In an earlier study, EoS parameters were fitted to the PREM lower mantle by adopting an overall superadiabatic temperature gradient (excess 200 K) in the lower mantle (i.e. related to $\eta_B < 1$ in PREM, Fig. 12c), and a 150-km thick thermal boundary layer near the CMB (Stacey and Davis, 2004; Stacey, 2005). The κ' values in REM1D are substantially lower than PREM and show similar trends as predicted by the fitted EoS between 771 and 2000 km. Our κ' features are not prescribed during model construction and are largely the outcome of steeper gradients and curvature in v_S structure of the REM1D lower mantle (Fig. 2g). The sign of κ'' is reversed and becomes positive in the central lower mantle below 2135 km ($p = 94$–127 GPa), highlighted by a grey box in Fig. 16, which is not expected for EoS of a uniform composition. While choosing a specific EoS formulation and fitting new thermodynamical parameters for the lower mantle are beyond the scope of this study, a thermal boundary layer with a uniform bulk composition cannot be reconciled with the derivative properties of REM1D.

The large temperature contrast across this boundary layer ($\Delta T = T_{CMB} - T_0$) results in thermal buoyancy ($\Delta\rho_T = \alpha\rho_0\Delta T$), which counter-

acts the chemical buoyancy arising from the intrinsic density of the material ($\Delta\rho_C = \rho_0\beta C$). Here, subscript '0' denotes properties at the reference temperature T_0 (typically the room temperature), β is the excess density of the chemically distinct material (in %), and C denotes its concentration with depth (eq. 11; e.g. Farnetani, 1997). Depending on the buoyancy ratio ($B = \Delta\rho_C/\Delta\rho_T$), a dense basal layer can stabilize relative to the overlying/ambient mantle and act as the source region for long-lived thermo-chemical plumes (e.g. Hansen and Yuen, 1988; Le Bars and Davaille, 2004; Tackley, 2012). Chemical buoyancy can dominate over thermal buoyancy in the lowermost ~500–750 km of the mantle due to compositional gradients (Section 4.5), also supported by the reduced thermal expansion (α) at high pressures conditions (e.g. Chopelas and Boehler, 1992; Duffy and Ahrens, 1993; Trampert, 2004). While estimates of B based on the REM1D density profile will require joint thermo-chemical calibrations (Section 4.5), some first-order features are readily apparent. A density excess in the lowermost mantle does not afford better fits to normal mode data than REM1D in agreement with Masters and Gubbins (2003). A less dense region is not reported by our inversions and is also disfavored based on physical reasons, as it would be gravitationally unstable and fail to persist as a pervasive feature due to overturning over geological timescales. Due to the superadiabatic temperature profile in the lowermost mantle, total density ($\rho = \rho_0$ - $\Delta\rho_T + \Delta\rho_C$) sensed by the seismic waves (e.g. longest-period normal modes) is lower than the intrinsic chemical density of the material. Superadiabatic temperatures will tend to suppress the seismological signatures of excess density arising from the chemically distinct components whose amounts are likely to increase with depth in this boundary layer (Section 4.5).

The low-velocity, dense region at the bottom of the mantle lies within the depth range where perovskite (Pv) could transform to the high-velocity post-perovskite (pPv) in the lowermost mantle (e.g. Murakami et al., 2004). If the entire lowermost mantle lay within the post-perovskite stability field in a purely thermal regime with a homogeneous pyrolitic composition, step changes in shear-wave velocities and density at ~2741 km would be a pervasive feature. There is no apparent need for a systematic step change based on summary arrival time curves and mode eigenfrequencies, especially for the diffracted P_{diff} and S_{diff} arrivals that are sensitive to structure at the bottom ~200–300 km of the mantle. An overall reduction of velocities but not of density in the D″ region (Fig. 17d) may suggest that either the Pv-pPv phase transition is not a global feature or its physical effects are masked by compositional gradients in the thermo-chemical boundary layer. Other mineralogical (e.g. Catalli et al., 2009; Grocholski et al., 2012; Houser, 2007) and geodynamic (e.g. Nakagawa and Tackley, 2006) considerations could also limit the geographical extent of the post-perovskite stability field.

Radial structure in the lowermost mantle can also inform our understanding of localized features in the D″ region known as ultra-low velocity zones (ULVZs). Local waveform studies based on complexity in body-wave arrivals have documented the occurrence of several ULVZs in the lowermost mantle with velocity reductions in the range of 10–30 % (e.g. Thorne and Garnero, 2004; Rost et al., 2005; Cottaar and Romanowicz, 2012; Yuan and Romanowicz, 2017). While the lateral extent of ULVZs is debated, such localized detections are likely getting reflected in the global average (REM1D) and a substantial portion of the D″ region may be slower than what was inferred in previous studies. Since our average velocities are up to ~1 % lower than PREM in the D″ region, strength of variations in localized ULVZs may need to be updated relative to the new baseline structure. Revised amplitudes of ULVZs can have important implications for the relative contribution of partial melt (e.g. Williams and Garnero, 1996), iron enrichment (e.g. Buffett et al., 2000) and the Pv-pPv phase transition (e.g. Mao et al., 2006).

4.7. Inferences on bulk composition

Both the absolute physical properties and step changes across the internal discontinuities in REM1D provide constraints on the bulk composition of the Earth's interior. We employed reference datasets in model construction that afford sensitivity to both depth integrals of structure (e.g. surface wave dispersion, normal mode frequencies) and the step changes across transition-zone discontinuities (e.g. body-wave impedance contrasts). Both gradients and step changes of velocities and density in the depth range of ~400–1000 km evolve during the iterative inversions and are not dictated by the starting model or regularization from Paper I. The tradeoff between gradients and step changes are low due to the sensitivity afforded by normal-mode overtones and body waves; radial variations similar to within 1 % are obtained irrespective of the damping that modulate step changes (γ_d). For comparisons of absolute seismic properties with those predicted by mineral physics (Fig. 17), we use the elastic moduli as a function of pressure and temperature calculated by Stixrude and Lithgow-Bertelloni (2011, 2012). These calculations assume either a pyrolite or basalt composition (e.g. Workman and Hart, 2005; Xu et al., 2008), and superadiabatic gradients in the bottom ~300 km of the mantle. To first order, profiles of absolute velocities and density in REM1D are fit well by an olivine-dominated pyrolitic composition throughout the upper mantle and extended transition zone down to a depth of ~800 km.

Phase transformations are highly sensitive to bulk composition and even slight changes in mantle chemistry can dramatically change the expected radial structure. Key seismological constraints for inferring the mantle composition and calibrating the geotherm are gradients and step changes of velocity and density in the mantle transition zone (410–650 km) and the upper lower mantle (650–771 km). REM1D has stronger gradients in physical properties than PREM and ~30 % weaker impedance contrast at the 650-km discontinuity (Z_S = 11.6 %, Table 4). Our results agree with mineralogical estimates of multiphase assemblages with a pyrolitic composition from both *ab initio* simulations and laboratory experiments (cf. Table 3 in Paper I), consistent with the inferences in several studies (e.g. Ita and Stixrude, 1992; Gaherty et al., 1999b; Lessing et al., 2015). The step change in density at the 650-km discontinuity is reduced to almost half in REM1D (5.3 %) compared to PREM (9.3 %); our new estimates are more consistent with the dissociation of a high volume fraction (52–76 %) of ringwoodite in a pyrolitic composition (e.g. Yu et al., 2007). We detect a small step change in v_P across the 650-km discontinuity (2.5 %), which corresponds to a negligible contrast in bulk-sound speed (v_Φ) and a small contrast (1.1 %) in the Lamé parameter λ (Table 4). These negligible step changes at the bottom of the transition zone are broadly consistent with a seismological study that favored prescribing zero contrasts (i.e. $\%v_\Phi = \%\lambda = 0$; Estabrook and Kind, 1996), and are within the bounds for Mg-rich ringwoodite reported by *ab initio* calculations (e.g. $\%v_\Phi = -0.1 \pm 0.48$; Yu et al., 2007; Wentzcovitch et al., 2010). Predictions from multi-component mineral assemblages also predict lower Z_P impedance contrasts than PREM (13.9 %) at the 650-km discontinuity (cf. Table 3 of Paper I). Mineralogical estimates of Z_P contrasts range from ~7–9 % for pyrolite across a range of potential temperatures (1500–1700 K) (Weidner and Wang, 2000; Xu et al., 2008; Stixrude and Lithgow-Bertelloni, 2011). Low amplitudes of $P_{650}P$ that are related to low Z_P impedance contrasts have been reported in both global stacks of long-period seismograms (e.g. Estabrook and Kind, 1996; Shearer and Flanagan, 1999) and related vespagrams (e.g. Deuss, 2009). Some studies have claimed regional detections of the $P_{650}P$ precursor over a range of depths and attributed this to chemical variations (e.g. Deuss et al., 2006; Waszek et al., 2021); potential localized features can be evaluated with full 3-D tomographic models that solve jointly for velocity and the topography of discontinuities (e.g. Gu et al., 2003; Moulik and Ekström, 2014, 2016).

REM1D contains steep gradients in v_P, v_S and density in the upper lower mantle (ULM, 650–771 km) that are consistent with mineralogical expectations for pyrolite (Fig. 17). In contrast, PREM reported steep gradients in velocities without a corresponding increase in density gradients (Fig. 2), which leads to an abrupt decrease of the Bullen's stratification parameter (η_B) to values below 1 in this region (Fig. 12b,

eq. 10). Superadiabatic gradients are not expected in the ULM region and any chemical or phase transitions will likely lead to an increase of η_B with depth (Section 2.1, eq. 11). The ULM region is part of the extended mantle transition zone (650–771 km) and corresponds to depths where transitions from all upper mantle minerals (olivine, enstatite, and garnet) to their high-pressure polymorphs (perovskite, ferropericlase, and calcium perovskite) are completed (e.g. Stixrude and Lithgow-Bertelloni, 2011). This feature is seen in mineralogical models as the signature of the garnet to perovskite transition, which is gradual and spread out over more than 100 km in depth (Weidner and Wang, 1998). Most features in REM1D are more in agreement than PREM with a olivine-dominated composition with a residuum comprising all other phases (e.g. garnet, clinopyroxene) as the bulk composition in the upper mantle and extended transition zone in agreement with several mineral physical and petrological studies (e.g. Ita and Stixrude, 1992; Jackson and Rigden, 1996).

Pyrolite offers a viable explanation for the REM1D structure in the shallowest ~800 km of the mantle but not a unique one and a few discrepancies seen in earlier studies persist. A component of lithologic heterogeneity within the same aggregate bulk composition may be required to improve the fits to our profiles of absolute velocities (e.g. Xu et al., 2008; Stixrude and Lithgow-Bertelloni, 2012; Cammarano et al., 2009). A relatively gradual 520-km discontinuity is predicted by mineralogical models but was excluded from REM1D due to its highly variable nature in regional studies (Deuss, 2009) and absence in global stacks of reflected body waves (Gu et al., 1998). Baseline or systematic discrepancies between REM1D and mineralogical predictions can be due to: (i) using anharmonic moduli (infinite frequency limit) without accounting for physical dispersion from our attenuation model (Section 3.1), (ii) phase transformations in pyroxene and garnet that may act to split or suppress the olivine-dominated discontinuities (e.g. Weidner and Wang, 2000; Saikia et al., 2008), (iii) imperfect knowledge of key mineralogical properties like the temperature dependence of shear modulus in lower mantle minerals (e.g. Stixrude and Lithgow-Bertelloni, 2022), or (iv) calculations along an adiabat with fixed upper mantle potential temperature of 1600 K without exploring the parameter space of published values that typically range from 1550 to 1670 K (e.g. McKenzie et al., 2005; Herzberg et al., 2007; Courtier et al., 2007; Putirka, 2008). Another discrepancy lies in velocity (but not density) contrasts at the 410-km discontinuity, where REM1D reports ~1.5 times lower values (ν_P = 2.5 %, ν_S = 3.4 %, Table 4) than mineralogical predictions for pyrolite (Fig. 17, cf. Table 3 in Paper I). Enriching the olivine-poor piclogite composition (Bass and Anderson, 1984) in various elements (e.g. Al, Na; Gasparik, 1990; Ita and Stixrude, 1992) could afford an alternative albeit conceptually complicated way to fit REM1D structure.

Our comparisons do not demonstrate a strong preference towards either depletion or enrichment in basalt atop or within the mantle transition zone associated with subducted slabs (e.g. Xu et al., 2008; Yu et al., 2023). Pure basalt does not predict step changes in ν_P, ν_S and density structure at 410 and 650 km within the uncertainty bounds of the reference datasets or the preferred estimates from REM1D (Fig. 17b, c) so its volume fraction needs to be generally low to be consistent with seismology. Mechanisms such as a pervasive mechanical mixture of basalt from oceanic crust formation and its complementary residue can explain the overall low volume fractions in this region ($\ll$30 wt%; Stixrude and Lithgow-Bertelloni, 2012; Yan et al., 2020). Global estimates of basalt fraction may be low in this region if basalt segregation is restricted to regions of Cenozoic subduction and the recycled basaltic components from deeper regions are not stored due to a 'leaky' transition zone. Regional enrichment in basalt is possible and can be probed with tomographic models that employ data particularly sensitive to the transition zone (e.g. Fukao and Obayashi, 2013; Moulik and Ekström, 2014). A detailed mapping of basalt fraction in the transition zone will require self-consistent modeling of thermodynamical and seismological constraints.

Changes to bulk composition from the chemical stratification in the bottom ~500–750 km of the mantle (Section 4.6) can be attributed to various processes: (i) gradual MORB enrichment (e.g. Deschamps and Trampert, 2004; Xie and Tackley, 2004; Nakagawa and Buffett, 2005; Matas et al., 2007; Ricolleau et al., 2010), (ii) primordial material with greater proportion of bridgmanite than ferropericlase (e.g. Ballmer et al., 2017; Gülcher et al., 2020), and (iii) crystallization of a primordial basal magma ocean (Nomura et al., 2011). The first two processes can enrich the lowermost mantle (depth ~ 2000 km–CMB) in silica (i.e. lower the Mg/Si ratio) relative to a pyrolitic composition in the upper mantle and extended transition zone (24.4–771 km). A thermo-chemical layer with pervasive silica enrichment could reconcile the discrepancies in silica content between pyrolite (Mg/Si ratio = 1.2–1.3) and bulk silicate Earth estimates based on CI chondrites (Mg/Si ratio = 0.9–1.1), which represent the rocky building blocks of the solar system (Hart and Zindler, 1986; McKenzie et al., 2005; Murakami et al., 2012). Estimating the bulk composition of such a layer is important for deriving properties like critical gradients that help calibrate the mantle geotherm (eqs. 20 and 21). Due to the tradeoff in temperature and composition when fitting radial models (e.g. Ita and Stixrude, 1992; Weidner and Wang, 2000; Ballmer et al., 2017; Houser et al., 2020), elucidating the exact amount of silica enrichment and its radial distribution will benefit from jointly optimizing the temperature and composition profiles accounting for the pertinent features in REM1D (e.g. Sections 4.5 and 4.6).

4.8. Relation to mantle geodynamics and isotope geochemistry

We have restricted our discussion to geological interpretations that can be informed by signatures in average seismic properties and their derivatives (e.g. η_B, κ', μ/κ, σ_P). Elucidating the time history and relative importance of the contributing geological processes has purposefully been excluded. For example, processes that determine the deposition and evolution of the pervasive thermo-chemical boundary layer in the lowermost mantle are yet to be ascertained. The lowermost mantle is a potential candidate for a geochemical reservoir either primordial in origin (e.g. Labrosse et al., 2007), an outcome of the interactions with the iron-rich outer core (e.g. Knittle and Jeanloz, 1989) or as a possible 'graveyard' of dense mineral assemblages sourced from the phase transformation of subducted oceanic crust at the base of the transition zone (e.g. Christensen and Hofmann, 1994). Relative importance of these processes likely varies in space and time due to the inherent time-dependence of plate tectonics and continental cycles that is not captured by a 'snapshot' seismological Earth model like REM1D. Average (an) elastic and density structure is unlikely to change abruptly over geological timescales and is constrained using geophysical data that have higher precision (Paper I) than mineral physics (e.g. Matas et al., 2007; Murakami et al., 2012). Moreover, no interpretative assumptions on bulk composition and temperature profile were adopted while constructing REM1D; calibration of mineralogical models and geodynamic simulations against our average structure can therefore afford independent first-order information (e.g. Dannberg et al., 2017). For example, irrespective of their origin and evolution, higher-density or chemically distinct components will tend to either gravitationally stabilize or thermodynamically equilibrate at greater depths explaining some features seen in REM1D (Sections 4.5 and 4.6).

In the preceding sections, we have discussed bulk chemical composition in terms of mineral phases or elements ignoring their isotopic composition. While physical parameters in REM1D cannot automatically discriminate between different elemental isotopes, observed signatures of the thermo-chemical boundary layer are broadly consistent with expectations from geochemistry. Geochemical observations require extensive regions of the mantle where basaltic oceanic crust accumulates, thereby depleting other regions of the mantle in these components (e.g. Tucker et al., 2020). If we attribute lower-mantle features in REM1D to the post-Archaean convection regime that is relatively well constrained (e.g. Ullrich and Van der Voo, 1981; Becker et al., 2009),

mineralogical comparisons reveal that a non-negligible amount of a basaltic component could explain the steeper density gradients and derivative properties (η_B, κ') in the lowermost mantle (Sections 4.5–4.7). Since the transition zone structure and step changes across 410- and 650-km discontinuities do not afford a clear signature of pervasive basalt enrichment in a 'leaky' transition zone (Section 4.3), the lowermost mantle is likely to serve as the slab 'graveyard' that preserves the remnants of oceanic crust. Several geochemical and petrological observations can be reconciled with a model of the descent, ponding and ultimate fate of subducted slabs in the Earth's mantle (e.g. Ringwood, 1982; Hofmann and White, 1982). Geochemical diversity of MORBs versus OIBs can be explained by the accumulation of some basalt-bearing subducted crust in the lowermost mantle, a likely source of ocean island lavas (e.g. Zindler and Hart, 1986; Kellogg et al., 1999; Hofmann, 2003). Incompatible element enrichment is characteristic of several isotopic systems (e.g. $^{235/238}$U-^{232}Th-$^{206/207/208}$Pb, ^{87}Rb—^{87}Sr, ^{187}Re—^{187}Os and ^{146}Sm—^{142}Nd) that contain signatures of the recycled oceanic crust (e.g. Shirey and Walker, 1998; Hofmann, 2003; Boyet and Carlson, 2005), while other isotopic systems (e.g. ^{3}He/^{4}He, ^{182}W, ^{20}Ne, ^{40}Ar, ^{129}Xe, ^{100}Ru) contain signatures of a primordial source of heterogeneity (e.g. Jackson et al., 2010; Mukhopadhyay, 2012; Touboul et al., 2012; Peters et al., 2017; Fischer-Gödde et al., 2020). Geodynamical simulations have reported that chemically distinct material, either primordial in origin or accrued by recent plate tectonics, can be shaped into extensive piles or blobs of distinct composition in the lowermost mantle (e.g. Tackley, 1998; McNamara and Zhong, 2004; Ballmer et al., 2017; Gülcher et al., 2020), which would manifest themselves in the average elastic and density structure.

4.9. Thermodynamical state of the core

REM1D structure is consistent with a neutrally stable, homogeneous and adiabatic outer core characterized by the equivalent conditions Brunt-Väisälä frequency N^2=0 and Bullen's stratification parameter η_B=1 (Figs. 7 and 12b). We adopted a quartic (n = 4) polynomial for density to prevent spurious interpretations of inhomogeneity or non-adiabicity in the outer core (cf. Section 4.1.4 in Paper I). This slight adjustment to the parameterization is sufficient to reduce the artifacts in η_B and N^2 to within the uncertainty bounds of EoS parameters. Minor deviations of the Bullen's parameter ($|\eta_B - 1| \leq 0.005$) are within the uncertainties arising from numerical precision or parameterization and should not be interpreted at this time (Paper I). REM1D reports stronger v_P and ρ gradients and up to 0.5 % lower v_P than PREM in the outermost outer core (Section 3.4, Fig. 2g). Even with the changes to v_P structure, derivative properties in REM1D (N^2, η_B) remain close to the expectations of homogeneity and adiabicity with density gradients that closely follow the Adams-Williamson equation. Based on our modeling, there is no apparent need to invoke a stably stratified thermal or chemical boundary layer close to the ICB (e.g. Gubbins et al., 2008) or in the outermost outer core (e.g. Lay and Young, 1990; Buffett et al., 2000). Based on thermodynamic models of core evolution (e.g. Braginsky, 1963; Loper and Roberts, 1977; Buffett and Seagle, 2010), lighter elements may migrate upwards as the liquid iron alloy cools and crystallizes near the liquidus thereby forming thin distinct layers close to the core boundaries (CMB and ICB). REM1D is able to fit arrival times of core phases with a smooth v_P curvature in the bottom ~300 km of the outer core near the ICB (Fig. 7a). A more dramatic reduction of velocity gradient in this region (e.g. AK135, EK137) is not required to adequately fit the arrival times (±0.25 s) of the different branches of PKP (Fig. 9, Table 3). If radial inhomogeneity is indeed present, possible reasons for the null detection in REM1D include: (i) the layer is too thin ($\ll$ 100 km) to influence normal modes and the propagation of body waves globally, or (ii) the signal is subdued due to competing contributions from temperature (i.e. non-adiabaticity) and composition (e.g. eq. 11). Detecting a very thin boundary layer and disentangling thermo-chemical effects within such a layer is beyond the scope of this study. The outer core is perhaps the only principal region where homogeneity and adiabicity may be expected throughout due to its very low viscosity and the resulting well-mixed characteristics (e.g. Stevenson, 1981).

At the pressure range of 136–329 GPa within the outer core, the range of κ' in REM1D (3.25–3.61) and its variation (i.e. negative κ'') are physically plausible for a well-mixed region with uniform phase and composition (Figs. 7 and 16). Based on liquid state theory, irrespective of the temperature profile within the outer core (i.e. adiabatic, isothermal, intermediate), κ' is expected to follow a linear relationship with pressure p with a range that is consistent with REM1D values ($\kappa' \simeq 5–5.6 \cdot p/\kappa$; Stevenson, 1980, 1981). In contrast, PREM and most body-wave models contained an anomalous reversal of sign in κ'' at the bottom 1000 km of the outer core (Fig. 7h), a feature that does not afford significantly better fits to the reference datasets (Section 2.4). REM1D does not contain the very steep velocity gradients in the lowermost ~150 km of the outer core reported by some body-wave studies (e.g. Song and Helmberger, 1995; Zou et al., 2008), which would lead to very abrupt changes in η_B and κ' values (Fig. 7e,g).

EoS parameters from mineral physics can be precisely fitted to the smooth high-order derivatives and absolute variations of REM1D due to its modular parameterization in terms of analytical basis functions (Section 2.2, cf. Appendix A in Paper I). REM1D has stronger v_P gradients in the outer core and removes the anomalously positive κ'' values near the ICB found in PREM (Figs. 7h and 16). Previous EoS parameters based on the PREM outer core will therefore need to be re-calibrated. For example, Stacey (2005) fitted empirical EoS to PREM structure, which do not account explicitly for the properties of individual minerals in an assemblage that can be characterized using laboratory experiments and *ab initio* studies. The bounds on mineralogical parameters provided by such empirical EoS are nevertheless useful for seismological comparisons since no calibration for the underlying bulk composition is needed. The fitted EoS parameters based on a reciprocal κ' relationship (Stacey, 2005) are clearly inconsistent with the steeper curvatures (i.e. larger $|\kappa''|$) in the REM1D outer core. In the inner core, REM1D revises the velocity structure (Fig. 1) and derivative properties (κ' = 2.35–2.36, Fig. 16) that will need to be calibrated against empirical EoS formulations (e.g. Stacey and Davis, 2004) and *ab initio* or experimental data at extreme conditions (p > 300 GPa; e.g. Mao et al., 1998; Laio et al., 2000; Merkel et al., 2005). Such calculations can afford insights on the bulk composition (i.e. phase of iron and lighter element concentrations) and temperature profile of this remote principal region (e.g. Jephcoat and Olson, 1987; Davies et al., 2015; Hirose et al., 2021). Fitting EoS parameters (e.g. Stacey and Davis, 2004; Cobden et al., 2009; Deschamps and Trampert, 2004) with an appropriate formulation (e.g. Birch, 1947; Vinet et al., 1987; Roy and Roy, 2001) may have synergistic applications in the study of Super-Earths (e.g. Duffy et al., 2005; Seager, 2013; Boujibar et al., 2020; Kraus et al., 2022).

5. Conclusions and outlook

While early admonitions regarding the dangers of excessive confidence about the Earth's deep interior still ring true (Birch, 1952, p. 234), our approach leverages the tremendous progress in the geosciences over the past few decades and undoubtedly increases the certitude of information. While there is a growing body of evidence on lateral heterogeneity in most principal regions of the Earth, this study improves our understanding of the ostensibly simpler 1D structure. While 3D tomographic models may seem like a natural and more attractive alternative for all geological interpretations, this premise overlooks several important issues. Features in 3D models are often influenced by the limitations in theory or observations (e.g. ignoring anisotropy or attenuation, excluding portions of the ~1–3200 s band) and the prior information contained in the baseline or starting 1D model (e.g. v_P/v_S ratios). We extend the technique of full spectrum tomography (FST) to

the construction of radial models that account for the observational bias and non-linear effects arising from heterogeneity in the crust and mantle (Paper I). We interpret features only after REM1D has been constructed to optimally fit the new reference datasets. Prior information from petrology and mineral physics inform the starting model, parameterization and regularization (Paper I); however, all physical parameters are allowed to evolve during our iterative inversions. Improvements in theory and observations can reveal new features of the Earth that improve geological interpretations.

REM1D is the first radial reference Earth model to constrain the spherical average of density and (an)elastic heterogeneity using multiple types of seismological and astronomic-geodetic observations. New seismological datasets spanning three orders of magnitude in frequency (~0.3 mHz – 1 Hz) can be reconciled with a radial model without the need to invoke a frequency dependence of attenuation ($\alpha_Q = 0$). All physical parameters in REM1D vary smoothly between the Moho and 410-km discontinuity, thereby excluding the 220-km discontinuity imposed *a priori* in several models. REM1D fits all subsets of reference datasets up to ~100 times better (i.e. lower χ^2/N misfits) than all radial models published to date. REM1D is the first anisotropic model that predicts arrival times of major mantle and core phases in agreement ($\pm$0.8 s, $\psi_{pb} \leq 0.25$ s) with widely used but theoretically incomplete isotropic velocity models that were optimized for earthquake location (e.g. AK135, SP6). In practice, the effects of lateral heterogeneity on earthquake locations cannot be captured by a single radial velocity model even when corrections for local structure beneath the stations are adopted. A three-dimensional model constructed using REM1D as the baseline structure would predict the geographically unbiased arrival times necessary for deriving locations of earthquakes and explosions (e.g. Antolik et al., 2001).

Robust structural features necessary to fit the reference datasets are detected everywhere in the Earth. The v_P and ρ variations in the outer core have steep gradients and the derivative properties are consistent with a neutrally stable region comprising a well-mixed iron alloy undergoing adiabatic compression ($\eta_B \simeq 1, N^2 \simeq 0$, negative κ''). A strongly attenuating ($Q_\mu \sim$ 60–80), low-v_S zone is found at a depth of ~150–175 km corresponding to a mechanically weak asthenosphere. Substantial anisotropy is required only in the shallowest ~250 km of the mantle primarily due to LPO-style textures of intrinsically anisotropic grains arising from horizontal flow. The step change in shear attenuation ($\Delta Q_\mu = 156$) at the 650-discontinuity can be due to the combined effects of unit-cell scale reordering that accompanies the breakdown of ringwoodite and a reset of post-reaction grain sizes. Finite bulk attenuation is detected throughout the mantle with two parameters above ($Q_\kappa = 385.62$) and below the 410-km discontinuity ($Q_\kappa = 28{,}596$). An olivine-rich pyrolitic composition is broadly consistent with REM1D structure and the derivative properties (η_B) in the shallow regions down to a depth of ~800 km including the step changes at the 410- and 650-km discontinuities. Reduced density contrast at the 650-km discontinuity and a smooth gradient below suggest that this extended transition zone may act as a 'leaky' boundary layer for convection (e.g. Christensen and Yuen, 1985; Tackley et al., 1993), which impedes but does not completely prevent flow of mass and heat between the upper and lower mantle.

Radial structure of the mantle deeper than ~800 km may necessitate temperature gradients, heat flux, phase or spin transitions, thermal boundary layers and chemical stratification. Features of the REM1D lower mantle can be explained in terms of: (i) effects of thermally driven convection throughout the central lower mantle (771–2741 km) leading to an apparent subadiabaticity in η_B, (ii) effects of spin transitions in iron-bearing minerals leading to a change in the linear gradients of μ/κ and σ_P on either side of a transition region (~1300–1700 km, 52–73 GPa), (iii) a thermal boundary layer with larger superadiabatic gradients than near the surface, which ultimately exceed the critical gradients for both v_P and v_S (but not for density) at a depth of 2741 km, and (iv) chemical stratification in the bottom ~500–750 km of the mantle that acts to suppress the thermal effects. Several features of absolute elastic and density variations in the lowermost mantle cannot be easily reconciled with purely thermal variations (Section 4.6). Chemical stratification in this region is consistent with the evidence of denser-than-average heterogeneity (~1 % peak-to-peak anomalies) roughly coincident with the large-scale slow-velocity superplumes beneath the Pacific Ocean and Africa from full-spectrum tomography (Moulik and Ekström, 2016), which has been substantiated by a sensitivity analysis of solid Earth tides (Lau et al., 2017). Density structure can afford the clearest signature of thermo-chemical variations but early normal-mode studies were inconclusive (Ishii and Tromp, 1999; Resovsky and Ritzwoller, 1999; Masters et al., 2000a; Kuo and Romanowicz, 2002). Recent advancements are due to techniques that can invert diverse observations to reduce inter-parameter tradeoffs (e.g. FST; Moulik and Ekström, 2016), new measurements of density-sensitive longest-period normal modes (e.g. ${}_0S_2$ at ~3200 s; Häfner and Widmer-Schnidrig, 2013; Deuss et al., 2013), and theory to express solid Earth tides with this dominant mode of deformation (~95 % ${}_0S_2$ contribution; Lau et al., 2015). Suggestions of purely thermal variations in the lowermost mantle (e.g. Davies et al., 2012; Schuberth et al., 2012) are not consistent with the emerging information on both radial structure and lateral heterogeneity.

A confluence of methods and observations will be necessary for disentangling the relative contributions of different processes to the formation and evolution of the Earth's interior. REM1D provides revised estimates of average properties in a heterogeneous Earth and serves as the update of the preliminary reference Earth model (PREM; Dziewoński and Anderson, 1981). Our interpretations are a synthesis of results from rapidly evolving areas of research that will afford new insights in the future. Potential micro-physical mechanisms need to be investigated that explain the bulk and shear attenuation profiles in REM1D with a spectrum of relaxation times or a superposition of energy dissipation mechanisms. Calibrations against REM1D structure and derivative properties (e.g. η_B, κ', μ/κ, σ_P) can improve the certitude and scope of interpretations. Revised core structure may be well suited for EoS studies since it removes past artifacts due to parameterization and improves the overall consistency with mineral physics. Chemical stratification and lateral heterogeneity in the mantle will amplify the uncertainties in thermodynamical properties; joint calibrations of the temperature profile (Section 4.5) and bulk chemical composition (Section 4.7) may prove inevitable in some regions. Realistic uncertainty estimates of seismological properties will be crucial for (in)validation of predictions from mineral physics and geodynamics. Geological interpretations can naturally be refined with a full three-dimensional reference Earth model (REM3D) that builds on this work. REM1D is readily extendable due to its modular construction and accounts for the effects of lateral heterogeneity on radial structure, features critical to these geophysical, geochemical and petrological applications.

Funding Statement

This work has been supported for several years first by fellowships at Columbia University and thereafter by partial support from the National Science Foundation (NSF) Grants (EAR-1315984, EAR-1345082, EAR-2341811) and Princeton University. Some of the calculations were performed using the open-source AVNI toolkit (Moulik et al., 2023, http://avni.globalseismology.org) developed with support from the Computational Infrastructure for Geodynamics (http://geodynamics.org), which is funded by the NSF Grants EAR-0949446 and EAR-1550901.

CRediT authorship contribution statement

Pritwiraj Moulik: Conceptualization, Methodology, Data curation, Software, Formal analysis, Visualization, Writing – original draft,

Writing – review & editing. **Göran Ekström:** Writing – review & editing, Supervision.

Declaration of competing interest

The authors declare that they have no known competing financial interests or personal relationships that could have appeared to influence the work reported in this paper.

Acknowledgments

We thank the broader geoscience community for contributing to this project (Moulik and The 3D Reference Earth Model (REM3D) Consortium, 2022, http://rem3d.org).

Appendix A. Supplementary data

Supplementary data to this article can be found online at https://doi.org/10.1016/j.pepi.2025.107320.

Data availability

The reference dataset (see Paper I), REM1D model and codes to evaluate physical parameters at arbitrary locations are available from the project webpage (http://rem3d.org) and are permanently archived on Zenodo (https://doi.org/10.5281/zenodo.8407693).

References

Abers, G.A., Fischer, K.M., Hirth, G., Wiens, D.A., Plank, T., Holtzman, B.K., McCarthy, C., Gazel, E., 2014. Reconciling mantle attenuation-temperature relationships from seismology, petrology, and laboratory measurements. Geochem. Geophys. Geosyst. 15 (9), 3521–3542. https://doi.org/10.1002/2014gc005444.

Afonso, J., Fullea, J., Yang, Y., Connolly, J., Jones, A., 2013. 3-D multi-observable probabilistic inversion for the compositional and thermal structure of the lithosphere and upper mantle. II: general methodology and resolution analysis. J. Geophys. Res. Solid Earth 118 (4), 1650–1676. https://doi.org/10.1002/jgrb.50123.

Aizawa, Y., Barnhoorn, A., Faul, U.H., Gerald, J.D.F., Jackson, I., Kovács, I., 2008. Seismic properties of Anita Bay Dunite: an exploratory study of the influence of water. J. Petrol. 49 (4), 841–855. https://doi.org/10.1093/petrology/egn007.

Akaogi, M., Ito, E., Navrotsky, A., 1989. Olivine-modified spinel-spinel transitions in the system Mg2SiO4-Fe2SiO4: calorimetric measurements, thermochemical calculation, and geophysical application. J. Geophys. Res. Solid Earth 94 (B11), 15671–15685. https://doi.org/10.1029/jb094ib11p15671.

Alexandrakis, C., Eaton, D.W., 2010. Precise seismic-wave velocity atop Earth's core: no evidence for outer-core stratification. Phys. Earth Planet. Inter. 180 (1–2), 59–65. https://doi.org/10.1016/j.pepi.2010.02.011.

Anderson, D.L., 1980. Bulk attenuation in the earth and viscosity of the core. Nature 285 (5762), 204–207. https://doi.org/10.1038/285204a0.

Anderson, O.L., 1982. The Earth's core and the phase diagram of iron. Philosophical transactions of the Royal Society of London. Series A, Mathemat. Phys. Sci. 306 (1492), 21–35. https://doi.org/10.1098/rsta.1982.0063.

Anderson, D.L., Given, J.W., 1982. Absorption band Q model for the earth. J. Geophys. Res. 87, 3893–3904.

Anderson, D.L., Hart, R., 1978. Q of the earth. J. Geophys. Res. 83, 5869–5882.

Anderson, O.L., Schreiber, E., Liebermann, R.C., Soga, N., 1968. Some elastic constant data on minerals relevant to geophysics. Rev. Geophys. 6 (4), 491–524. https://doi.org/10.1029/rg006i004p00491.

Antolik, M., Ekström, G., Dziewonski, A., 2001. Global event location with full and sparse data sets using three-dimensional models of mantle P-wave velocity. Pure Appl. Geophys. 158 (1), 291–317. https://doi.org/10.1007/pl00001161.

Backus, G.E., 1962. Long-wave elastic anisotropy produced by horizontal layering. J. Geophys. Res. 67 (11), 4427–4440. https://doi.org/10.1029/jz067i011p04427.

Backus, G.E., 1965. Possible forms of seismic anisotropy of the uppermost mantle under oceans. J. Geophys. Res. 70 (14), 3429–3439. https://doi.org/10.1029/jz070i014p03429.

Badro, J., 2014. Spin transitions in mantle minerals. Annu. Rev. Earth Planet. Sci. 42 (1), 231–248. https://doi.org/10.1146/annurev-earth-042711-105304.

Badro, J., Fiquet, G., Guyot, F., Rueff, J.-P., Struzhkin, V.V., Vankoo, G., Monaco, G., 2003. Iron partitioning in Earth's mantle: toward a deep lower mantle discontinuity. Science 300 (5620), 789–791. https://doi.org/10.1126/science.1081311.

Ballmer, M.D., Houser, C., Hernlund, J.W., Wentzcovitch, R.M., Hirose, K., 2017. Persistence of strong silica-enriched domains in the Earth's lower mantle. Nat. Geosci. 10 (3), 236–240. https://doi.org/10.1038/ngeo2898.

Bass, J.D., Anderson, D.L., 1984. Composition of the upper mantle: geophysical tests of two petrological models. Wiley Online Library 11 (3), 237–240.

Bassin, C., Laske, G., Masters, G., 2000. The current limits of resolution for surface wave tomography in North America. Eos. Trans. AGU 81 (48) (Fall Meet. Suppl.–03).

Becker, T.W., Kustowski, B., Ekström, G., 2008. Radial seismic anisotropy as a constraint for upper mantle rheology. Earth Planet. Sci. Lett. 267, 213–227.

Becker, T.W., Conrad, C.P., Buffett, B., Müller, R.D., 2009. Past and present seafloor age distributions and the temporal evolution of plate tectonic heat transport. Earth Planet. Sci. Lett. 278 (3–4), 233–242. https://doi.org/10.1016/j.epsl.2008.12.007.

Becker, T.W., Conrad, C.P., Schaeffer, A.J., Lebedev, S., 2014. Origin of azimuthal seismic anisotropy in oceanic plates and mantle. Earth Planet. Sci. Lett. 401, 236–250. https://doi.org/10.1016/j.epsl.2014.06.014.

Beghein, C., Trampert, J., Heijst, H.J.V., 2006. Radial anisotropy in seismic reference models of the mantle. J. Geophys. Res. 111 (B2), B02303. https://doi.org/10.1029/2005jb003728.

Beghein, C., Yuan, K., Schmerr, N., Xing, Z., 2014. Changes in seismic anisotropy shed light on the nature of the Gutenberg discontinuity. Science 343 (6176), 1237–1240. https://doi.org/10.1126/science.1246724.

Berryman, J.G., 1979. Long-wave elastic anisotropy in transversely isotropic media. Geophysics 44 (5), 896–917. https://doi.org/10.1190/1.1440984.

Birch, F., 1947. Finite elastic strain of cubic crystals. Phys. Rev. 71 (11), 809–824. https://doi.org/10.1103/physrev.71.809.

Birch, F., 1952. Elasticity and constitution of the Earth's interior. J. Geophys. Res. Solid Earth 57 (2), 227–286. https://doi.org/10.1029/jz057i002p00227.

Birch, F., 1964. Density and composition of mantle and core. J. Geophys. Res. Solid Earth 69 (20), 4377–4388. https://doi.org/10.1029/jz069i020p04377.

Bolt, B.A., Qamar, A., 1970. Upper bound to the density jump at the boundary of the Earth's inner Core. Nature 228 (5267), 148–150. https://doi.org/10.1038/228148a0.

Boujibar, A., Driscoll, P., Fei, Y., 2020. Super-earth internal structures and initial thermal states. Journal of Geophysical Research: Planets 125 (5). https://doi.org/10.1029/2019je006124.

Boyet, M., Carlson, R.W., 2005. ^{142}Nd evidence for early (>4.53 Ga) global differentiation of the silicate earth. Science 309 (5734), 576–581. https://doi.org/10.1126/science.1113634.

Bozdağ, E., Peter, D., Lefebvre, M., Komatitsch, D., Tromp, J., Hill, J., Podhorszki, N., Pugmire, D., 2016. Global adjoint tomography: first-generation model. Geophys. J. Int. 207 (3), 1739–1766. https://doi.org/10.1093/gji/ggw356.

Braginsky, S., 1963. Structure of the F layer and reasons for convection in the Earth's core. Dokl. Akad. Nauk. SSSR Engl. Trans. 149, 1311–1314.

Brown, J.M., Shankland, T.J., 1981. Thermodynamic parameters in the earth as determined from seismic profiles. Geophys. J. R. Astron. Soc. 66 (3), 579–596. https://doi.org/10.1111/j.1365-246x.1981.tb04891.x.

Buchbinder, G.G.R., 1968. Properties of the core-mantle boundary and observations of PcP. J. Geophys. Res. Solid Earth 73 (18), 5901–5923. https://doi.org/10.1029/jb073i018p05901.

Budiansky, B., Sumner, E.E., O'Connell, R.J., 1983. Bulk thermoelastic attenuation of composite materials. J. Geophys. Res. Solid Earth 88 (B12), 10343–10348. https://doi.org/10.1029/jb088ib12p10343.

Buffett, B.A., Seagle, C.T., 2010. Stratification of the top of the core due to chemical interactions with the mantle. Journal of geophysical research: solid. Earth 115 (B4). https://doi.org/10.1029/2009jb006751.

Buffett, B.A., Garnero, E.J., Jeanloz, R., 2000. Sediments at the top of Earth's Core. Science 290 (5495), 1338–1342. https://doi.org/10.1126/science.290.5495.1338.

Bullen, K.E., 1949. Compressibility-pressure hypothesis and the Earth's interior. Geophys. Supplem. Monthly Notices Royal Astronom. Society 5 (9), 335–368. https://doi.org/10.1111/j.1365-246x.1949.tb02952.x.

Bullen, K., 1963. An index of degree of chemical inhomogeneity in the earth. Geophys. J. R. Astron. Soc. 7 (5), 584–592.

Bullen, K.E., 1967. Note on the coefficient η. Geophys. J. R. Astron. Soc. 13 (4), 459. https://doi.org/10.1111/j.1365-246x.1967.tb03144.x.

Bunge, H., Ricard, Y., Matas, J., 2001. Non-adiabaticity in mantle convection. Geophys. Res. Lett. 28 (5), 879–882. https://doi.org/10.1029/2000gl011864.

Burakovsky, L., Preston, D.L., Wang, Y., 2004. Cold shear modulus and Grüneisen parameter at all densities. Solid State Commun. 132 (3–4), 151–156. https://doi.org/10.1016/j.ssc.2004.07.066.

Cammarano, F., Deuss, A., Goes, S., Giardini, D., 2005. One-dimensional physical reference models for the upper mantle and transition zone: combining seismic and mineral physics constraints. J. Geophys. Res. Solid Earth 110, B01306. https://doi.org/10.1029/2004jb003272.

Cammarano, F., Romanowicz, B., Stixrude, L., Lithgow-Bertelloni, C., Xu, W., 2009. Inferring the thermochemical structure of the upper mantle from seismic data. Geophys. J. Int. 179 (2), 1169–1185. https://doi.org/10.1111/j.1365-246x.2009.04338.x.

Caracas, R., Mainprice, D., Thomas, C., 2010. Is the spin transition in Fe2+−bearing perovskite visible in seismology? Geophys. Res. Lett. 37 (13). https://doi.org/10.1029/2010gl043320.

Carcione, J.M., 2000. A model for seismic velocity and attenuation in petroleum source rocks. Geophysics 65 (4), 1080–1092.

Catalli, K., Shim, S.-H., Prakapenka, V., 2009. Thickness and Clapeyron slope of the post-perovskite boundary. Nature 462, 782–785. https://doi.org/10.1038/nature08598.

Chang, S.-J., Ferreira, A.M.G., Ritsema, J., Heijst, H.J., Woodhouse, J.H., 2015. Joint inversion for global isotropic and radially anisotropic mantle structure including crustal thickness perturbations. J. Geophys. Res. 120 (6), 4278–4300. https://doi.org/10.1002/2014jb011824.

Chapman, M., 2003. Frequency-dependent anisotropy due to meso-scale fractures in the presence of equant porosity. Geophys. Prospect. 51 (5), 369–379.

Chen, M., Tromp, J., 2007. Theoretical and numerical investigations of global and regional seismic wave propagation in weakly anisotropic earth models. Geophys. J. Int. 168 (3), 1130–1152. https://doi.org/10.1111/j.1365-246x.2006.03218.x.
Chopelas, A., Boehler, R., 1992. Thermal expansivity in the lower mantle. Geophys. Res. Lett. 19 (19), 1983–1986. https://doi.org/10.1029/92gl02144.
Christensen, U.R., Hofmann, A.W., 1994. Segregation of subducted oceanic crust in the convecting mantle. J. Geophys. Res. 99, 19867–19884. https://doi.org/10.1029/93jb03403.
Christensen, U.R., Yuen, D.A., 1985. Layered convection induced by phase transitions. J. Geophys. Res. Solid Earth 90 (B12), 10291–10300. https://doi.org/10.1029/jb090ib12p10291.
Cleary, J., 1969. The S velocity at the core-mantle boundary, from observations of diffracted S. Bull. Seismol. Soc. Am. 59 (3), 1399–1405. https://doi.org/10.1111/gji.1938.4.issue-5.
Cobden, L., Goes, S., Ravenna, M., Styles, E., Cammarano, F., Gallagher, K., Connolly, J. A.D., 2009. Thermochemical interpretation of 1-D seismic data for the lower mantle: the significance of nonadiabatic thermal gradients and compositional heterogeneity. J. Geophys. Res. Solid Earth 114 (B11). https://doi.org/10.1029/2008jb006262.
Conrad, C.P., Behn, M.D., 2010. Constraints on lithosphere net rotation and asthenospheric viscosity from global mantle flow models and seismic anisotropy. Geochem. Geophys. Geosyst. 11 (5), Q05W05. https://doi.org/10.1029/2009gc002970.
Cottaar, S., Romanowicz, B., 2012. An unusually large ULVZ at the base of the mantle near Hawaii. Earth Planet. Sci. Lett. 355-356, 213–222. https://doi.org/10.1016/j.epsl.2012.09.005.
Courtier, A.M., Jackson, M.G., Lawrence, J.F., Wang, Z., Lee, C.-T.A., Halama, R., Warren, J.M., Workman, R., Xu, W., Hirschmann, M.M., Larson, A.M., Hart, S.R., Lithgow-Bertelloni, C., Stixrude, L., Chen, W.-P., 2007. Correlation of seismic and petrologic thermometers suggests deep thermal anomalies beneath hotspots. Earth Planet. Sci. Lett. 264 (1), 308–316.
Crowley, J.W., Gérault, M., O'Connell, R.J., 2011. On the relative influence of heat and water transport on planetary dynamics. Earth Planet. Sci. Lett. 310, 380–388. https://doi.org/10.1016/j.epsl.2011.08.035.
Dahlen, F.A., 1982. The effect of data windows on the estimation of free oscillation parameters. Geophys. J. Int. 69 (2), 537–549. https://doi.org/10.1111/j.1365-246X.1982.tb04964.x.
Dahlen, F.A., Tromp, J., 1998. Theoretical Global Seismology. Princeton Univ Press, Princeton Univ Press.
Dalton, C.A., Ekström, G., Dziewonski, A.M., 2008. The global attenuation structure of the upper mantle. J. Geophys. Res. 113, B09303. https://doi.org/10.1029/2007jb005429.
Dannberg, J., Eilon, Z., Faul, U., Gassmöller, R., Moulik, P., Myhill, R., 2017. The importance of grain size to mantle dynamics and seismological observations. Geochem. Geophys. Geosyst. 18 (8), 3034–3061. https://doi.org/10.1002/2017gc006944.
Davies, D.R., Goes, S., Davies, J.H., Schuberth, B.S.A., Bunge, H.P., Ritsema, J., 2012. Reconciling dynamic and seismic models of Earth's lower mantle: the dominant role of thermal heterogeneity. Earth Planet. Sci. Lett. 353-354, 253–269. https://doi.org/10.1016/j.epsl.2012.08.016.
Davies, C., Pozzo, M., Gubbins, D., Alfè, D., 2015. Constraints from material properties on the dynamics and evolution of Earth's core. Nat. Geosci. 8 (9), 678–685. https://doi.org/10.1038/ngeo2492.
Debayle, E., Ricard, Y., 2013. Seismic observations of large-scale deformation at the bottom of fast-moving plates. Earth Planet. Sci. Lett. 376, 165–177. https://doi.org/10.1016/j.epsl.2013.06.025.
Deschamps, F., Trampert, J., 2004. Towards a lower mantle reference temperature and composition. Earth Planet. Sci. Lett. 222 (1), 161–175. https://doi.org/10.1016/j.epsl.2004.02.024.
Deuss, A., 2009. Global observations of mantle discontinuities using SS and PP precursors. Surv. Geophys. 30 (4–5), 301–326. https://doi.org/10.1007/s10712-009-9078-y.
Deuss, A., Redfern, S.A.T., Chambers, K., Woodhouse, J.H., 2006. The nature of the 660-kilometer discontinuity in Earth's mantle from global seismic observations of PP precursors. Science 311 (5758), 198–201. https://doi.org/10.1126/science.1120020.
Deuss, A., Ritsema, J., van Heijst, H., 2013. A new catalogue of normal-mode splitting function measurements up to 10 mHz. Geophys. J. Int. 193, 920–937. https://doi.org/10.1093/gji/ggt010.
Dohmen, R., Milke, R., 2010. Diffusion in polycrystalline materials: grain boundaries, mathematical models, and experimental data. Rev. Mineral. Geochem. 72 (1), 921–970. https://doi.org/10.2138/rmg.2010.72.21.
Doornbos, D.J., 1974. The Anelasticity of the inner Core. Geophys. J. Int. 38 (2), 397–415. https://doi.org/10.1111/j.1365-246x.1974.tb04131.x.
Duffy, T.S., Ahrens, T.J., 1993. Thermal expansion of mantle and core materials at very high pressures. Geophys. Res. Lett. 20 (11), 1103–1106. https://doi.org/10.1029/93gl00479.
Duffy, T., Madhusudhan, N., Lee, K., 2005. Mineralogy of super-earth planets. In: Treatise on Geophysics, Second edition vol. 2. Elsevier, pp. 149–178.
Durand, S., Chambat, F., Matas, J., Ricard, Y., 2012. Constraining the kinetics of mantle phase changes with seismic data. Geophys. J. Int. 189 (3), 1557–1564. https://doi.org/10.1111/j.1365-246x.2012.05417.x.
Durand, S., Matas, J., Ford, S., Ricard, Y., Romanowicz, B., Montagner, J., 2013. Insights from ScS–S measurements on deep mantle attenuation. Earth Planet. Sci. Lett. 374, 101–110. https://doi.org/10.1016/j.epsl.2013.05.026.
Durek, J.J., Ekström, G., 1995. Evidence of bulk attenuation in the asthenosphere from recordings of the Bolivia earthquake. Geophys. Res. Lett. 22 (16), 2309–2312. https://doi.org/10.1029/95gl01434.
Durek, J., Ekström, G., 1996. A radial model of anelasticity consistent with long-period surface-wave attenuation. Bull. Seismol. Soc. Am. 86 (1A), 144–158.
Dziewoński, A.M., Anderson, D.L., 1981. Preliminary reference earth model. Phys. Earth Planet. Inter. 25, 297–356.
Ekström, G., 2011. A global model of Love and Rayleigh surface wave dispersion and anisotropy, 25–250 s. Geophys. J. Int. 187, 1668–1686.
Estabrook, C.H., Kind, R., 1996. The nature of the 660-kilometer upper-mantle seismic discontinuity from precursors to the PP phase. Science 274 (5290), 1179–1182. https://doi.org/10.1126/science.274.5290.1179.
Faccenda, M., Burlini, L., Gerya, T.V., Mainprice, D., 2008. Fault-induced seismic anisotropy by hydration in subducting oceanic plates. Nature 455, 1097–1100. https://doi.org/10.1038/nature07376.
Falzone, A.J., Stacey, F.D., 1980. Second-order elasticity theory: explanation for the high poisson's ratio of the inner core. Phys. Earth Planet. Inter. 21 (4), 371–377. https://doi.org/10.1016/0031-9201(80)90140-5.
Farnetani, C.G., 1997. Excess temperature of mantle plumes: the role of chemical stratification across D″. Geophys. Res. Lett. 24, 1583–1586. https://doi.org/10.1029/97gl01548.
Farra, V., 2005. First-order ray tracing for qS waves in inhomogeneous weakly anisotropic media. Geophys. J. Int. 161 (2), 309–324. https://doi.org/10.1111/j.1365-246x.2005.02570.x.
Faul, U.H., Jackson, I., 2005. The seismological signature of temperature and grain size variations in the upper mantle. Earth Planet. Sci. Lett. 234, 119–134.
Faul, U., Jackson, I., 2015. Transient creep and strain energy dissipation: an experimental perspective. Annu. Rev. Earth Planet. Sci. 43 (1), 541–569. https://doi.org/10.1146/annurev-earth-060313-054732.
Fischer-Gödde, M., Elfers, B.-M., Münker, C., Szilas, K., Maier, W.D., Messling, N., Morishita, T., Kranendonk, M.V., Smithies, H., 2020. Ruthenium isotope vestige of Earth's pre-late-veneer mantle preserved in Archaean rocks. Nature 579 (7798), 240–244. https://doi.org/10.1038/s41586-020-2069-3.
Forsyth, D.W., 1975. The early structural evolution and anisotropy of the oceanic upper mantle. Geophys. J. Int. 43 (1), 103–162. https://doi.org/10.1111/j.1365-246x.1975.tb00630.x.
French, S.W., Romanowicz, B.A., 2014. Whole-mantle radially anisotropic shear velocity structure from spectral-element waveform tomography. Geophys. J. Int. 199, 1303–1327. https://doi.org/10.1093/gji/ggu334.
Frost, D.A., Avery, M.S., Buffett, B.A., Chidester, B.A., Deng, J., Dorfman, S.M., Li, Z., Liu, L., Lv, M., Martin, J.F., 2022. Multidisciplinary constraints on the thermal-chemical boundary between Earth's Core and mantle. Geochem. Geophys. Geosyst. 23 (3), e2021GC009764. https://doi.org/10.1029/2021gc009764.
Fu, S., Yang, J., Zhang, Y., Okuchi, T., McCammon, C., Kim, H., Lee, S.K., Lin, J., 2018. Abnormal elasticity of Fe-bearing Bridgmanite in the Earth's lower mantle. Geophys. Res. Lett. 45 (10), 4725–4732. https://doi.org/10.1029/2018gl077764.
Fuji, N., Kawai, K., Geller, R.J., 2010. A methodology for inversion of broadband seismic waveforms for elastic and anelastic structure and its application to the mantle transition zone beneath the northwestern Pacific. Phys. Earth Planet. Inter. 180 (3–4), 118–137. https://doi.org/10.1016/j.pepi.2009.10.004.
Fukao, Y., Obayashi, M., 2013. Subducted slabs stagnant above, penetrating through, and trapped below the 660 km discontinuity. J. Geophys. Res. Solid Earth 118 (11), 5920–5938. https://doi.org/10.1002/2013jb010466.
Fukao, Y., Widiyantoro, S., Obayashi, M., 2001. Stagnant slabs in the upper and lower mantle transition region. Rev. Geophys. 39 (3), 291–323. https://doi.org/10.1029/1999rg000068.
Gaherty, J.B., 2004. A surface wave analysis of seismic anisotropy beneath eastern North America. Geophys. J. Int. 158 (3), 1053–1066. https://doi.org/10.1111/j.1365-246x.2004.02371.x.
Gaherty, J.B., Jordan, T., 1995. Lehmann discontinuity as the base of an anisotropic layer beneath continents. Science 268 (5216), 1468–1471. https://doi.org/10.1126/science.268.5216.1468.
Gaherty, J.B., Kato, M., Jordan, T.H., 1999a. Seismological structure of the upper mantle: a regional comparison of seismic layering. Phys. Earth Planet. Inter. 110 (1–2), 21–41. https://doi.org/10.1016/s0031-9201(98)00132-0.
Gaherty, J.B., Wang, Y., Jordan, T.H., Weidner, D.J., 1999b. Testing plausible upper-mantle compositions using fine-scale models of the 410-km discontinuity. Geophys. Res. Lett. 26 (11), 1641–1644. https://doi.org/10.1029/1999gl900312.
Gasparik, T., 1990. Phase relations in the transition zone. J. Geophys. Res. Solid Earth 95 (B10), 15751–15769. https://doi.org/10.1029/jb095ib10p15751.
Giardini, D., Li, X.-D., Woodhouse, J.H., 1987. Three-dimensional structure of the earth from splitting in free-oscillation spectra. Nature 325, 405–411. https://doi.org/10.1038/325405a0.
Giardini, D., Li, X.-D., Woodhouse, J.H., 1988. Splitting functions of long-period Normal modes of the earth. J. Geophys. Res. 93 (B11), 13716–13742. https://doi.org/10.1029/jb093ib11p13716.
Grand, S.P., van der Hilst, R.D., Widiyantoro, S., 1997. Global seismic tomography: A snapshot of convection in the earth. GSA Today 7 (4), 1–7.
Green, D.H., Ringwood, A.E., 1967. The genesis of basaltic magmas. Contrib. Mineral. Petrol. 15 (2), 103–190. https://doi.org/10.1007/bf00372052.
Greve, S.M., Savage, M.K., 2009. Modelling seismic anisotropy variations across the Hikurangi subduction margin, New Zealand. Earth Planet. Sci. Lett. 285, 16–26. https://doi.org/10.1016/j.epsl.2009.05.035.
Gribb, T.T., Cooper, R.F., 1998. Low-frequency shear attenuation in polycrystalline olivine: grain boundary diffusion and the physical significance of the Andrade model

for viscoelastic rheology. J. Geophys. Res. Solid Earth 103 (B11), 27267–27279. https://doi.org/10.1029/98jb02786.
Grocholski, B., Catalli, K., Shim, S.-H., Prakapenka, V., 2012. Mineralogical effects on the detectability of the postperovskite boundary. Proc. Natl. Acad. Sci. 109, 2275–2279. https://doi.org/10.1073/pnas.1109204109.
Grüneisen, E., 1912. Theorie des festen zustandes einatomiger elemente. Ann. Phys. 344 (12), 257–306. https://doi.org/10.1002/andp.19123441202.
Gu, Y.J., Dziewonski, A.M., Agee, C.B., 1998. Global de-correlation of the topography of transition zone discontinuities. Earth Planet. Sci. Lett. 157 (1–2), 57–67. https://doi.org/10.1016/s0012-821x(98)00027-2.
Gu, Y.J., Dziewoński, A.M., Ekström, G., 2003. Simultaneous inversion for mantle shear velocity and topography of transition zone discontinuities. Geophys. J. Int. 154, 559–583.
Gubbins, D., Masters, G., Nimmo, F., 2008. A thermochemical boundary layer at the base of Earth's outer core and independent estimate of core heat flux. Geophys. J. Int. 174 (3), 1007–1018. https://doi.org/10.1111/j.1365-246x.2008.03879.x.
Gülcher, A.J., Gebhardt, D.J., Ballmer, M.D., Tackley, P.J., 2020. Variable dynamic styles of primordial heterogeneity preservation in the Earth's lower mantle. Earth Planet. Sci. Lett. 536, 116160. https://doi.org/10.1016/j.epsl.2020.116160.
Häfner, R., Widmer-Schnidrig, R., 2013. Signature of 3-D density structure in spectra of the spheroidal free oscillation ${}_0S_2$. Geophys. J. Int. 192, 285–294. https://doi.org/10.1093/gji/ggs013.
Hager, B., Clayton, R., Richards, M., Comer, R., 1985. Lower mantle heterogeneity, dynamic topography and the geoid. Nature 313, 541–545.
Hansen, U., Yuen, D.A., 1988. Numerical simulations of thermal-chemical instabilities at the core–mantle boundary. Nature 334, 237–240. https://doi.org/10.1038/334237a0.
Hart, S.R., Zindler, A., 1986. In search of a bulk-earth composition. Chem. Geol. 57 (3–4), 247–267. https://doi.org/10.1016/0009-2541(86)90053-7.
Hart, R.S., Anderson, D.L., Kanamori, H., 1977. The effect of attenuation on gross earth models. J. Geophys. Res. Solid Earth 82 (11), 1647–1654. https://doi.org/10.1029/jb082i011p01647.
Heinz, D.L., Jeanloz, R., 1983. Inhomogeneity parameter of a homogeneous earth. Nature 301 (5896), 138–139. https://doi.org/10.1038/301138a0.
Heinz, D., Jeanloz, R., O'Connell, R.J., 1982. Bulk attenuation in a polycrystalline earth. J. Geophys. Res. Solid Earth 87 (B9), 7772–7778. https://doi.org/10.1029/jb087ib09p07772.
Helffrich, G., Kaneshima, S., 2010. Outer-core compositional stratification from observed core wave speed profiles. Nature 468 (7325), 807–810. https://doi.org/10.1038/nature09636.
Herzberg, C., Asimow, P.D., Arndt, N., Niu, Y., Lesher, C., Fitton, J., Cheadle, M., Saunders, A., 2007. Temperatures in ambient mantle and plumes: constraints from basalts, picrites, and komatiites. Geochem. Geophys. Geosyst. 8 (2).
Hirose, K., Labrosse, S., Hernlund, J., 2013. Composition and state of the Core. Annu. Rev. Earth Planet. Sci. 41, 657–691. https://doi.org/10.1146/annurev-earth-050212-124007.
Hirose, K., Wood, B., Vočadlo, L., 2021. Light elements in the Earth's core. Nat. Rev. Earth & Environ. 2 (9), 645–658. https://doi.org/10.1038/s43017-021-00203-6.
Hirschmann, M.M., 2006. Water, melting and the deep earth H_2O cycle. Annu. Rev. Earth Planet. Sci. 34 (1), 629–653. https://doi.org/10.1146/annurev.earth.34.031405.125211.
Hirth, G., Kohlstedt, D.L., 1996. Water in the oceanic upper mantle: implications for rheology, melt extraction and the evolution of the lithosphere. Earth Planet. Sci. Lett. 144, 93–108. https://doi.org/10.1016/0012-821x(96)00154-9.
Hofmann, A.W., 1997. Mantle geochemistry: the message from oceanic volcanism. Nature 385, 219–229. https://doi.org/10.1038/385219a0.
Hofmann, A.W., 2003. Sampling mantle heterogeneity through oceanic basalts: Isotopes and trace elements. In: Carlson, R.W., Holland, H.D., Turekian, K.K. (Eds.), Treatise on Geochemistry: The Mantle and Core. Elsevier, New York, pp. 61–91.
Hofmann, A.W., White, W.M., 1982. Mantle plumes from ancient oceanic crust. Earth Planet. Sci. Lett. 57 (2), 421–436. https://doi.org/10.1016/0012-821x(82)90161-3.
Holtzman, B.K., Kendall, J.M., 2010. Organized melt, seismic anisotropy, and plate boundary lubrication. Geochem. Geophys. Geosyst. 11, Q0AB06. https://doi.org/10.1029/2010gc003296.
Holtzman, B.K., Kohlstedt, D.L., Zimmerman, M.E., 2003. Melt segregation and strain partitioning: implications for seismic anisotropy and mantle flow. Science 301, 1227–1230. https://doi.org/10.1126/science.1087132.
Houser, C., 2007. Constraints on the presence or absence of post-perovskite in the lowermost mantle from long-period seismology. In: Post-Perovskite: The Last Mantle Phase Transition. American Geophysical Union (AGU), pp. 191–216. https://doi.org/10.1029/174GM14.
Houser, C., Hernlund, J., Valencia-Cardona, J., Wentzcovitch, R., 2020. Discriminating lower mantle composition. Phys. Earth Planet. Inter. 308, 106552. https://doi.org/10.1016/j.pepi.2020.106552.
Hwang, Y.K., Ritsema, J., 2011. Radial Q structure of the lower mantle from teleseismic body-wave spectra. Earth Planet. Sci. Lett. 303 (3–4), 369–375. https://doi.org/10.1016/j.epsl.2011.01.023.
Irifune, T., Shinmei, T., McCammon, C.A., Miyajima, N., Rubie, D.C., Frost, D.J., 2010. Iron partitioning and density changes of Pyrolite in Earth's lower mantle. Science 327 (5962), 193–195. https://doi.org/10.1126/science.1181443.
Irving, J.C.E., Cottaar, S., Lekic, V., 2018. Seismically determined elastic parameters for Earth's outer core. Sci. Adv. 4 (6), eaar2538. https://doi.org/10.1126/sciadv.aar2538.
Ishii, M., Tromp, J., 1999. Normal-mode and free-air gravity constraints on lateral variations in velocity and density of Earth's mantle. Science 285, 1231–1236.
Ita, J., Stixrude, L., 1992. Petrology, elasticity, and composition of the mantle transition zone. J. Geophys. Res. Solid Earth 97 (B5), 6849–6866. https://doi.org/10.1029/92jb00068.
Jackson, I., 1983. Some geophysical constraints on the chemical composition of the earth's lower mantle. Earth Planet. Sci. Lett. 62 (1), 91–103. https://doi.org/10.1016/0012-821x(83)90073-0.
Jackson, I., Faul, U.H., 2010. Grainsize-sensitive viscoelastic relaxation in olivine: towards a robust laboratory-based model for seismological application. Phys. Earth Planet. Inter. 183 (1), 151–163.
Jackson, I., Rigden, S.M., 1996. Analysis of P-V-T data: constraints on the thermoelastic properties of high-pressure minerals. Phys. Earth Planet. Inter. 96 (2–3), 85–112. https://doi.org/10.1016/0031-9201(96)03143-3.
Jackson, I., Gerald, J.D.F., Faul, U.H., Tan, B.H., 2002. Grain-size-sensitive seismic wave attenuation in polycrystalline olivine. J. Geophys. Res. Solid Earth 107 (B12), 2360. https://doi.org/10.1029/2001jb001225.
Jackson, M.G., Carlson, R.W., Kurz, M.D., Kempton, P.D., Francis, D., Blusztajn, J., 2010. Evidence for the survival of the oldest terrestrial mantle reservoir. Nature 466 (7308), 853–856. https://doi.org/10.1038/nature09287.
Jackson, I., Faul, U.H., Skelton, R., 2014. Elastically accommodated grain-boundary sliding: new insights from experiment and modeling. Phys. Earth Planet. Inter. 228, 203–210. https://doi.org/10.1016/j.pepi.2013.11.014.
Jarvis, G.T., Mckenzie, D.P., 2006. Convection in a compressible fluid with infinite Prandtl number. J. Fluid Mech. 96 (3), 515–583. https://doi.org/10.1017/s002211208000225x.
Jaupart, C., Labrosse, S., Mareschal, J.C., 2007. Temperatures, heat and energy in the mantle of the earth. In: Schubert, G. (Ed.), Treatise on Geophysics, vol. 7. Elsevier, pp. 253–303. https://doi.org/10.1016/B978-044452748-6.00114-0.
Jeanloz, R., Knittle, E., 1989. Density and composition of the lower mantle. Philosophical transactions for the Royal Society of London. Series A, Mathemat. Phys. Sci. 328, 377–389. https://doi.org/10.1098/rsta.1989.0042.
Jeanloz, R., Morris, S., 1987. Is the mantle geotherm subadiabatic? Geophys. Res. Lett. 14 (4), 335–338. https://doi.org/10.1029/gl014i004p00335.
Jeanloz, R., Richter, F.M., 1979. Convection, composition, and the thermal state of the lower mantle. J. Geophys. Res. Solid Earth 84 (B10), 5497–5504. https://doi.org/10.1029/jb084ib10p05497.
Jech, J., Pšenčík, I., 1989. First-order perturbation method for anisotropic media. Geophys. J. Int. 99 (2), 369–376. https://doi.org/10.1111/j.1365-246x.1989.tb01694.x.
Jephcoat, A., Olson, P., 1987. Is the inner core of the earth pure iron? Nature 325 (6102), 332–335. https://doi.org/10.1038/325332a0.pdf.
Jung, H., Karato, S.-I., 2001. Water-induced fabric transitions in olivine. Science 293, 1460–1463. https://doi.org/10.1126/science.1062235.
Kanamori, H., Anderson, D.L., 1977. Importance of physical dispersion in surface-wave and free oscillation problems. Rev. Geophys. 15 (1), 105–112. https://doi.org/10.1029/rg015i001p00105.
Kaneshima, S., 2018. Array analyses of SmKS waves and the stratification of Earth's outermost core. Phys. Earth Planet. Inter. 276, 234–246. https://doi.org/10.1016/j.pepi.2017.03.006.
Kaneshima, S., Helffrich, G., 2013. Vp structure of the outermost core derived from analysing large-scale array data of SmKS waves. Geophys. J. Int. 193 (3), 1537–1555. https://doi.org/10.1093/gji/ggt042.
Karato, S.-I., 1992. On the Lehmann discontinuity. Geophys. Res. Lett. 19 (22), 2255–2258. https://doi.org/10.1029/92gl02603.
Karato, S.-I., 1998. Seismic anisotropy in the deep mantle, boundary layers and the geometry of mantle convection. Pure Appl. Geophys. 151 (2), 565–587. https://doi.org/10.1007/s000240050130.
Karato, S.-I., 2011. Water distribution across the mantle transition zone and its implications for global material circulation. Earth Planet. Sci. Lett. 301 (3–4), 413–423. https://doi.org/10.1016/j.epsl.2010.11.038.
Karato, S.-I., Jung, H., 1998. Water, partial melting and the origin of the seismic low velocity and high attenuation zone in the upper mantle. Earth Planet. Sci. Lett. 157 (3–4), 193–207. https://doi.org/10.1016/s0012-821x(98)00034-x.
Karato, S.-I., Karki, B.B., 2001. Origin of lateral variation of seismic wave velocities and density in the deep mantle. J. Geophys. Res. Solid Earth 106, 21771–21783. https://doi.org/10.1029/2001jb000214.
Karato, S.-I., Jung, H., Katayama, I., Skemer, P., 2008. Geodynamic significance of seismic anisotropy of the upper mantle: new insights from laboratory studies. Annu. Rev. Earth Planet. Sci. 36 (1), 59–95. https://doi.org/10.1146/annurev.earth.36.031207.124120.
Kawakatsu, H., 2016. A new fifth parameter for transverse isotropy. Geophys. J. Int. 204 (1), 682–685. https://doi.org/10.1093/gji/ggv479.
Kawakatsu, H., Kumar, P., Takei, Y., Shinohara, M., Kanazawa, T., Araki, E., Suyehiro, K., 2009. Seismic evidence for sharp lithosphere-asthenosphere boundaries of oceanic plates. Science 324 (5926), 499–502. https://doi.org/10.1126/science.1169499.
Kellogg, L., Hager, B., van der Hilst, R., 1999. Compositional stratification in the deep mantle. Science 283 (5409), 1881–1884. https://doi.org/10.1126/science.283.5409.1881.
Kennett, B.L.N., 2020. Radial earth models revisited. Geophys. J. Int. 222 (3), 2189–2204. https://doi.org/10.1093/gji/ggaa298.
Kennett, B., 2021. The relative behaviour of bulk and shear modulus as an indicator of the iron spin transition in the lower mantle. Earth Planet. Sci. Lett. 559, 116808. https://doi.org/10.1016/j.epsl.2021.116808.
Kennett, B.L.N., Engdahl, E.R., Buland, R., 1995. Constraints on seismic velocities in the earth from traveltimes. Geophys. J. Int. 122, 108–124. https://doi.org/10.1111/j.1365-246x.1995.tb03540.x.

Khan, A., Connolly, J.A.D., Taylor, S.R., 2008. Inversion of seismic and geodetic data for the major element chemistry and temperature of the Earth's mantle. J. Geophys. Res. Solid Earth 113 (B9), B09308. https://doi.org/10.1029/2007jb005239.
Kiefer, B., Stixrude, L., Wentzcovitch, R.M., 1997. Calculated elastic constants and anisotropy of mg_2sio_4 spinel at high pressure. Geophys. Res. Lett. 24 (22), 2841–2844. https://doi.org/10.1029/97GL02975.
Klein, E.M., Langmuir, C.H., 1987. Global correlations of ocean ridge basalt chemistry with axial depth and crustal thickness. J. Geophys. Res. 92 (B8), 8089–8115.
Knittle, E., Jeanloz, R., 1989. Simulating the core-mantle boundary: an experimental study of high-pressure reactions between silicates and liquid iron. Geophys. Res. Lett. 16 (7), 609–612. https://doi.org/10.1029/gl016i007p00609.
Knittle, E., Jeanloz, R., 1991. Earth's Core-mantle boundary: results of experiments at high pressures and temperatures. Science 251 (5000), 1438–1443. https://doi.org/10.1126/science.251.5000.1438.
Koelemeijer, P., Deuss, A., Ritsema, J., 2013. Observations of core-mantle boundary Stoneley modes. Geophys. Res. Lett. 40, 2557–2561. https://doi.org/10.1002/grl.50514.
Koper, K.D., Dombrovskaya, M., 2005. Seismic properties of the inner core boundary from PKiKP / P amplitude ratios. Earth Planet. Sci. Lett. 237 (3–4), 680–694. https://doi.org/10.1016/j.epsl.2005.07.013.
Kraus, R.G., Hemley, R.J., Ali, S.J., Belof, J.L., Benedict, L.X., Bernier, J., Braun, D., Cohen, R.E., Collins, G.W., Coppari, F., Desjarlais, M.P., Fratanduono, D., Hamel, S., Krygier, A., Lazicki, A., Mcnaney, J., Millot, M., Myint, P.C., Newman, M.G., Rygg, J. R., Sterbentz, D.M., Stewart, S.T., Stixrude, L., Swift, D.C., Wehrenberg, C., Eggert, J. H., 2022. Measuring the melting curve of iron at super-earth core conditions. Science 375 (6577), 202–205. https://doi.org/10.1126/science.abm1472.
Kuo, C., Romanowicz, B., 2002. On the resolution of density anomalies in the Earth's mantle using spectral fitting of normal-mode data. Geophys. J. Int. 150, 162–179. https://doi.org/10.1046/j.1365-246x.2002.01698.x.
Kustowski, B., Ekström, G., Dziewonski, A.M., 2008. Anisotropic shear-wave velocity structure of the Earth's mantle: A global model. J. Geophys. Res. 113, B06306. https://doi.org/10.1029/2007jb005169.
Labrosse, S., Hernlund, J.W., Coltice, N., 2007. A crystallizing dense magma ocean at the base of the Earth's mantle. Nature 450, 866–869. https://doi.org/10.1038/nature06355.
Laio, A., Bernard, S., Chiarotti, G.L., Scandolo, S., Tosatti, E., 2000. Physics of Iron at Earth's Core conditions. Science 287 (5455), 1027–1030. https://doi.org/10.1126/science.287.5455.1027.
Laske, G., Masters, G., Ma, Z., Pasyanos, M., 2013. Update on CRUST1.0 - A 1-degree global model of Earth's CRUST. Geophys. Res. Abstr. 15, Abstract EGU2013–2658.
Lau, H.C.P., Yang, H.-Y., Tromp, J., Mitrovica, J.X., Latychev, K., Al-Attar, D., 2015. A normal mode treatment of semi-diurnal body tides on an aspherical, rotating and anelastic earth. Geophys. J. Int. 202 (2), 1392–1406. https://doi.org/10.1093/gji/ggv227.
Lau, H.C.P., Mitrovica, J.X., Davis, J.L., Tromp, J., Yang, H.-Y., Al-Attar, D., 2017. Tidal tomography constrains Earth's deep-mantle buoyancy. Nature 551 (7680), 321–326. https://doi.org/10.1038/nature24452.
Lawrence, J.F., Shearer, P.M., 2006. Constraining seismic velocity and density for the mantle transition zone with reflected and transmitted waveforms. Geochem. Geophys. Geosyst. 7 (10), Q10012. https://doi.org/10.1029/2006gc001339.
Lawrence, J.F., Wysession, M.E., 2006. QLM9: A new radial quality factor model for the lower mantle. Earth Planet. Sci. Lett. 241 (3), 962–971.
Lay, T., Young, C.J., 1990. The stably-stratified outermost core revisited. Geophys. Res. Lett. 17 (11), 2001–2004. https://doi.org/10.1029/gl017i011p02001.
Lay, T., Hernlund, J., Buffett, B.A., 2008. Core–mantle boundary heat flow. Nat. Geosci. 1 (1), 25–32. https://doi.org/10.1038/ngeo.2007.44.
Le Bars, M., Davaille, A., 2004. Whole layer convection in a heterogeneous planetary mantle. Journal of geophysical research: solid. Earth 109 (B3). https://doi.org/10.1029/2003jb002617.
Lekic, V., Matas, J., Panning, M., Romanowicz, B., 2009. Measurement and implications of frequency dependence of attenuation. Earth Planet. Sci. Lett. 282 (1–4), 285–293. https://doi.org/10.1016/j.epsl.2009.03.030.
Lessing, S., Thomas, C., Saki, M., Schmerr, N., Vanacore, E., 2015. On the difficulties of detecting PP precursors. Geophys. J. Int. 201 (3), 1666–1681. https://doi.org/10.1093/gji/ggv105.
Li, X., Giardini, D., Woodhouse, J., 1991. Large-scale three-dimensional even-degree structure of the earth from splitting of long-period normal modes. J. Geophys. Res. 96 (B1), 551–577.
Lin, P.-Y.P., Gaherty, J.B., Jin, G., Collins, J.A., Lizarralde, D., Evans, R.L., Hirth, G., 2016. High-resolution seismic constraints on flow dynamics in the oceanic asthenosphere. Nature 535 (7613), 538–541. https://doi.org/10.1038/nature18012.
Liu, L., 1979. Phase transformations and the constitution of the deep mantle. In: McElhinny, M. (Ed.), The Earth: Its Origin, Structure and Evolution. Academic, San Diego, C.A, pp. 177–202.
Liu, H.-P., Anderson, D.L., Kanamori, H., 1976. Velocity dispersion due to anelasticity; implications for seismology and mantle composition. Geophys. J. Int. 47 (1), 41–58. https://doi.org/10.1111/j.1365-246x.1976.tb01261.x.
Loper, D.E., Roberts, P.H., 1977. On the motion of an iron-alloy core containing a slurry: I. General theory. Geophys. & Astrophys. Fluid Dynam. 9 (1), 289–321. https://doi.org/10.1080/03091927708242333.
Loper, D.E., Stacey, F.D., 1983. The dynamical and thermal structure of deep mantle plumes. Chem. Geol. 33, 304–317.
Love, A., 1927. A Treatise on the Theory of Elasticity, 4th edition. Cambridge University Press, Cambridge.
Lythgoe, K.H., Deuss, A., 2015. The existence of radial anisotropy in Earth's upper inner core revealed from seismic normal mode observations. Geophys. Res. Lett. 42, 4841–4848. https://doi.org/10.1002/2015gl064326.
Ma, X., Tkalčić, H., 2021. CCREM: new reference earth model from the global coda-correlation Wavefield. J. Geophys. Res. Solid Earth 126 (9). https://doi.org/10.1029/2021jb022515.
Ma, Z., Masters, G., Laske, G., Pasyanos, M., 2014. A comprehensive dispersion model of surface wave phase and group velocity for the globe. Geophys. J. Int. 199 (1), 113–135. https://doi.org/10.1093/gji/ggu246.
Maggi, A., Debayle, E., Priestley, K., Barruol, G., 2006. Azimuthal anisotropy of the Pacific region. Earth Planet. Sci. Lett. 250, 53–71.
Mainprice, D., 2007. Seismic anisotropy of the deep earth from a mineral and rock physics perspective. In: Schubert, G. (Ed.), Treatise on Geophysics, vol. 2. Elsevier, Oxford, UK, pp. 437–492.
Mainprice, D., Barruol, G., Ben Ismail, W., 2000. The seismic anisotropy of the earth's mantle: From single crystal to polycrystal. In: Karato, S.-I., Forte, A., Liebermann, R., Masters, G., Stixrude, L. (Eds.), Earth's Deep Interior: Mineral Physics and Tomography from the Atomic to the Global Scale, Geophys. Monogr. Ser. American Geophysical Union, Washington D.C., pp. 237–264
Mao, H.-K., Shu, J., Shen, G., Hemley, R.J., Li, B., Singh, A.K., 1998. Elasticity and rheology of iron above 220 GPa and the nature of the Earth's inner core. Nature 396 (6713), 741–743. https://doi.org/10.1038/25506.
Mao, W.L., Mao, H.-K., Sturhahn, W., Zhao, J., Prakapenka, V.B., Meng, Y., Shu, J., Fei, Y., Hemley, R.J., 2006. Iron-rich post-perovskite and the origin of ultralow-velocity zones. Science 312 (5773), 564–565. https://doi.org/10.1126/science.1123442.
Marone, F., Romanowicz, B., 2007. The depth distribution of azimuthal anisotropy in the continental upper mantle. Nature 447, 198–201. https://doi.org/10.1038/nature05742.
Marquardt, D.W., 1963. An algorithm for least-squares estimation of nonlinear parameters. J. Soc. Ind. Appl. Math. 11 (2), 431–441.
Marquardt, H., Buchen, J., Mendez, A.S.J., Kurnosov, A., Wendt, M., Rothkirch, A., Pennicard, D., Liermann, H., 2018. Elastic softening of (Mg0.8Fe0.2)O Ferropericlase across the Iron spin crossover measured at seismic frequencies. Geophys. Res. Lett. 45 (14), 6862–6868. https://doi.org/10.1029/2018gl077982.
Masters, G., 1979. Observational constraints on the chemical and thermal structure of the Earth's deep interior. Geophys. J. R. Astron. Soc. 57 (2), 507–534. https://doi.org/10.1111/j.1365-246x.1979.tb04791.x.
Masters, G., Gilbert, F., 1983. Attenuation in the earth at low frequencies. Philosophical transactions for the Royal Society of London. Series A, Mathemat. Phys. Sci. 308 (1504), 479–522. https://doi.org/10.1098/rsta.1983.0016.
Masters, G., Gubbins, D., 2003. On the resolution of density within the earth. Phys. Earth Planet. Inter. 140 (1–3), 159–167. https://doi.org/10.1016/j.pepi.2003.07.008.
Masters, G., Laske, G., Bolton, H., Dziewonski, A., 2000a. The relative behavior of shear velocity, bulk sound speed, and compressional velocity in the mantle: Implications for chemical and thermal structure. In: Karato, S., Forte, A., Liebermann, R., Masters, G., Stixrude, L. (Eds.), Earth's Deep Interior: Mineral Physics and Tomography from the Atomic to the Global Scale, Geophys. Monogr. Ser, vol. 117. American Geophysical Union, Washington, D. C, pp. 63–87.
Masters, G., Laske, G., Gilbert, F., 2000b. Autoregressive estimation of the splitting matrix of free-oscillation multiplets. Geophys. J. Int. 141 (1), 25–42. https://doi.org/10.1046/j.1365-246x.2000.00058.x.
Matas, J., Bass, J., Ricard, Y., Mattern, E., Bukowinski, M.S.T., 2007. On the bulk composition of the lower mantle: predictions and limitations from generalized inversion of radial seismic profiles. Geophys. J. Int. 170 (2), 764–780. https://doi.org/10.1111/j.1365-246x.2007.03454.x.
Mattern, E., Matas, J., Ricard, Y., Bass, J., 2005. Lower mantle composition and temperature from mineral physics and thermodynamic modelling. Geophys. J. Int. 160, 973–990. https://doi.org/10.1111/j.1365-246x.2004.02549.x.
Matyska, C., Yuen, D.A., 2000. Profiles of the Bullen parameter from mantle convection modelling. Earth Planet. Sci. Lett. 178 (1–2), 39–46. https://doi.org/10.1016/s0012-821x(00)00060-1.
Matyska, C., Yuen, D.A., 2002. Bullen's parameter: a link between seismology and geodynamical modelling. Earth Planet. Sci. Lett. 198 (3–4), 471–483. https://doi.org/10.1016/s0012-821x(01)00607-0.
McCarthy, C., Takei, Y., Hiraga, T., 2011. Experimental study of attenuation and dispersion over a broad frequency range: 2. The universal scaling of polycrystalline materials. J. Geophys. Res. Solid Earth 116, B09207. https://doi.org/10.1029/2011jb008384.
McDonough, W.F., Sun, S., s., 1995. The composition of the earth. Chem. Geol. 120 (3–4), 223–253. https://doi.org/10.1016/0009-2541(94)00140-4.
McKenzie, D., Bickle, M.J., 1988. The volume and composition of melt generated by extension of the lithosphere. Geophys. J.R. Astron. Soc. 29 (3), 625–679. https://doi.org/10.1093/petrology/29.3.625.
Mckenzie, D.P., Roberts, J.M., Weiss, N.O., 1974. Convection in the earth's mantle: towards a numerical simulation. J. Fluid Mech. 62 (03), 465. https://doi.org/10.1017/s0022112074000784.
McKenzie, D., Jackson, J., Priestley, K., 2005. Thermal structure of oceanic and continental lithosphere. Earth Planet. Sci. Lett. 233 (3), 337–349.
McNamara, A.K., Zhong, S., 2004. Thermochemical structures within a spherical mantle: Superplumes or piles? J. Geophys. Res. Solid Earth 109, B07402. https://doi.org/10.1029/2003jb002847.
Menke, W., 1989. Geophysical Data Analysis: Discrete Inverse Theory. Academic, San Diego, Calif, Academic, San Diego, Calif.

Merkel, S., Shu, J., Gillet, P., Mao, H., Hemley, R.J., 2005. X-ray diffraction study of the single-crystal elastic moduli of ϵ-Fe up to 30 GPa. J. Geophys. Res. Solid Earth 110, B05201. https://doi.org/10.1029/2004jb003197.
Mochizuki, E., 1986. The free oscillations of an anisotropic and heterogeneous earth. Geophys. J. Int. 86 (1), 167–176.
Monnereau, M., Yuen, D.A., 2002. How flat is the lower-mantle temperature gradient? Earth Planet. Sci. Lett. 202 (1), 171–183. https://doi.org/10.1016/s0012-821x(02)00756-2.
Montagner, J.-P., 1998. Where Can Seismic Anisotropy Be Detected in the Earth's Mantle? In Boundary Layers… pure and applied geophysics, 151 (2), 223–256. https://doi.org/10.1007/s000240050113.
Montagner, J.-P., 2002. Upper mantle low anisotropy channels below the Pacific plate. Earth Planet. Sci. Lett. 202 (2), 263–274. https://doi.org/10.1016/s0012-821x(02)00791-4.
Montagner, J., Anderson, D.L., 1989a. Petrological constraints on seismic anisotropy. Phys. Earth Planet. Inter. 54, 82–105.
Montagner, J.-P., Anderson, D.L., 1989b. Constrained reference mantle model. Phys. Earth Planet. Inter. 58 (2–3), 205–227. https://doi.org/10.1016/0031-9201(89)90055-1.
Montagner, J., Jobert, N., 1988. Vectorial tomography: II. Application to the Indian Ocean. Geophys. J. Int. 94, 309–344. https://doi.org/10.1111/j.1365-246x.1988.tb05904.x.
Montagner, J., Kennett, B.L.N., 1996. How to reconcile body-wave and normal-mode reference earth models. Geophys. J. Int. 125 (1), 229–248. https://doi.org/10.1111/j.1365-246x.1996.tb06548.x.
Montagner, J.-P., Nataf, H.-C., 1986. A simple method for inverting the azimuthal anisotropy of surface waves. J. Geophys. Res. 91 (B1), 511–520. https://doi.org/10.1029/jb091ib01p00511.
Morelli, A., Dziewonski, A.M., 1993. Body wave Traveltimes and A spherically symmetric P- and S-wave velocity model. Geophys. J. Int. 112 (2), 178–194. https://doi.org/10.1111/j.1365-246x.1993.tb01448.x.
Moulik, P., Ekström, G., 2014. An anisotropic shear velocity model of the Earth's mantle using normal modes, body waves, surface waves and long-period waveforms. Geophys. J. Int. 199, 1713–1738. https://doi.org/10.1093/gji/ggu356.
Moulik, P., Ekström, G., 2016. The relationships between large-scale variations in shear velocity, density, and compressional velocity in the Earth's mantle. J. Geophys. Res. 121, 2737–2771. https://doi.org/10.1002/2015jb012679.
Moulik, P., Ekström, G., 2025. Radial structure of the Earth: (I) Model concepts and data. Phys. Earth Planet. Inter. https://doi.org/10.1016/j.pepi.2025.107319.
Moulik, P., The 3D Reference Earth Model (REM3D) Consortium, 2022. Three-Dimensional Reference Earth Model Project: Data, Techniques, Models & Tools. American Geophysical Union (AGU) Fall Meeting, Chicago, IL, USA. https://doi.org/10.5281/zenodo.7883683.
Moulik, P., Lekic, V., Romanowicz, B., Ma, Z., Schaeffer, A., Ho, T., Beucler, E., Debayle, E., Deuss, A., Durand, S., Ekström, G., Lebedev, S., Masters, G., Priestley, K., Ritsema, J., Sigloch, K., Trampert, J., Dziewonski, A.M., 2022. Global reference seismological data sets: multimode surface wave dispersion. Geophys. J. Int. 228 (3), 1808–1849. https://doi.org/10.1093/gji/ggab418.
Moulik, P., Maguire, R., Gassmoeller, R., Havlin, C., 2023. AVNI: Analysis and Visualization Toolkit for plaNetary Inferences. https://doi.org/10.5281/zenodo.10035731.
Mukerji, T., Mavko, G., 1994. Pore fluid effects on seismic velocity in anisotropic rocks. Geophysics 59 (2), 233–244.
Mukhopadhyay, S., 2012. Early differentiation and volatile accretion recorded in deep-mantle neon and xenon. Nature 486 (7401), 101–104. https://doi.org/10.1038/nature11141.
Müller, G., Mula, A.H., Gregersen, S., 1977. Amplitudes of long-period PcP and the core-mantle boundary. Chem. Geol. 14, 30–40. https://doi.org/10.1016/0031-9201(77)90044-9.
Murakami, M., Hirose, K., Kawamura, K., Sata, N., Ohishi, Y., 2004. Post-perovskite phase transition in MgSiO3. Science 304, 855–858. https://doi.org/10.1126/science.1095932.
Murakami, M., Ohishi, Y., Hirao, N., Hirose, K., 2012. A perovskitic lower mantle inferred from high-pressure, high-temperature sound velocity data. Nature 485 (7396), 90–94. https://doi.org/10.1038/nature11004.
Murnaghan, F.D., 1944. The compressibility of media under extreme pressures. Proc. Natl. Acad. Sci. 30 (9), 244–247. https://doi.org/10.1073/pnas.30.9.244.
Nakagawa, T., Buffett, B.A., 2005. Mass transport mechanism between the upper and lower mantle in numerical simulations of thermochemical mantle convection with multicomponent phase changes. Earth Planet. Sci. Lett. 230 (1–2), 11–27. https://doi.org/10.1016/j.epsl.2004.11.005.
Nakagawa, T., Tackley, P.J., 2005. Deep mantle heat flow and thermal evolution of the Earth's core in thermochemical multiphase models of mantle convection. Geochem. Geophys. Geosyst. 6 (8), Q08003. https://doi.org/10.1029/2005gc000967.
Nakagawa, T., Tackley, P.J., 2006. Three-dimensional structures and dynamics in the deep mantle: effects of post-perovskite phase change and deep mantle layering. Geophys. Res. Lett. 33, L12S11. https://doi.org/10.1029/2006gl025719.
Nakiboglu, S.M., 1982. Hydrostatic theory of the earth and its mechanical implications. Phys. Earth Planet. Inter. 28 (4), 302–311. https://doi.org/10.1016/0031-9201(82)90087-5.
Nicolas, A., Christensen, N., 1987. Formation of anisotropy in upper mantle peridotites: A review. In: Fuchs, K., Froidevaux, C. (Eds.), Composition, Structure and Dynamics of the Lithosphere-Asthenosphere System, Geodyn. Ser. American Geophysical Union, Washington, D. C, pp. 111–123.
Nimmo, F., Price, G.D., Brodholt, J., Gubbins, D., 2004. The influence of potassium on core and geodynamo evolution. Geophys. J. Int. 156 (2), 363–376. https://doi.org/10.1111/j.1365-246x.2003.02157.x.
Nishimura, C.E., Forsyth, D.W., 1989. The anisotropic structure of the upper mantle in the Pacific. Geophys. J. Int. 96, 203–229. https://doi.org/10.1111/j.1365-246x.1989.tb04446.x.
Nomura, R., Ozawa, H., Tateno, S., Hirose, K., Hernlund, J., Muto, S., Ishii, H., Hiraoka, N., 2011. Spin crossover and iron-rich silicate melt in the Earth's deep mantle. Nature 473 (7346), 199–202. https://doi.org/10.1038/nature09940.
Nowick, A.S., Berry, B.S., 1972. Anelastic Relaxation in Crystalline Solids. Academic Press, New York/London.
O'Connell, R., Budiansky, B., 1978. Measures of dissipation in viscoelastic media. Geophys. Res. Lett. 5 (1), 5. https://doi.org/10.1029/gl005i001p00005.
Oganov, A.R., Ono, S., 2004. Theoretical and experimental evidence for a post-perovskite phase of $MgSiO_3$ in Earth's D″ layer. Nature 430, 445–448. https://doi.org/10.1038/nature02701.
Ohuchi, T., Irifune, T., 2013. Development of A-type olivine fabric in water-rich deep upper mantle. Earth Planet. Sci. Lett. 362, 20–30. https://doi.org/10.1016/j.epsl.2012.11.029.
Olugboji, T.M., Karato, S., Park, J., 2013. Structures of the oceanic lithosphere-asthenosphere boundary: mineral-physics modeling and seismological signatures. Geochem. Geophys. Geosyst. 14 (4), 880–901. https://doi.org/10.1002/ggge.20086.
Pamato, M.G., Kurnosov, A., Boffa Ballaran, T., Frost, D.J., Ziberna, L., Giannini, M., Speziale, S., Tkachev, S.N., Zhuravlev, K.K., Prakapenka, V.B., 2016. Single crystal elasticity of majoritic garnets: stagnant slabs and thermal anomalies at the base of the transition zone. Earth Planet. Sci. Lett. 451, 114–124. https://doi.org/10.1016/j.epsl.2016.07.019.
Panning, M., Romanowicz, B., 2004. Inferences on flow at the base of Earth's mantle based on seismic anisotropy. Science 303 (5656), 351–353. https://doi.org/10.1126/science.1091524.
Parmentier, E.M., Sotin, C., Travis, B.J., 1994. Turbulent 3-D thermal convection in an infinite Prandtl number, volumetrically heated fluid: implications for mantle dynamics. Geophys. J. Int. 116 (2), 241–251. https://doi.org/10.1111/j.1365-246x.1994.tb01795.x.
Pearson, D.G., Brenker, F.E., Nestola, F., McNeill, J., Nasdala, L., Hutchison, M.T., Matveev, S., Mather, K., Silversmit, G., Schmitz, S., Vekemans, B., Vincze, L., 2014. Hydrous mantle transition zone indicated by ringwoodite included within diamond. Nature 507 (7491), 221–224. https://doi.org/10.1038/nature13080.
Peters, B.J., Carlson, R.W., Day, J.M.D., Horan, M.F., 2017. Hadean silicate differentiation preserved by anomalous $^{142}Nd/^{144}Nd$ ratios in the Réunion hotspot source. Nature 555 (7694), 89–93. https://doi.org/10.1038/nature25754.
Piet, H., Badro, J., Nabiei, F., Dennenwaldt, T., Shim, S.-H., Cantoni, M., Hébert, C., Gillet, P., 2016. Spin and valence dependence of iron partitioning in Earth's deep mantle. Proc. Natl. Acad. Sci. 113 (40), 11127–11130. https://doi.org/10.1073/pnas.1605290113.
Priestley, K., McKenzie, D., 2013. The relationship between shear wave velocity, temperature, attenuation and viscosity in the shallow part of the mantle. Earth Planet. Sci. Lett. 381, 78–91. https://doi.org/10.1016/j.epsl.2013.08.022.
Putirka, K., 2008. Excess temperatures at ocean islands: implications for mantle layering and convection. Geology 36 (4), 283–286.
Raj, R., 1975. Transient behavior of diffusion-induced creep and creep rupture. Metall. Trans. A. 6 (8), 1499–1509. https://doi.org/10.1007/bf02641961.
Randall, M.J., 1976. Attenuative dispersion and frequency shifts of the earth's free oscillations. Phys. Earth Planet. Inter. 12 (1), P1–P4. https://doi.org/10.1016/0031-9201(76)90002-9.
Resovsky, J., Ritzwoller, M., 1998. New and refined constraints on three-dimensional earth structure from normal modes below 3 mHz. J. Geophys. Res. 103, 783–810.
Resovsky, J., Ritzwoller, M., 1999. Regularization uncertainty in density models estimated from normal mode data. Geophys. Res. Lett. 26, 2319–2322.
Revenaugh, J., Jordan, T.H., 1991. Mantle layering from ScS reverberations: 2. The transition zone. J. Geophys. Res. Solid Earth 96 (B12), 19763–19780. https://doi.org/10.1029/91jb01486.
Richard, G., Monnereau, M., Ingrin, J., 2002. Is the transition zone an empty water reservoir? Inferences from numerical model of mantle dynamics. Earth Planet. Sci. Lett. 205 (1–2), 37–51. https://doi.org/10.1016/s0012-821x(02)01012-9.
Richter, F.M., McKenzie, D.P., 1981. Parameterizations for the horizontally averaged temperature of infinite Prandtl number convection. J. Geophys. Res. Solid Earth 86 (B3), 1738–1744. https://doi.org/10.1029/jb086ib03p01738.
Ricolleau, A., Perrillat, J.P., Fiquet, G., Daniel, I., Matas, J., Addad, A., Menguy, N., Cardon, H., Mezouar, M., Guignot, N., 2010. Phase relations and equation of state of a natural MORB: implications for the density profile of subducted oceanic crust in the Earth's lower mantle. J. Geophys. Res. Solid Earth 115, B08202. https://doi.org/10.1029/2009jb006709.
Ringwood, A.E., 1966. Chemical evolution of the terrestrial planets. Geochim. Cosmochim. Acta 30 (1), 41–104. https://doi.org/10.1016/0016-7037(66)90090-1.
Ringwood, A.E., 1975. Composition and Petrology of the Earth's Mantle. McGraw-Hill, New York.
Ringwood, A.E., 1982. Phase transformations and differentiation in subducted lithosphere: implications for mantle dynamics, basalt petrogenesis, and crustal evolution. J. Geol. 90 (6), 611–643.
Ritsema, J., Deuss, A., van Heijst, H.J., 2011. S40RTS: a degree-40 shear-velocity model for the mantle from new Rayleigh wave dispersion, teleseismic traveltime and normal-mode splitting function measurements. Geophys. J. Int. 184, 1223–1236. https://doi.org/10.1111/j.1365-246x.2010.04884.x.

Rost, S., Garnero, E.J., Williams, Q., Manga, M., 2005. Seismological constraints on a possible plume root at the core–mantle boundary. Nature 435 (7042), 666–669. https://doi.org/10.1038/nature03620.
Roy, P.B., Roy, S.B., 2001. An isothermal equation of state of solid. Phys. Status Solidi B 226 (1), 125–132. https://doi.org/10.1002/1521-3951(200107)226:1<125::aid-pssb125>3.0.co;2-1.
Rudolph, M.L., Moulik, P., Lekić, V., 2020. Bayesian inference of mantle viscosity from whole-mantle density models. Geochem. Geophys. Geosyst. 21 (11), e2020GC009335. https://doi.org/10.1029/2020gc009335.
Saikia, A., Frost, D.J., Rubie, D.C., 2008. Splitting of the 520-kilometer seismic discontinuity and chemical heterogeneity in the mantle. Science 319 (5869), 1515–1518. https://doi.org/10.1126/science.1152818.
Sailor, R.V., Dziewonski, A.M., 1978. Measurements and interpretation of normal mode attenuation. Geophys. J. Int. 53 (3), 559–581. https://doi.org/10.1111/j.1365-246x.1978.tb03760.x.
Sang, L., Bass, J.D., 2014. Single-crystal elasticity of diopside to 14gpa by brillouin scattering. Phys. Earth Planet. Inter. 228, 75–79. https://doi.org/10.1016/j.pepi.2013.12.011.
Schaeffer, A.J., Lebedev, S., Becker, T.W., 2016. Azimuthal seismic anisotropy in the Earth's upper mantle and the thickness of tectonic plates. Geophys. J. Int. 207 (2), 901–933. https://doi.org/10.1093/gji/ggw309.
Schlue, J.W., Knopoff, L., 1976. Shear wave anisotropy in the upper mantle of the Pacific Basin. Geophys. Res. Lett. 3 (6), 359–362. https://doi.org/10.1029/gl003i006p00359.
Schuberth, B.S.A., Zaroli, C., Nolet, G., 2012. Synthetic seismograms for a synthetic earth: long-period P- and S-wave traveltime variations can be explained by temperature alone. Geophys. J. Int. 188, 1393–1412. https://doi.org/10.1111/j.1365-246x.2011.05333.x.
Seager, S., 2013. Exoplanet Habitability. Science (New York, N.Y.) 340 (6132), 577–581. https://doi.org/10.1126/science.1232226.
Selby, N.D., Woodhouse, J.H., 2002. The Q structure of the upper mantle: Constraints from Rayleigh wave amplitudes. J. Geophys. Res. Solid Earth 107 (B5). https://doi.org/10.1029/2001jb000257. ESE 5–11.
Shearer, P.M., Flanagan, M.P., 1999. Seismic velocity and density jumps across the 410- and 660-kilometer discontinuities. Science 285 (5433), 1545–1548. https://doi.org/10.1126/science.285.5433.1545.
Shearer, P., Masters, G., 1990. The density and shear velocity contrast at the inner core boundary. Geophys. J. Int. 102 (2), 491–498. https://doi.org/10.1111/j.1365-246x.1990.tb04481.x.
Shirey, S.B., Walker, R.J., 1998. The re-Os isotope system in Cosmochemistry and high-temperature geochemistry. Earth Planet. Sci. 26 (1), 423–500. https://doi.org/10.1146/annurev.earth.26.1.423.
Shukla, G., Cococcioni, M., Wentzcovitch, R.M., 2016. Thermoelasticity of Fe3+− and Al-bearing bridgmanite: effects of iron spin crossover. Geophys. Res. Lett. 43 (11), 5661–5670. https://doi.org/10.1002/2016gl069332.
Simons, F.J., van der Hilst, R.D., 2003. Seismic and mechanical anisotropy and the past and present deformation of the Australian lithosphere. Earth Planet. Sci. Lett. 211 (3–4), 271–286. https://doi.org/10.1016/s0012-821x(03)00198-5.
Sinha, G., Butler, S.L., 2007. On the origin and significance of subadiabatic temperature gradients in the mantle. J. Geophys. Res. Solid Earth 112, B10406. https://doi.org/10.1029/2006jb004850.
Sinogeikin, S.V., Bass, J.D., Katsura, T., 2003. Single-crystal elasticity of ringwoodite to high pressures and high temperatures: implications for 520 km seismic discontinuity. Phys. Earth Planet. Inter. 136 (1), 41–66. https://doi.org/10.1016/S0031-9201(03)00022-0.
Smith, M.L., Dahlen, F.A., 1973. The azimuthal dependence of Love and Rayleigh wave propagation in a slightly anisotropic medium. J. Geophys. Res. Solid Earth 78, 3321–3333. https://doi.org/10.1029/jb078i017p03321.
Solomatov, V.S., Reese, C.C., 2008. Grain size variations in the earth's mantle and the evolution of primordial chemical heterogeneities. Journal of geophysical research: solid. Earth 113 (B7). https://doi.org/10.1029/2007JB005319.
Song, X., Helmberger, D.V., 1995. A P wave velocity model of Earth's core. J. Geophys. Res. Solid Earth 100 (B6), 9817–9830. https://doi.org/10.1029/94jb03135.
Speziale, S., Milner, A., Lee, V.E., Clark, S.M., Pasternak, M.P., Jeanloz, R., 2005. Iron spin transition in Earth's mantle. Proc. Natl. Acad. Sci. 102 (50), 17918–17922. https://doi.org/10.1073/pnas.0508919102.
Stacey, F.D., 1995. Theory of thermal and elastic properties of the lower mantle and core. Phys. Earth Planet. Inter. 89 (3–4), 219–245. https://doi.org/10.1016/0031-9201(94)03005-4.
Stacey, F.D., 2005. High pressure equations of state and planetary interiors. Rep. Prog. Phys. 68 (2), 341–383. https://doi.org/10.1088/0034-4885/68/2/r03.
Stacey, F., Davis, P., 2004. High pressure equations of state with applications to the lower mantle and core. Phys. Earth Planet. Inter. 142 (3–4), 137–184. https://doi.org/10.1016/j.pepi.2004.02.003.
Stacey, F.D., Loper, D.E., 1983. The thermal boundary-layer interpretation of D and its role as a plume source. Phys. Earth Planet. Inter. 33, 45–55.
Stevenson, D., 1980. Applications of liquid state physics to the Earth's core. Phys. Earth Planet. Inter. 22 (1), 42–52. https://doi.org/10.1016/0031-9201(80)90099-0.
Stevenson, D.J., 1981. Models of the Earth's Core. Science 214 (4521), 611–619. https://doi.org/10.1126/science.214.4521.611.
Stixrude, L., 2007. Properties of rocks and minerals - seismic properties of rocks and minerals, and structure of the earth. In: Schubert, G. (Ed.), Treatise on Geophysics, vol. 2. Elsevier, pp. 7–32. https://doi.org/10.1016/B978-044452748-6.00042-0.
Stixrude, L., Lithgow-Bertelloni, C., 2011. Thermodynamics of mantle minerals – II. Phase equilibria. Geophys. J. Int. 184, 1180–1213. https://doi.org/10.1111/j.1365-246x.2010.04890.x.
Stixrude, L., Lithgow-Bertelloni, C., 2012. Geophysics of chemical heterogeneity in the mantle. Annu. Rev. Earth Planet. Sci. 40, 569–595. https://doi.org/10.1146/annurev.earth.36.031207.124244.
Stixrude, L., Lithgow-Bertelloni, C., 2022. Thermal expansivity, heat capacity and bulk modulus of the mantle. Geophys. J. Int. 228 (2), 1119–1149. https://doi.org/10.1093/gji/ggab394.
Tackley, P.J., 1998. Three-dimensional simulations of mantle convection with a Thermo-chemical basal boundary layer: D″? the core-mantle boundary region. Am. Geophys. Union 231–253. https://doi.org/10.1029/gd028p0231.
Tackley, P.J., 2012. Dynamics and evolution of the deep mantle resulting from thermal, chemical, phase and melting effects. Earth Sci. Rev. 110, 1–25. https://doi.org/10.1016/j.earscirev.2011.10.001.
Tackley, P.J., Stevenson, D.J., Glatzmaier, G.A., Schubert, G., 1993. Effects of an endothermic phase transition at 670 km depth in a spherical model of convection in the Earth's mantle. Nature 361 (6414), 699–704. https://doi.org/10.1038/361699a0.
Takei, Y., Karasawa, F., Yamauchi, H., 2014. Temperature, grain size, and chemical controls on polycrystal anelasticity over a broad frequency range extending into the seismic range. J. Geophys. Res. 119 (7), 5414–5443. https://doi.org/10.1002/2014jb011146.
Takeuchi, H., Saito, M., 1972. Seismic surface waves. In: Bolt, B.A. (Ed.), Seismology: Surface Waves and Earth Oscillations, Methods in Comput. Phys, Vol, vol. 11. Academic Press, New York, pp. 217–295.
Tanaka, S., 2007. Possibility of a low P-wave velocity layer in the outermost core from global SmKS waveforms. Earth Planet. Sci. Lett. 259 (3–4), 486–499. https://doi.org/10.1016/j.epsl.2007.05.007.
Thomsen, L., 1986. Weak elastic anisotropy. Geophysics 51 (10), 1954–1966. https://doi.org/10.1190/1.1442051.
Thorne, M.S., Garnero, E.J., 2004. Inferences on ultralow-velocity zone structure from a global analysis of SPdKS waves. J. Geophys. Res. Solid Earth 109, B08301. https://doi.org/10.1029/2004jb003010.
Tkalčić, H., Kennett, B.L.N., Cormier, V.F., 2009. On the inner—outer core density contrast from PKiKP/PcP amplitude ratios and uncertainties caused by seismic noise. Geophys. J. Int. 179 (1), 425–443. https://doi.org/10.1111/j.1365-246x.2009.04294.x.
Touboul, M., Puchtel, I.S., Walker, R.J., 2012. ^{182}W evidence for long-term preservation of early mantle differentiation products. Science 335 (6072), 1065–1069. https://doi.org/10.1126/science.1216351.
Trampert, J., 2004. Probabilistic tomography maps chemical heterogeneities throughout the lower mantle. Science 306, 853–856. https://doi.org/10.1126/science.1101996.
Trefethen, L., Bau, D., 1997. Numerical linear algebra. Ind. Appl. Math., Philadelphia, PA. Soc. Ind. Appl. Math., Philadelphia, PA, Soc.
Tsuchiya, T., Tsuchiya, J., Umemoto, K., Wentzcovitch, R.M., 2004. Phase transition in MgSiO3 perovskite in the earth's lower mantle. Earth Planet. Sci. Lett. 224, 241–248. https://doi.org/10.1016/j.epsl.2004.05.017.
Tsuchiya, T., Wentzcovitch, R.M., Silva, C.R.S., d., Gironcoli, S. d., 2006. Spin transition in Magnesiowüstite in Earth's lower mantle. Phys. Rev. Lett. 96 (19), 198501. https://doi.org/10.1103/physrevlett.96.198501.
Tucker, J.M., Keken, P.E., Jones, R.E., Ballentine, C.J., 2020. A role for subducted oceanic crust in generating the depleted Mid-Ocean ridge basalt mantle. Geochem. Geophys. Geosyst. 21, e2020GC009148. https://doi.org/10.1029/2020gc009148.
Ullrich, L., Van der Voo, R., 1981. Minimum continental velocities with respect to the pole since the Archean. Tectonophysics 74 (1–2), 17–27. https://doi.org/10.1016/0040-1951(81)90125-6.
Valencia-Cardona, J.J., Williams, Q., Shukla, G., Wentzcovitch, R.M., 2017. Bullen's parameter as a seismic observable for spin crossovers in the lower mantle. Geophys. Res. Lett. 44, 9314–9320. https://doi.org/10.1002/2017gl074666.
van der Hilst, R.D., Widiyantoro, S., Engdahl, E.R., 1997. Evidence for deep mantle circulation from global tomography. Nature 386, 578–584.
Vinet, P., Ferrante, J., Rose, J.H., Smith, J.R., 1987. Compressibility of solids. J. Geophys. Res. Solid Earth 92 (B9), 9319–9325. https://doi.org/10.1029/jb092ib09p09319.
Visser, K., Trampert, J., Lebedev, S., Kennett, B., 2008. Probability of radial anisotropy in the deep mantle. Earth Planet. Sci. Lett. 270 (3), 241–250.
Waszek, L., Deuss, A., 2015. Anomalously strong observations of PKiKP/PcP amplitude ratios on a global scale. J. Geophys. Res. 120 (7), 5175–5190. https://doi.org/10.1002/2015jb012038.
Waszek, L., Tauzin, B., Schmerr, N.C., Ballmer, M.D., Afonso, J.C., 2021. A poorly mixed mantle transition zone and its thermal state inferred from seismic waves. Nat. Geosci. 14 (12), 949–955. https://doi.org/10.1038/s41561-021-00850-w.
Weidner, D.J., 1985. A mineral physics test of a pyrolite mantle. Geophys. Res. Lett. 12 (7), 417–420. https://doi.org/10.1029/gl012i007p00417.
Weidner, D.J., Wang, Y., 1998. Chemical- and Clapeyron-induced buoyancy at the 660 km discontinuity. J. Geophys. Res. Solid Earth 103 (B4), 7431–7441. https://doi.org/10.1029/97jb03511.
Weidner, D.J., Wang, Y., 2000. Phase transformations: Implications for mantle structure. In: Karato, S., Forte, A., Liebermann, R., Masters, G., Stixrude, L. (Eds.), Earth's Deep Interior: Mineral Physics and Tomography from the Atomic to the Global Scale, Geophys. Monogr. Ser, vol. 117. American Geophysical Union, Washington, D. C, pp. 215–235.
Weidner, D.J., Sawamoto, H., Sasaki, S., Kumazawa, M., 1984. Single-crystal elastic properties of the spinel phase of Mg_2SiO_4. J. Geophys. Res. Solid Earth 89 (B9), 7852–7860. https://doi.org/10.1029/JB089iB09p07852.
Wentzcovitch, R.M., Justo, J.F., Wu, Z., Silva, C.R.S., d., Yuen, D. A., Kohlstedt, D., 2009. Anomalous compressibility of ferropericlase throughout the iron spin cross-over. Proc. Natl. Acad. Sci. 106 (21), 8447–8452. https://doi.org/10.1073/pnas.0812150106.

Wentzcovitch, R.M., Yu, Y.G., Wu, Z., 2010. Thermodynamic properties and phase relations in mantle minerals investigated by first principles Quasiharmonic theory. Rev. Mineral. Geochem. 71 (1), 59–98. https://doi.org/10.2138/rmg.2010.71.4.

Widmer, R., Masters, G., Gilbert, F., 1991. Spherically symmetric attenuation within the earth from normal mode data. Geophys. J. Int. 104 (3), 541–553. https://doi.org/10.1111/j.1365-246x.1991.tb05700.x.

Williams, Q., Garnero, E.J., 1996. Seismic evidence for partial melt at the base of Earth's mantle. Science 273 (5281), 1528–1530. https://doi.org/10.1126/science.273.5281.1528.

Williamson, E.D., Adams, L., 1923. Density distribution in the earth. J. Wash. Acad. Sci. 13 (19), 413–428. https://doi.org/10.2307/24532814.

Woodhouse, J., 1980. The coupling and attenuation of nearly resonant multiplets in the Earth's free oscillation spectrum. Geophys. J. Int. 61 (2), 261–283.

Woodhouse, J.H., 1981. A note on the calculation of travel times in a transversely isotropic earth model. Phys. Earth Planet. Inter. 25 (4), 357–359. https://doi.org/10.1016/0031-9201(81)90047-9.

Workman, R.K., Hart, S.R., 2005. Major and trace element composition of the depleted MORB mantle (DMM). Earth Planet. Sci. Lett. 231, 53–72. https://doi.org/10.1016/j.epsl.2004.12.005.

Xie, S., Tackley, P.J., 2004. Evolution of U-Pb and Sm-Nd systems in numerical models of mantle convection and plate tectonics. J. Geophys. Res. Solid Earth 109, B11204. https://doi.org/10.1029/2004jb003176.

Xu, W., Lithgow-Bertelloni, C., Stixrude, L., Ritsema, J., 2008. The effect of bulk composition and temperature on mantle seismic structure. Chem. Geol. 275, 70–79. https://doi.org/10.1016/j.epsl.2008.08.012.

Yan, J., Ballmer, M.D., Tackley, P.J., 2020. The evolution and distribution of recycled oceanic crust in the Earth's mantle: insight from geodynamic models. Earth Planet. Sci. Lett. 537, 116171. https://doi.org/10.1016/j.epsl.2020.116171.

Yu, Y.G., Wentzcovitch, R.M., Tsuchiya, T., Umemoto, K., Weidner, D.J., 2007. First principles investigation of the postspinel transition in Mg_2SiO_4. Geophys. Res. Lett. 34, L10306. https://doi.org/10.1029/2007gl029462.

Yu, Y.G., Wu, Z., Wentzcovitch, R.M., 2008. α–β–γ transformations in Mg_2SiO_4 in Earth's transition zone. Chem. Geol. 273, 115–122. https://doi.org/10.1016/j.epsl.2008.06.023.

Yu, C., Goes, S., Day, E.A., van der Hilst, R.D., 2023. Seismic evidence for global basalt accumulation in the mantle transition zone. Science. Advances 9 (22), eadg0095. https://doi.org/10.1126/sciadv.adg0095.

Yuan, K., Romanowicz, B., 2017. Seismic evidence for partial melting at the root of major hot spot plumes. Science 357 (6349), 393–397. https://doi.org/10.1126/science.aan0760.

Zener, C., 1948. Elasticity and Anelasticity of Metals. University of Chicago Press.

Zhu, H., Bozdağ, E., Duffy, T.S., Tromp, J., 2013. Seismic attenuation beneath Europe and the North Atlantic: implications for water in the mantle. Earth Planet. Sci. Lett. 381, 1–11. https://doi.org/10.1016/j.epsl.2013.08.030.

Zindler, A., Hart, S., 1986. Chemical geodynamics. Annu. Rev. Earth Planet. Sci. 14, 493–571. https://doi.org/10.1146/annurev.ea.14.050186.002425.

Zou, Z., Koper, K.D., Cormier, V.F., 2008. The structure of the base of the outer core inferred from seismic waves diffracted around the inner core. J. Geophys. Res. Solid Earth 113, B05314. https://doi.org/10.1029/2007jb005316.